Title
Experimental Investigations of Beam Driven Plasma Wakefield Accelerators

Author
Vafaei-Najafabadi, Navid

Publication Date
2016

Peer reviewed|Thesis/dissertation

University of California
Los Angeles

Experimental Investigations of Beam Driven Plasma Wakefield Accelerators

A dissertation submitted in partial satisfaction
of the requirements for the degree
Doctor of Philosophy in Electrical Engineering

by

Navid Vafaei-Najafabadi

2016

Abstract of the Dissertation

Experimental Investigations of Beam Driven Plasma Wakefield Accelerators

by

Navid Vafaei-Najafabadi

Doctor of Philosophy in Electrical Engineering

University of California, Los Angeles, 2016

Professor Chandra J Joshi, Chair

A plasma wakefield accelerator (PWFA) uses a plasma wave (a wake) to accelerate electrons at a gradient that is three orders of magnitude higher than that of a conventional accelerator. When the plasma wave is driven by a high-density particle beam or a high-intensity laser pulse, it evolves into the nonlinear blowout regime, where the driver expels the background plasma electrons, resulting in an ion cavity forming behind the driver. This ion cavity has ideal properties for accelerating and focusing electrons. One method to insert electrons into this highly-relativistic, transient structure is by ionization injection. In this method, electrons resulting from further ionization of the ions inside the wake are trapped and accelerated by the wakefield. These injected electrons absorb the energy of the wake, resulting in a reduced accelerating field amplitude; this phenomenon is known as beam loading.

This thesis discusses experiments that demonstrate how ionization injection can, on the one hand, lead to excessive beam loading and be a detriment to a PWFA, while on the other hand, it may be taken advantage of to produce bright electron beams that will be necessary for applications of a PWFA to a free electron laser (FEL) or a collider. These experiments were part of the FACET Campaign at the SLAC National Accelerator Laboratory and used FACET's 3 nC, 20.35 GeV electron beam to field ionize the plasma source and drive a wake.

In the first experiment, the plasma source was a 30 cm column of rubidium (Rb) vapor. The low ionization potential and high atomic mass of Rb made it a suitable candidate as a

plasma source for a PWFA. However, the low ionization potential of the Rb+ ion resulted in continuous ionization of Rb+ and injection of electrons along the length of the plasma. This resulted in heavy beam-loading, which reduced the strength of the accelerating field by half, making the Rb source unusable for a PWFA.

In the second experiment, the plasma source was a column of lithium (Li) vapor bound by cold helium (He) gas. Here, the ionization injection of He electrons in the 10 cm boundary region between Li and He led to localized beam loading and resulted in an accelerated electron beam with high energy (32 GeV), a 10% energy spread, and an emittance an order of magnitude smaller than the drive beam. Particle-in-cell simulations indicate that the beam loading can be further optimized by reducing the injection region even more, which can lead to bright, high-current, low-energy-spread electron beams.

The dissertation of Navid Vafaei-Najafabadi is approved.

Christoph Niemann

Tatsuo Itoh

Warren B Mori

Chandra J Joshi, Committee Chair

University of California, Los Angeles

2016

To my parents, for their unrelenting love and support

To the one I love the most; may our love prove stronger than the Fates trying to tear us apart

Table of Contents

1 Introduction **1**

1.1 Plasma Accelerators for the Colliders of the Future 1

1.2 Plasma Wakefield Acceleration 3

1.3 Forces in the Blowout Regime 4

1.4 Electron Beam Driven Plasma Wakefield Accelerator 8

1.5 Previous Work 11

1.6 Work Carried Out in This Thesis 16

2 Limitation on the Accelerating Gradient of a Wakefield Excited by an Ultra-Relativistic Electron Beam in Rubidium Plasma **20**

2.1 Introduction 20

2.2 Beam Loading and Transformer Ratio 23

2.3 Ionization Injection into the Plasma Wakefield 25

2.4 Experimental Setup 27

2.5 Physics of Distributed Injection 32

2.6 Evidence for Distributed Injection 38

2.7 Beam Loading due to Distributed Injection 43

2.8 Simulations 46

2.9 Conclusions 54

3 Generation of Low Emittance Electron Beams **55**

3.1 Introduction 55

3.2 Experimental Setup 56

3.3 Observation of Injected Electrons 57

3.4 Helium as Source of Injected Charge (Simulation) . . . 61
3.5 Helium as Source of Injected Charge (Experiment) . . . 64
3.6 Plasma Length Scaling . . . 68
3.7 Conclusions . . . 74
3.8 Acknowledgements . . . 74

4 Simulations as a Guide for Experimental Design . . . 75
4.1 Introduction . . . 75
4.2 Single Betatron Cycle Simulation . . . 76
4.3 Density Scaling Observed in the Simulation . . . 81
4.3.1 Scaling of Plasma Density . . . 83
4.3.2 Scaling of Accelerated Bunch Parameters with Impurity Density . . . 86
4.4 Emittance Measurement in a 3D Simulation . . . 90
4.5 Effect of Change of Plasma Column's Radius on Acceleration . . . 93

5 Conclusions . . . 98

A Plasma Sources for PWFA . . . 101

B Distributed Beam Loading Supplement . . . 107
B.1 Betatron oscillation of beam in various foil conditions . . . 107

C Revisiting Emittance Measurement in the Experiment . . . 109
C.1 Introduction . . . 109
C.2 Modeling Electron Beam Propagation To Detection Plane . . . 112
C.3 Measuring Beam Width and Estimating Emittance . . . 114
C.3.1 Emittance of the Drive Beam . . . 116

References **121**

List of Figures

1.1 Properties of the blowout regime. (a) shows the plasma density color map for the simulation. The wake is propagating from the right to the left. The current density of the two bunches is superimposed in red. (b) shows the on-axis beam densities in red and the on-axis plasma density in blue. The region where plasma density comes to zero is the blowout region. (c) shows the color map for the longitudinal field $\bar{E_z}$. The radial uniformity of this field can be observed from the color table. (d) shows the on-axis electric field in the simulation. This field is modified(loaded) by the presence of the trailing bunch. (e) shows the transverse force $\bar{E_X} - \bar{B_Y}$. longitudinal uniformity of the transverse field can be observed in the color map. The red line at 5 c/ω_p indicates the location of lineout shown in (f). (f) shows the transverse lineout, which is linear and focusing for electrons. . 7

1.2 (a) Electron beam densities for three drive-witness simulations, where the witness beams are the same in all cases and the density of the drive beam is varied by varying σ_r; $k_p\sigma_r$ is 0.65, 0.98, and 1.3 for the blue, green, and red case respectively, corresponding to peak n_b/n_p of 2.1, 1, and 0.5 for the three cases. The value $\Lambda = 0.90$ is the same for all three cases. The beam propagation direction is indicated by a red arrow. (b) The resulting longitudinal field is presented for the three simulations in (a) 10

2.1 Beam loading in a drive/trailing electron-driven plasma wakefield accelerator (a) The longitudinal density profile of drive and trailing electron beams in three different beam loading scenarios. The drive beam density is the same ($n_b \sim 5n_p$) in all three cases. The three cases of trailing beam are: no trailing beam, i.e. unloaded wake (blue), trailing beam with peak density 40% that of the drive bunch (red), and trailing beam with peak density 80% that of the drive bunch (green). (b) The on axis longitudinal electric field for each of the three cases in (a). One can see progressively stronger beam loading that leads to flattening of the wake and reduction in the transformer ratio as described in the text. 24

2.2 Experimental Setup. The electron beam enters from the left. The energy spectrum of the beam before plasma is shown as the inset (E) on the top left. Transition radiation generated as the beam traverses the 1 μm Ti foil (T) is observed simultaneously by a pyroelectric detector (Pyro) and a THz Michelson interferometer (M). Correlation between the pyro and the inverse of the bunch length deduced from the Michelson interferometer is shown beneath the setup. Foils with progressively higher scattering strength (F1-F3) can be inserted in the path of the beam before it enters the plasma oven, leading to progressively increased beam emittance (see Table 2.2 for details). The density profiles of neutral Rb and Ar are plotted underneath the schematic of the oven in blue circles and red diamonds, respectively. Absolutely calibrated toroids upstream and downstream of the plasma record the amount of charge entering and exiting the plasma. The quadrupole magnets Q1 and Q2 along with the dipole magnet D form the imaging energy spectrometer. The Cherenkov radiation emitted by the dispersed electrons between silicon wafers (1) and (2) is detected by camera C to give the electron spectrum after the plasma. An example of the energy spectrum with the white curve showing the integrated charge is shown below camera C. The charge near 20.4 GeV has been attenuated by a factor of 10. The Lanex screen, shielded by a 1mm copper foil, detects the betatron x-rays. 28

2.3 (a) Ionization rates for neutral Rb, neutral Ar, Rb^+, and Ar^+ ions as a function of electric field. (b) The ionization fraction for neutral Rb using an electron beam with $\sigma_z = 40$ μm and $\sigma_r = 35$ μm. The rates are obtained from ADK model. The longitudinal profile of the initial beam is shown in blue lineout and the longitudinal profile of the participating charge is shown in red lineout. (c) Envelope evolution of a beam slice with normalized emittance of $\epsilon_n = 250$ mm-mrad in an ion column with ion density n_i having the same profile in z as the rubidium plasma. The plot of density is shown in green. The propagation of the electron beam in vacuum and in the presence of blowout regime is shown in blue and orange, respectively. Regions with significant presence of Ar are shown in blue shade. The beam size below $\sigma_r < 7.9$ μm ionizes neutral Ar and $\sigma_r < 4.5$ μm ionizes Ar^{1+} and Rb^{1+}. 34

2.4 (a) X-ray yield for a set of 77 consecutive shots sorted as a function of σ_z. In this dataset, Foil F1 is inserted and the the variation of σ_z is due to the shot-to-shot jitter of the phase of the linac (b) ΔQ and x-ray yield are plotted against each other for each shot. (c) ΔW^- sorted as a function of σ_z for the same data. (d) ΔQ correlation with ΔW^- for the same data. 39

2.5 (a) Excess charge as a function of the x-ray yield in four cases obtained with the insertion of various foils that change the beam emittance. The data is filtered by selecting pyro values between 5000 and 5300, ($\sigma_z \sim 40$ μm) so that the current profiles are nearly identical as judged by the similarity of the electron beam spectra before the plasma. The data shown in red triangles is a subset of data in Fig. 2.4. (b) Energy loss is shown as a function of excess charge for the same data as in (a). (c) The electron beam energy spectra for the data shown in (a) and (b). The spectra related to each foil is averaged. 42

2.6 Data from a 71 shot dataset where no foils F1-F3 were inserted. (a) Peak energy loss ΔW^- as a function of σ_z, grouped by a range of 300 in pyro corresponding to $\sim$ 3 μm change in σ_z. (b) ΔQ plotted as a function of ΔW^-, where each point corresponds to one of the six groups in (a). The corresponding groups in (a) and (b) are indicted by numbers above or below data points. The value of ΔW^- for each data point in (b) corresponds to the mean value of ΔW^- for a group in (a) and the mean of ΔQ for each group is plotted with the error bars representing the standard deviation of ΔQ in a group. (c) Correlation of X-ray yield and ΔQ data shown in (a). (d) Peak energy-gain ΔW^+ as a function of ΔQ for the same data. 1GeV is added to the raw ΔW^+ value to compensate for the head-to-tail energy chirp of the incoming electron beam. (e) Waterfall plot for data shown in (a). Each slice represents an integration of the spectra along the non-dispersive direction, which are sorted by ΔQ. The shot number is shown on the horizontal axis. The counts near the initial beam energy ($\sim$ 20.35 GeV) and the counts below the initial energy (energy loss area) are divided by ten and two, respectively, as indicated on the images. (f) Average transformer ratio, $\langle R \rangle = \Delta W^+ / \Delta W^-$ plotted for the same data set shown in (e). 44

2.7 (a) Measured energy spectra for the same shots as displayed in Fig. 2.5. The white line shows ΔW^- and ΔW^+, where each point represents moving average of 5 shots. (b) The measured average transformer ratio $\langle R \rangle = \Delta W^+ / \Delta W^-$ as a function of ΔQ 46

2.8 A density plot of a snapshot in the simulation. All densities are normalized to 2.7×10^{17} cm^{-3}. Rb II electrons in the area to the left of the red dashed line are made transparent, so that the deflection of the sheath due to the beam loading of excess charge is visible. Since the simulation is cylindrically symmetric, only $r > 0$ is shown in this image. Rb I electrons form the wake and are shown in grayscale while Rb II electrons, shown in green, are tracked separately from Rb I electrons. The color plots are restricted for better visibility of lower density features. 48

2.9 Comparison of simulations with and without Ar and secondary Rb ionization. (a) On axis electric field for the two simulations with the beam having propagated 12 cm in the plasma in each simulation. The red curve represents the value of the field where only ionization of Rb I is present. For the blue curve both ionization levels of Ar and Rb are included. (b) Same parameters plotted as (a), except that the frame represents a time at 30 cm of beam propagation. (c) The energy space of the beam at the end of the simulation for the beam loaded case. Peak energy loss of 8 GeV and energy gain of 12 are clearly observed. (d) is the same for the simulation without beam loading – i.e. secondary ionization injection. . . 51

2.10 (a)$\bar{\Psi}$ for the simulation frame shown in Fig. 2.9(a) for the case where no secondary ionization is present. Black curve shows the outline of radial location, where Rb I electron density corresponds to 50% neutral density, i.e. the bubble sheath for $\xi < 160$ μm. The spike in the region $165 < \xi < 170$ μm indicate the region over which the neutral Rb is ionized. (b) The outline of on-axis plasma density (blue) and $\bar{\Psi}$ (shown in orange) corresponding to the $r = 0$ line in (a). On axis density reaches 1 (indicating full ionization on axis) at $\xi = 165\mu$m. In the region 73.0 μm $< \xi <$ 144.8 μm, $\bar{\Psi} > 0.7$. Electrons born in this region that reach the back of the wake where $\bar{\Psi} \sim -0.3$ satisfy the trapping condition $\Delta\bar{\Psi} < -1$. . . . 53

3.1 Experimental setup. Toroidal charge monitors upstream and downstream of the plasma monitor the input and output charge. The inset shows the neutral density profile of lithium and helium in a nominally 30 cm long oven. The spectrometer is formed by the dispersive element (D) and a pair of quadrupoles (Q1, and Q2) used to focus particular energies. Cherenkov radiation is produced by the dispersed electrons in the 5 cm air space between two Si wafers marked (1) and (2) and is recorded by the camera C. An example of the drive beam spectrum before plasma interaction is shown as an inset. The electrons are dumped into the beam stop. An axicon optic was used to preionize the plasma (see Section 3.5). 58

3.2 Energy spectra resulting from the interaction of the drive beam and the 30 cm plasma. The spectra are from nominally identical conditions with the variation occurring because of shot- to-shot jitter in the linac. The solid black line indicates the initial drive beam energy at 20.35 GeV. The energy spread on the drive beam was 1.4% rms (see inset in Fig. 3.1 for example spectrum). Electrons with energy of 6.35 GeV are focused by the spectrometer's quadrupole magnets, and marked by thin dashed black line. The injected charge in (a) is identified with an ellipse and the peak energy loss is indicated by a thick dashed black arrow. (b) The energy distribution of injected charge peaks at 5.8 GeV and has an energy spread of 1.2 GeV FWHM (20%). (d) Energy gain can reach over 10 GeV, in which case the maximum energy of the injected charge is difficult to discern as it merges into and overlaps with the energy loss feature of the drive beam. The tilt angle observed in the injected beam is due to slight misalignment in the trajectory of of the beam with respect to the center of quadrupoles (Q1 and Q2 in Fig. 3.1). . 60

3.3 OSIRIS simulation results. (a) shows an r-z slice of the cylindrically symmetric simulation, where the e-beam has propagated 5.2 cm (halfway up the ramp). The color table for the drive beam electrons is shown below the figure. Lithium and helium electron densities are shown in blue and green, respectively. The process of helium electron injection can be observed. (b) r-z slice of simulation after the e-beam propagates 31.2 cm (20.8 cm in the plateau region). Color map for the beam electrons is displayed below the image. Lithium and helium electrons are shown with same color maps as (a). The helium electrons at the back of the wake are encircled with a dashed black circle. (c) Energy spread of the helium electrons after the e-beam propagates 31.2 cm. (d) The on-axis longitudinal electric field (red) normalized to 36 GV/m and the on-axis density of the helium beam (blue) normalized to 6×10^{19} cm^{-3}. The dashed black line indicates the useful accelerating field without beam loading. 63

3.4 Calculation of the region in space where the laser is intense enough to ionize helium atoms. (a) Blue solid line is the intensity profile of a 500 mJ, 100 fs laser pulse with a 40 mm wide flat top profile incident upon a 1.5 degrees axicon. The neutral density profiles of lithium and helium are overlaid on the intensity profile as dashed red and purple lines, respectively. (b) Ionization fraction contour (n_e/n_0) of helium subject to laser intensity in (a) calculated from the integrated ionization rate (Eq. 3.2) over 100 fs. 66

3.5 Spectra resulting from the interaction of the electron beam with (a) the 30 cm lithium vapor without preionization laser. (b) 30 cm lithium vapor with laser pulse preionizing the plasma. (c) 130 cm lithium vapor without preionization laser. (d) 130 cm lithium vapor with laser pulse preionizing the plasma. The energy focused by the quadrupoles of the spectrometer is marked with a dashed black line. The color table for (a) and (b) is defined by the top color bar and the one for (c) and (d) is defined by the bottom color bar. Injected charge is marked with solid black ellipses. 67

3.6 Spectra resulting from the interaction of the drive beam with the 130 cm long, 8×10^{16} cm^{-3} plasma. The energy focused by the spectrometer's quadrupole magnets are marked by the dashed black line. The solid black line represents the initial energy of the drive beam. The injected beam in each frame is marked with a solid black ellipse. The outer edges of the defocused beam electrons are traced with two dashed black curves. (a) Example of a narrow divergence feature disconnected from drive beam; the charge is 25 pC. (b) Highest observed energy of the injected charge with limited energy spread. (c) Example of a low divergence injected beam overlapping with the high-energy-spread accelerated drive beam electrons. 71

3.7 Emittance measurement for the injected bunch in the long plasma. (a) Blue circles indicate the values of σ_x at different values of energy for a single spectrum image, which is shown in the inset. The contour of the injected charge is identified by solid black line marked as (1). The dashed black contour identified as (2) belongs to the accelerated electrons of the drive bunch, which are focused by the imaging spectrometer at 24.3 GeV. The top and bottom horizontal black dashed lines in the inset correspond to the highest and lowest energies for which σ_x is calculated. Red dashed line represents the best fit to the data, resulting in emittance value of 36 mm-mrad. (b) Histogram of emittance values ($\epsilon_{n,x}$) for a dataset, where 65 data points belonging to the same dataset could be fit and measured. 72

4.1 The setup for the simulation 77

4.2 (a) A snapshot of density as a colormap 4.5 cm after propagation (immediately after the helium upramp). Helium electrons are represented with blue, the pre-ionized plasma with pink and the beam electrons with red-blue colors (color table shown only for beam electrons). (b) Injected helium charge in the simulation as a function of distance. The two distinct ionization and injection region are marked with (1) and (2). (c) The ξ location of highest transverse electric field for each frame in the simulation. The center of the electron beam density is at 272 μm. The region where no ionization in simulation is observed is clearly marked. (d) Transverse and total electric fields plotted at the location of highest transverse field in the blowout region for each frame in simulation. No ionization injection is observed in frames where $E_{tot} < E_{th} \approx 75\ GV/m$ 78

4.3 (a)Current profile of the injected helium charge after 17.6 cm of propagation in plasma. (b) Plot of on axis $\bar{\Psi}$ after 4.4 cm of propagation. The lowest and highest range of $\bar{\Psi}_i$ that lead to ionization and injection are marked as $\bar{\Psi}_{i1}$ and $\bar{\Psi}_{i2}$. The corresponding ξ where $\Delta\bar{\Psi} < 1$ is also marked for each case (c) Energy spectra for the injected helium electrons. (d) Energy spectra for the drive beam 82

4.4 (a) Measurement of injected charge as a function of distance in the simulations. The beginning of the helium impurity is set to zero. Sim1 is shown in blue, Sim2 in orange, and Sim3 in yellow colors. Same colors are used in all sub-figures(b) Total electric fields as a function of distance for the same three simulations. (c) The 80% plasma density contours for the same three simulations after 3 cm of propagation in the plasma in addition to the density color map of the initial drive beam. The location of ξ where the transition between full and partial blowout occurs is marked by an arrow for each case. 84

4.5 (a) Energy spectra for Sim1-3. The spectra in each case is shown 5.7 cm after the beginning of the helium region. The same colors used in all four figures (b) Current profiles of helium injected charge for Sim1-Sim3, with each curve normalized to the peak current for that case (I_p). The legend shows the value of peak current in each case in amps. (c) The value of Ψ_i corresponding to the pinch in each frame. The range over which no electrons are ionized and injected are marked by double-sided arrows. (d) The longitudinal field corresponding to the three cases. 87

4.6 Comparing the results of Sim3 and Sim4, where the helium density is increased by five folds. (a)Injected charge in the first bubble as a function of distance. Zero indicates the beginning of helium region (3 cm of initial beam propagation in both simulations). The same color is used in the rest of the sub figures (b) Current profile as a function of ξ for both simulations normalized to the peak value of current in each case. The value of peak current in each case is shown in the legend of the figure. (c) Helium spectra in the two cases after 5.7 cm of propagation from the beginning of helium region. (d) Longitudinal electric field compared in both cases. 89

4.7 Results of the 3D cartesian simulation after 6.2 cm of propagation. (a)Current profile of the helium electron beam in the simulation.(b) Energy spectral density for the helium charge in the simulation. (c) Longitudinal phase space (z, p_z) for the helium electrons. (d) Transverse phase space for the higher energy injected electrons (indicated by black lined rectangle in (c)), which is produced in the first oscillation cycle. 92

4.8 Comparison in cases with different width of plasma column. (a) 80% density contour of the simulations superimposed on the density color map of the initial electron beam (before interaction with plasma) (b) Total field as a function of distance. Zero corresponds to the beginning of helium impurity region for Sim3, corresponding to 3 cm of propagation in plasma. (c) Longitudinal electric field in the same cases as (a). Note that curves for $8R_{b0}$ and $2R_{b0}$ almost exactly overlap in the figures, resulting in $8R_{b0}$ data to be hidden from view under $2R_{b0}$ curves . 96

A.1 (a) Schematics of a lithium vapor heat pipe oven. The important components are marked on the schematic. (b) The lithium oven seen from the side, with hot lithium inside at $\sim 1000^\circ$ C. (c) Image of the lithium oven as installed in the experimental area at FACET 102

A.2 (a) Measured temperature profile of a 30 cm lithium heat pipe oven. (b) Corresponding lithium and helium density. (c) Measurement of temperature profile of a 130 cm lithium oven. The x axis indicates the distance from the center of the oven. (d) Lithium and helium density corresponding to profile in (c) 104

A.3 (a) Temperature measurement using a thermocouple for the rubidium oven. (b) Calculated rubidium and argon densities 105

B.1 The effect of betatron σ_r on the betatron oscillations. (a) Betatron oscillations for a beam with $\epsilon_n = 250$ mm-mrad, and $\sigma_r = 35$ μm, same as Fig. 2.3. (b) Betatron oscillations for a beam with $\epsilon_n = 250$ mm-mrad, and $\sigma_r = 60$ μm . . . 108

C.1 The phase space and the corresponding Courant-Snyder parameters of an electron beam with Gaussian distributions. Here, the transverse coordinate of interest is on the x axis and the corresponding divergence $x' = p_x/p_z$ is the y axis. 110

C.2 (a) An example of a double Gaussian fit to the horizontal lineout of a 6-pixel wide slice of the spectrum on LANEX. the image fitted is shown as an inset. The black lines indicate the outer extents of where the fit was performed. (b) $\sigma_r(E)$ for the same data. The value of the third point is obtained from the σ_r fitted to the lineout in (a). The dashed orange line is obtained by an optimization of the electron beam variables inside a plasma, which are then propagated to Lanex screen. Effects of foils and plasma down-ramp are included here 115

C.3 The downramp modeled after the real plasma downramp shown in blue. In orange, there is the evolution of σ_r as a function of distance. 117

C.4 Measuring the emittance of the electron beam. (a) Same as Fig. 3.6(b), zoomed in the region of interest. (b) σ_r plotted for various energies (blue filled circles) along with the spectra resulting from the optimization of electron beam parameters (ϵ_n,σ_r, and α) inside the plasma. The effects of the plasma down ramps, and the Be and Al foils are modeled as described above along with the effect of the quadrupoles 118

C.5 Measuring the emittance of the drive beam electrons that lost energy. (a) Raw image. Color table enhanced to improve the visibility of pinch region at $\sim$ 14.35 GeV. the black dotted lines indicate the outer extents of where the fits to the lineouts were performed (b) σ_r plotted for various energies (blue filled circles) along with the spectra resulting from the optimization of electron beam parameters (ϵ_n,σ_r, and α)=(584, 56, 0.06) inside the plasma. The effects of the Be and Al foils are modeled as described above along with the effect of the quadrupoles, but not the plasma ramp 119

List of Tables

2.1 Plasma and beam parameters in the experiment. and are calculated with $\sigma_z = 40\mu m$. L_{FWHM} is the full width at half maximum of the rubidium density profile (shown as an inset in Fig. 2.2) 27

2.2 Properties of scattering foils used in the experiment and their effect on normalized emittance and σ_r at the entrance of plasma. See text for how the normalized emittance is calculated. 30

3.1 The interaction parameters as predicted by the 3D nonlinear theory and as measured in the experiments for the short and the long oven. L is the length of the oven as measured using the FWHM of the density profile. All other symbols are defined in the text. The superscript 'th' and 'exp' designate values obtained from theory and experiment, respectively. The $E_{\mathrm{max}}^{\mathrm{exp}}$ for the short plasma is comparable to $E_{\mathrm{max}}^{\mathrm{sim}} \approx 36$ GV/m, the beam loaded peak electric field from the simulation (Section 4). Note that the experimental and simulation values denote those of a beam-loaded wake, whereas the theoretical values are for a wake that is not beam loaded. 69

4.1 Beam and normalizations parameters for all the simulations in this chapter. $n_0 = 2.5 \times 10^{17}$ cm^{-3} is the normalization density used in the simulation, i.e. $c/\omega_p = 10.65$ μm 76

4.2 Simulation parameters for demonstration of density scaling of the simulation. The length of the helium region includes the length of the ramps, whose length is also scaled for each density 83

4.3 Simulation parameters for the various plasma column width. H_2 Plateau Density for all cases is 2.5×10^{17} cm^{-3} 94

C.1 Name and location of the important points using the LINAC coordinates in meters. The P_{ext} refers to the plasma exit location, taken as half way down the downramp. QS 1 and QS 2 are the two quadrupole magnets used in the spectrometer. The distances shown indicate the middle of the magnets. The effective length of the magnets is 1 m. Lanex is the Lanex screen indicated in the text, and is used for emittance measurement, and Cherenkov is the the location of the Charenkov detection plane. 111

Acknowledgments

First and foremost, I would like to thank professor Joshi for mentoring and supporting me throughout the last six years. His generous support and advice has been an invaluable contributor to the advancement of my career, and I will always be indebted to him for this generosity and mentorship. He thought me the value of creativity and how a novel perspective elevates the scientific value of the results that at the first glance may appear unimpressive. I moreover learned about leading a scientific team, forming collaborations, and effectively working with others from him. He gave me the opportunity and funding to travel to a premier, world-class research facility, FACET facility of SLAC National Laboratory, and participate in many high profile experiments. I was further given the opportunity to be responsible for a funded experiment at FACET (E-217), and to present results and request experimental time from a review committee, something that I am sure few other students have had the opportunity to do before having a PhD. On the academic side, his tireless advocacy for his students and deep engagement with his students and staff instilled in me a deep respect for the instructional roles of an academic researcher.

I would also like to thank Ken Marsh, who acted as my day-to-day supervisor, and who I regard as the best experimentalist I had ever had the privilege of working with. His keen sense of critical elements in experimental design and his methodical approach to planning and executing experiments is something I aspire to as I continue in my own research career.

Dr. Chris Clayton is another member of the UCLA group who has been an invaluable part of my graduate education, and I will always be indebted to him for his keen insights, and brilliant ideas, and in his camaraderie that was greatly beneficial on the long nights spent in the FACET control room.

I would like to acknowledge Dr. Jessica Shaw and Jeremy Pigeon, who were my colleagues and provided me with great support and friendship, particularly through the first difficult years of the Ph.D. program.

Dr. Sergei Tochitsky, the senior researcher at the Neptune lab always provided much

valued insight and perspective on work and life, for which I am very grateful. As someone not directly involved with my research topics. his friendly point of view on my research encouraged me to become a better communicator and scientist.

Maria Guerrero was greatly helpul in navigating the administrative tasks at UCLA and I am indebted to her for enabling me to focus on my academic duties without worries about important and bureaucratic parts of the program. I am also indebted to her for her keen observations and kind encouragements throughout these years.

I am also thankful to other members of the UCLA experimental group Dr. Nuno Lemos, Chen-Kang Huang, Eric Welch and Elizabeth Abramyan for their friendship and support.

I am indebted to the plasma simulation group at UCLA, not only for providing me with the simulation codes and mentoring on how to use these code, but also for personally helping me with running particular simulation projects. In particular, I am grateful to Dr. Weiming An for QuickPIC code and teaching me how to run 2D cylindrical simulations. I am also grateful to Diana (Ligia) Amorim, without whom the 3D section of the simulation chapter of this thesis would not have been possible. I am also indebted to Professor Warren Mori, the head of the simulation group and I would also like to thank Dr. Frank Tsung and Dr. Xinlu Xu for fruitful discussions. The simulations presented in this thesis were performed on Hoffman Cluster, access to which was granted to me through the collaboration with the UCLA simulation group.

The experiments reported in this thesis would not have been possible without the assistance of our collaborators at SLAC. In particular Dr. Mark Hogan and Dr. Vitaly Yakimenko provided great leadership for the facility and the experiments. The team responsible for tuning and delivery of the electron and positron beam ensured the availability of the high energy density particle beams that enabled the experiments reported in this thesis. Drs. Mike Litos, Sebastien Corde, and Erik Adli capably took the responsibility for various experimental apparatus and were invaluable to performing the experiments reported in this thesis. Dieter Walz's experimental support and expertise was crucial for many components of the experiment. Dr. Christine Clarke was the link between SLAC administration and

users, and was a superb resource who guided us through the complex bureaucracy of the system. On a personal note, Drs. Clarke and Hogan worked tirelessly to enable me to be able to work at SLAC, and I am greatly indebted to them for their efforts. Dr. Selina Green compiled an accurate and dependable record of the fast-evolving experimental instrumentations at FACET and her website became the de facto encyclopedia with rich array of information about all aspects of the experiments. Drs. Joel Frederico and Spencer Gessner, who knew the FACET computer system better than almost anyone provided great friendship and have been instrumental in installing data acquisition system and analysis tools. Carl Lindstrom from the University of Oslo also provided invaluable expertise in understanding the electron beam behavior from the conventional accelerator perspective, and has also been a very good friend. I would also like to thank Patric Muggli from MPI in Munich for great discussions, both scientific, and philosophical.

Chapter 2 is a reproduction of a journal articled submitted for publication: N. Vafaei-Najafabadi, K. A. Marsh, C. E. Clayton, W. An, W. B. Mori, C. Joshi, W. Lu, E. Adli, S. Corde, C. I. Clarke, M. Litos, S. Green, S. Gessner, J. Frederico, A. S. Fisher, Z. Wu, D. Walz, and M. J. Hogan. Limitation on the accelerating gradient of a wakefield excited by an ultra-relativistic electron beam in rubidium plasma. (submitted to Physical Review Accelerators and Beams).

Chapter 3 is a reproduction of a journal article published with the following citation: N. Vafaei-Najafabadi, W. An, C. E. Clayton, C. Joshi, K. A. Marsh, W. B. Mori, E. C. Welch, W. Lu, E. Adli, J. Allen, C. I. Clarke, S. Corde, J. Frederico, S. J. Gessner, S. Z. Green, M. J. Hogan, M. D. Litos, and V. Yakimenko. Evidence for high-energy and low-emittance electron beams using ionization injection of charge in a plasma wakefield accelerator Plasma Physics and Controlled Fusion, 58: 034009, 2016.

The work at UCLA was supported by NSF grant PHY-1415386 and DOE grant DE-SC0010064. The simulations were carried out on the Hoffman cluster at UCLA. Work at SLAC was supported by Department of Energy contract DE-AC02-76SF00515.

Vita

2007	B.Sc. Engineering Physics (with Distinction), University of Alberta, Canada.
2010	M.Sc. Photonics and Plasmas, University of Alberta, Canada.
2010-2012	Post Graduate Scholarship-D from the Natural Sciences and Engineering Council of Canada, Government of Canada

Publications

C.E. Clayton, E. Adli, J. Allen, W. An, C. I. Clarke, S. Corde, J. Frederico, S. Gessner, S. Z. Green, M. J. Hogan, C. Joshi, M. Litos, W. Lu, K. A. Marsh, W. B. Mori, N. Vafaei-Najafabadi, X. Xu, and V. Yakimenko. Self-mapping the longitudinal field structure of a nonlinear plasma accelerator cavity. Nature Communications, 7: 12483, 2016.

S. Corde, E. Adli, J. M. Allen, W. An, C. I. Clarke, B. Clausse, C. E. Clayton, J.-P. Delahaye, J. Frederico, S. Gessner, S. Z. Green, M. J. Hogan, C. Joshi, M. Litos, W. Lu, K. A. Marsh, W. B. Mori, N. Vafaei-Najafabadi, D. Walz, and V. Yakimenko. High-field plasma acceleration in a high-ionization-potential gas. Nature Communications, 7: 11898, 2016.

N. Vafaei-Najafabadi, W. An, C. E. Clayton, C. Joshi, K. A. Marsh, W. B. Mori, E. C. Welch, W. Lu, E. Adli, J. Allen, C. I. Clarke, S. Corde, J. Frederico, S. J. Gessner, S. Z. Green, M. J. Hogan, M. D. Litos, and V. Yakimenko. Evidence for high-energy and low-emittance

electron beams using ionization injection of charge in a plasma wakefield accelerator Plasma Physics and Controlled Fusion, 58: 034009, 2016.

S. Gessner, E. Adli, J. M. Allen, W. An, C. I. Clarke, C. E. Clayton, S. Corde, J.-P. Delahaye, J. Frederico, S. Z. Green, C. Hast, M.J. Hogan, C. Joshi, C. A. Lindstrom, N. Lipkowitz, M. Litos, W. Lu, K. A. Marsh, W. B. Mori, B. O'Shea, N. Vafaei-Najafabadi, D. Walz, V. Yakimenko, and G. Yocky. Demonstration of a positron beam-driven hollow channel plasma wakefield accelerator. Nature Communications, 7:11785, 2016.

S. Corde, E. Adli, J. M. Allen, W. An, C. I. Clarke, C. E. Clayton, J.-P. Delahaye, J. Frederico, S. Gessner, S. Green, M. Hogan, C. Joshi, N. Lipkowitz, M. Litos, W. Lu, K. Marsh, W. Mori, M. Schmeltz, N. Vafaei-Najafabadi, D. Walz, V. Yakimenko, and G. Yocky. Multi-gigaelectronvolt acceleration of positrons in a self-loaded plasma wakefield. Nature, 524(7566): 442-445, 2015.

M.D. Litos, E. Adli, W. An, C. I. Clarke, C. E. Clayton, S. Corde, J.-P. Delahaye, R.J. England, A. S., Fisher, J. Frederico, S. Gessner, S. Z. Green, M. J. Hogan, C. Joshi, W. Lu, K. A. Marsh, W. B. Mori, P. Muggli, N. Vafaei-Najafabadi, D. Walz, G. White, Z. Wu, Z., V. Yakimenko, and G. Yocky. High-efficiency acceleration of an electron beam in a plasma wakefield accelerator. Nature, 515: 92, 2014. (Cover Article)

N. Vafaei-Najafabadi, K. A. Marsh, C. E. Clayton, W. An, W. B. Mori, C. Joshi, W. Lu, E. Adli, S. Corde, M. Litos, S. Li, S. Gessner, J. Frederico, A. S. Fisher, Z. Wu, D. Walz, R. J. England, J. P. Delahaye, C. I. Clarke, M. J. Hogan, and P Muggli. Beam loading by distributed injection of electrons in a plasma wakefield accelerator. Physical Review Letters, 112(2):025001, 2014.

CHAPTER 1

Introduction

1.1 Plasma Accelerators for the Colliders of the Future

In 2012, the Large Hadron Collider (LHC) performed a series of landmark experiments that proved the existence of the Higgs boson [1, 2]. The LHC is a 27 km circumference circular collider that collides two beams of protons, each having 7 TeV of energy. Fundamental discoveries such as this have tremendous implications for the understanding of the laws of this universe. This is because the discovery of such particles can confirm, or upend the Standard Model of particle physics, which encompasses the current understanding of the constituent fundamental particles that form the universe and the forces that act on them. Recent experiments performed in early 2016 at LHC for instance hinted at the existence of a new particle not predicted by the Standard Model, and if proven, it will lead to a second age of discovery in fundamental physics.

Since their inception, particle accelerators have arguably been the most important tool in scientific research and discovery, furthering our knowledge of elementary particle physics. The typical size of the particles that constitute the nucleus of an atom, i.e. protons and neutrons, is on the order of a femto meter (10^{-15} m). Therefore to see the substructure of the proton one needs a probe that has a characteristic wavelength far smaller than this. It is well known that an electron can be thought of as either a particle or a wave. As shown by de Broglie, the characteristic wavelength of a particle is related to its momentum by $\lambda = h/p$ where $p = \gamma mv$ is the particle momentum, m is the particle mass and h is the Planck constant. Therefore, a high energy particle can be used as a probe with a small wavelength. Indeed, it was only when particle beams with energies greater than a GeV became available

that one could probe on a scale smaller than the size of the proton and a whole ensemble of particles known as masons (later shown to comprise of quarks) were discovered. Another way to look at this phenomenon is that the constituents of matter have high rest mass, and so to generate them in a detectible way, one needs to start with high energy particles from the conservation of matter and energy.

In addition to particle physics discovery, particle accelerators have important application in chemistry and biology. In particular, particle accelerators are used to generate high brightness coherent/incoherent x-ray radiation (such as those in the Linac Coherent Light Source or synchrotrons) that can be used to conduct molecular crystallography in the fields of microbiology and chemistry or to study and model cracks, strain and corrosion in the field of materials engineering.

In order to tackle some of the most important problems in physics in this century, scientists will require high energy colliders of even greater energy than the LHC. The main challenges facing the building of the next generation of particle accelerators at the energy frontier of particle physics are going to be its cost and scale. The unloaded accelerating gradient of the room temperature RF-powered linear accelerator (LINAC) sections that comprise a particle collider is < 100 MeV/m. For superconducting structures such as those comprising the LHC the gradient is even smaller. As the gradient is increased beyond this value, the electric field tends to initiate breakdown and cause damage to the structure.

With regards to cost, the structure cost alone for the 27 km circumference LHC was over \$6 billion dollars, while the International Linear Collider (ILC), which is a 500 GeV e^-/e^+ collider, has a projected cost in excess of \$20B. Since the next generation particle accelerators would aim to reach even higher energies than those achieved at LHC or the ILC, the acceleration technology itself has to be revolutionized to enable miniaturization of the accelerator at a lower cost than currently possible to make the next-generation accelerators feasible.

As previously mentioned, the LHC accelerates and collides proton beams, but things get even more interesting with electron/positron colliders. The use of a e^-/e^+ collider in the

place of a hadron collider is desirable because the protons are composite particles, having been formed of sub-particles themselves. Thus during the collision, a slew of secondary particles are generated that greatly complicate the analysis and interpretation of data, adding to the ambiguity as well as the noise in the results. Additionally, the generated radiation means that the detectors cannot be placed near the point of collision because they would get damaged by the excess radiation caused by the secondary particle shower.

The LHC tunnel used to house an electron positron collider before being commissioned for acceleration of hadrons. The so called Large Electron Positron collider (LEP) collided positron and electron beams with about 100 GeV in each beam. However one cannot accelerate electrons or positrons in a circular machine far beyond this energy because these lighter particles lose energy to synchrotron radiation as they are accelerated in a circular orbit at a rate that scales as γ^4, where γ is the relativistic Lorentz factor. Therefore, a future particle collider would ideally have a linear geometry and would collide electron and positron beams.

If we assume that the loaded acceleration gradient of an RF superconducting linac can be increased to 50 MeV/m, to reach a 3 TeV center of mass energy the accelerator would have to be 60 km long. The collider would probably be twice this length because of the length of the final focusing optics. Thus the final length of the complete machine based on the extrapolation of the current technology is likely to be greater than 100 km. Such a gargantuan linear accelerator would almost certainly be prohibitively expensive. This fact was recognized by the accelerator community as early as in 1982 and search was underway to find particle acceleration techniques that had the potential to realize far higher acceleration gradients.

1.2 Plasma Wakefield Acceleration

In 1979, Tajima and Dawson proposed a method for accelerating electrons in a plasma wave [3]. Although this initial paper suggested using a laser pulse with the intensity of 10^{18} W/cm^2, it was soon followed by the suggestion of using an electron beam for the same

purpose [4]. This accelerating field in a plasma wave depends on $\delta n/n_p$, where n_p is the initial plasma density and δn represents the density perturbation in the plasma wave. In the limit of 1D cold wave breaking, which is the largest field that a plasma oscillation in a cold plasma can support, the accelerating field is on the order $eE/mc\omega_p = 1$. This elementary theoretical treatment suggests that the plasma wave can support electric fields on the order of 10 GeV/m at the density of $\sim 10^{16}$, which is more than two orders of magnitude higher than that in the conventional LINACs.

The plasma waves considered in the early work were mostly in the linear regime. The advantage of these linear waves is that its electric field can accelerate both electrons and positrons. In fact, the only difference in treatment of electrons and positrons would be the phase of the wake that would be both accelerating and focusing to either, which constitutes about 1/4 of the wavelength (a different quarter wavelength for electrons compared to positrons). The laser pulse intensity needed to produce the wake is frequently expressed in terms of the normalized vector potential of the laser $a_0 = eA/(mc^2)$.The quasi-linear regime is still being considered for acceleration of electrons and positrons using lasers, because it requires relatively low intensity lasers with $a_0 < 1$. On the other hand, once one uses a high intensity laser ($a_0 > 1$), or a high density electron beam (i.e. $n_b/n_p > 1$), the plasma wave quickly evolves to the blowout regime [5], where $\delta n/n_0 \approx 1$, i.e. all electrons are expelled from the region around the drive pulse (blowout). In fact, even if one starts with a relatively low density electron beam, or a linear wake, the plasma wave can evolve to blowout regime due to the phenomenon of self focusing, which occurs for the electron drive beam as it is propagating in the positively charged region of the wave, and for the laser driver due to the enhanced index of refraction of the positive region.

1.3 Forces in the Blowout Regime

The blowout regime has ideal properties for accelerating electrons and is therefore of great interest in the field of plasma accelerators. These properties can be explored using certain normalized parameters [6], where time is normalized to ω_p^{-1}, length to c/ω_p, velocities to the

speed of light c, mass to electron mass m, and charge to electron charge e, fields to $mc\omega_p/e$, potentials to mc^2/e, charge density to en_p, and current density to en_pc. For clarity, the normalized parameters are represented with an overbar.

The pseudo potential can defined as $\bar{\Psi} = (\bar{\Phi} - \bar{A_z})$, where $\bar{\Phi}$ is the electrostatic potential, $\bar{A_z}$ is the component of the vector potential along the direction of propagation, and a gauge is chosen such that $\bar{\Phi} \neq \bar{A_z}$. The coordinate system useful for this calculation is ($\xi = z - v_\phi t, x, y, s = z$), where v_ϕ is the phase velocity of the wake ($v_\phi \approx c$), and the driver is propagating in the s (or z) direction. Making the quasi-static approximation $\partial_s \ll \partial_\xi$, it can be shown that [6]

$$F_z \approx -\partial_\xi \bar{\Psi}, \tag{1.1}$$

$$F_\perp \approx -\nabla_\perp \bar{\Psi}. \tag{1.2}$$

An immediate consequence of the dependence of both longitudinal and transverse forces on $\bar{\Psi}$ is the Panofsky-Wenzel theorem, which states that under such conditions as expressed by Eq. 1.1 and 1.2,

$$\nabla_\perp F_z = \partial_\xi F_\perp. \tag{1.3}$$

In other words, the transverse variation of the longitudinal field is equal to the longitudinal variation of the transverse field.

By deriving an equation for Ψ in the blowout regime, we can describe the longitudinal and transverse forces. Using the equations of the vector potentials in the Lorentz Gauge, a 2D Poisson's equation can be derived for the pseudo potential Ψ:

$$-\nabla_\perp^2 \bar{\Psi} = 4\pi(\bar{\rho} - \frac{\bar{J_z}}{c}), \tag{1.4}$$

where $\bar{\rho}$ is the charge density and $\bar{J_z}$ is the z component of the current density.

Thus the transverse force (Eq. 1.2) can be found by integrating Eq. 1.4 in the transverse direction. Inside the blowout region, where $\rho = J = 0$,

$$F_\perp = -2\pi e^2 n_p x_\perp \tag{1.5}$$

This is an important equation, because it states that the electrons inside the blowout region feel only linear focusing force. A single electron in this field would perform simple harmonic oscillation motion. An ensemble of electrons would perform envelope oscillations and will have important consequences for the experimental results as will be described in detail in chapter 2. An important point is that this focusing force does not change with loading charge (often called beam loading) inside the blowout region, because the electric field of such a beam is balanced by its magnetic field. Figure 1.1 shows the properties of the fields in the blowout regime. The wake is produced by a dense bi-Gaussian drive electron beam with a peak $n_b/n_p = 1$, $k_p\sigma_z = 0.81$, $k_p\sigma_r = 1.1$, and $\gamma = 40,700$. Here, $k_p = \omega_p/c$ is the inverse skin depth of the plasma, $\omega_p = (\frac{n_p e^2}{m\epsilon_0})^{1/2}$ is the plasma frequency, ϵ_0 is the permittivity of free space, and $n_b = \frac{N}{(2\pi)^{3/2}\sigma_z\sigma_r^2}$ is the beam density, where N is the number of electrons in the bi-Gaussian bunch and σ_r and σ_z are the rms bunch width and bunch length, respectively [6]. A second trailing bunch with the same dimensions and $n_b/n_p = 0.5$ is following the first drive bunch.

An important consequence of the transverse force is its independence on ξ. Therefore, from the Panofsky-Wenzel theorem (Eq. 1.3),

$$\nabla_\perp F_z = \partial_\xi F_\perp = 0. \tag{1.6}$$

In other words, in the blowout regime, the accelerating force is uniform in the transverse direction. This property is very important in light of the fact that the linear transverse force in the blowout regime causes the electrons to perform radial oscillations (also called betatron oscillations). Regardless of what phase the electrons are in their oscillating cycle, they will see the same longitudinal force and get accelerated at the same rate. As it will be shown later, the betatron oscillation wavelength and frequency depend on the energy of the electron beam. So the transverse uniformity of the accelerating field allows for electrons starting with the same energy in a slice (i.e. same position in ξ) to maintain their energy uniformity, and maintain relative phase of oscillation while accelerating. This is an important quality that allows for the normalized transverse emittance of the beam, a measure of transverse quality of the beam defined in a later section, to be maintained as the electron beam is accelerated.

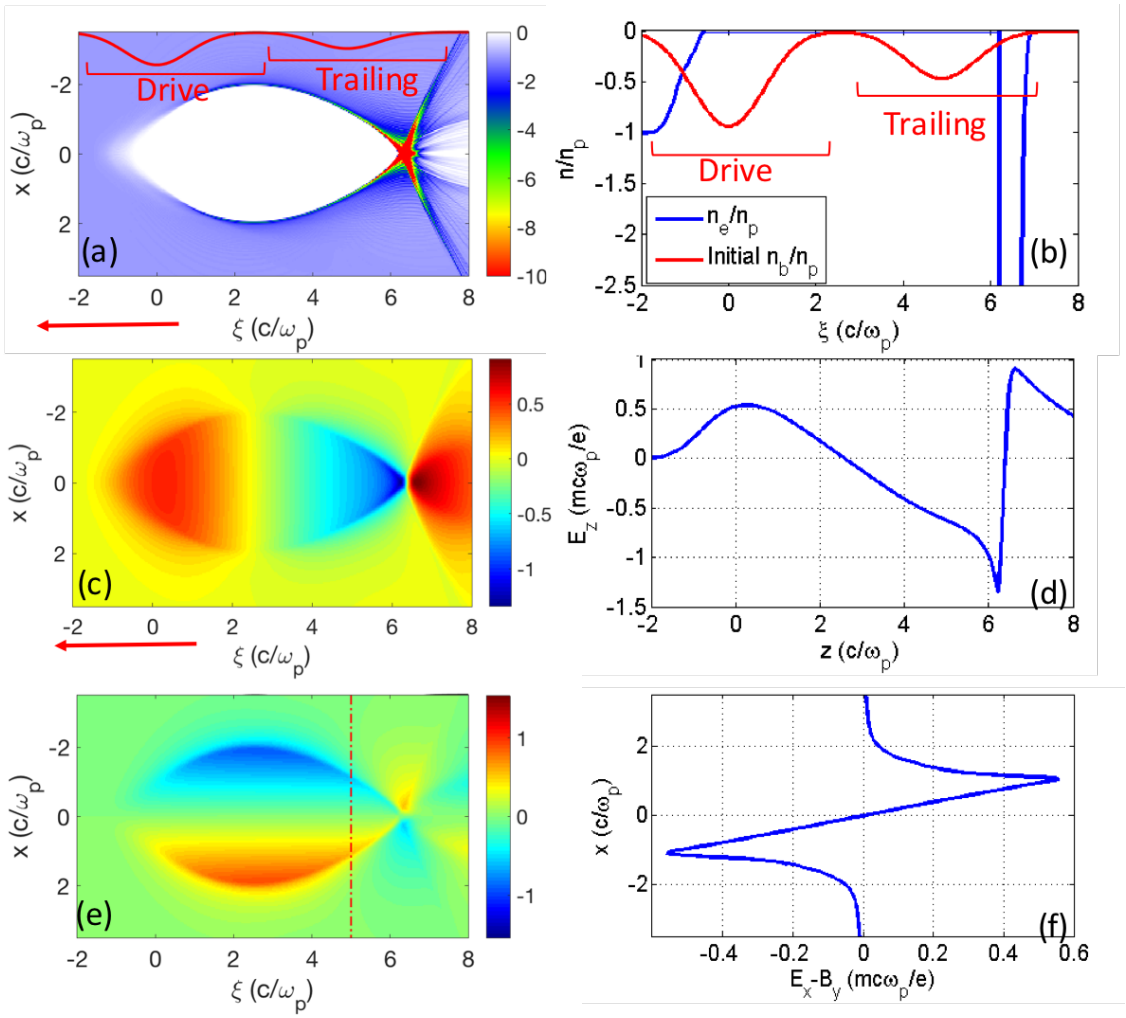

Figure 1.1: Properties of the blowout regime. (a) shows the plasma density color map for the simulation. The wake is propagating from the right to the left. The current density of the two bunches is superimposed in red. (b) shows the on-axis beam densities in red and the on-axis plasma density in blue. The region where plasma density comes to zero is the blowout region. (c) shows the color map for the longitudinal field $\bar{E_z}$. The radial uniformity of this field can be observed from the color table. (d) shows the on-axis electric field in the simulation. This field is modified(loaded) by the presence of the trailing bunch. (e) shows the transverse force $\bar{E_X} - \bar{B_Y}$. longitudinal uniformity of the transverse field can be observed in the color map. The red line at 5 c/ω_p indicates the location of lineout shown in (f). (f) shows the transverse lineout, which is linear and focusing for electrons.

As for the longitudinal force, using a phenomenological model of the blowout regime, Lu et. al [7] showed that the normalized scalar potential Ψ can be derived as

$$\bar{\Psi} \approx \frac{\bar{r_b}^2(\bar{\xi}) - \bar{r}^2}{4}. \tag{1.7}$$

Here, $\bar{r_b}$ is the blowout radius as a function of $\bar{\xi}$, and $\bar{r}$ is the transverse coordinate. This equation is valid for a relativistic blowout regime for a large maximum blowout radius ($k_p r_b \gg 1$), where the trajectory of r_b can be approximated as a circle. Combining this equation and Eq. 1.1, the longitudinal field can be calculated as:

$$\bar{E_z} = \partial_{\bar{\xi}} \bar{\Psi} = \frac{\bar{r_b}}{2} \frac{d\bar{r_b}}{d\bar{\xi}} \approx \frac{1}{2}\bar{\xi} \tag{1.8}$$

In un-normalized units, the peak accelerating field can be expressed as $eE_{\text{peak}}/(mc\omega_p) \approx \frac{1}{2}k_p R_b$, where R_b is the maximum of the blowout radius. The transverse and longitudinal forms of the force are shown in Fig. 1.1.

1.4 Electron Beam Driven Plasma Wakefield Accelerator

As shown in the last section, the forces of the blowout regime are ideal for creating an electron accelerator. The two primary drivers for a plasma-based accelerator are the particle beams and the laser beams. Although the experiments described in this thesis are restricted to electron beam experiments, it is useful to contrast the two drivers and discuss the advantages and disadvantages of using an electron beam driver compared to a laser pulse driver. As mentioned above, the maximum accelerating field is given by [7]

$$eE_{\text{peak}}/(mc\omega_p) = -\frac{1}{2}k_p R_b, \tag{1.9}$$

where R_b is the maximum blowout radius, m is the electron mass, e is the electron mass, c is the speed of light. In a bi-Gaussian beam with $k_p\sigma_z \approx 1$, $k_p\sigma_r \ll 1$,

$$k_p R_b \approx 2\sqrt{\Lambda}, \tag{1.10}$$

where Λ is charge per unit length given by $\Lambda = \frac{n_b}{n_p}(k_p\sigma_r)^2$. For the experiments explored in this thesis, σ_z and σ_r are both about 30 μm, and $N \sim 2 \times 10^{10}$ particles. Using these

parameters, $n_b = 4.7 \times 10^{16}$ cm^{-3}. However, the density used in the experiments in this thesis range from 8×10^{16} to 2.5×10^{17} cm^{-3}. Even though in these experiments, $n_b < n_p$, because of self-focusing of the driver mentioned previously, the experiment evolves into the blowout regime in than 1 cm according to simulations, which is much shorter than the 30-130 m plasma length . Figure 1.2 shows QuickPic simulations, where n_b was varied by changing σ_r, and it can been seen that different simulations with different initial beam densities (n_b/n_p) produce the same accelerating field once the blowout regime is established. The determining factor for the properties of the blowout regime is Λ, and if varied (by changing σ_z for instance), it would have a direct effect on the longitudinal accelerating field. Additionally, for the parameters mentioned above, the total energy per drive bunch is 65 J at a peak current of 13 kA. The peak power is therefore 650 TW, and these electron beams can be sent at 1-10 Hz to the Facility for Advanced Accelerator Experimental Tests (FACET) experimental area. This facility was a Department of Energy (DOE) designated User Facility, which used the first 2 km of the LINAC at the SLAC National Accelerator Laboratory to generate a 20 GeV electron or positron beam. Experiments were performed at this facility between 2012 and 2016.

Although in terms of average power, state-of-the art laser systems can produce pulses that compete with electron beams that were produced by FACET, the particle driven plasma accelerators have their own unique advantages. Whereas the Rayleigh length of a laser pulse, which is the length over which the cross-section area doubles, is usually less than a centimeter, the equivalent parameter for electron beams (called the β parameter) can be hundreds of centimeters long. This means that an electron beam can maintain a high energy density for a much longer distance without the need for external guiding, so it can drive a wake in a plasma for a much longer distance. For instance, while the longest interaction length in a laser driven plasma accelerator is below 10 cm (obtained using a plasma waveguide [8] or self-focusing of a laser in the plasma [9] to guide the laser pulse many Rayleigh lengths), the longest plasma wakefield accelerator (PWFA) driven by an electron beam is around 130 cm as will be reported in this thesis.

Figure 1.2: (a) Electron beam densities for three drive-witness simulations, where the witness beams are the same in all cases and the density of the drive beam is varied by varying σ_r; $k_p\sigma_r$ is 0.65, 0.98, and 1.3 for the blue, green, and red case respectively, corresponding to peak n_b/n_p of 2.1, 1, and 0.5 for the three cases. The value $\Lambda = 0.90$ is the same for all three cases. The beam propagation direction is indicated by a red arrow. (b) The resulting longitudinal field is presented for the three simulations in (a)

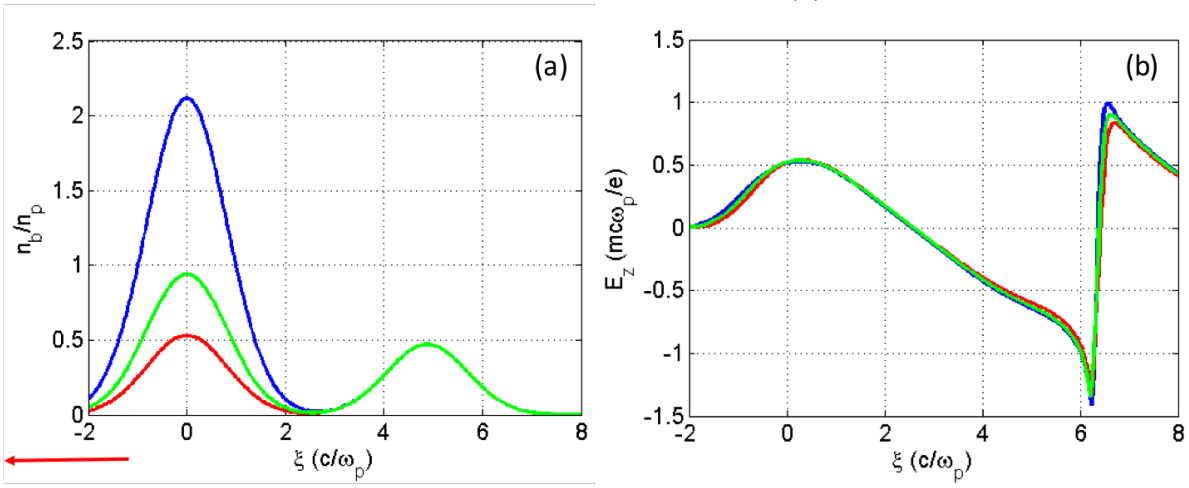

Another advantage of the beam driven PWFA is that the phase velocity of the wake is equal to the velocity of the electron beam, as opposed to the laser group velocity in plasma. In the case of the FACET beam, the drive beam has 20.35 GeV of energy, $\gamma_\phi = \gamma_b \approx 40,000$, where γ_b is the relativistic Lorentz factor for the beam and γ_ϕ is the Lorentz factor for the wake. On the other hand, for a laser driven wakefield, $\gamma_\phi = \frac{1}{\sqrt{3}}\sqrt{\frac{n_{cr}}{n_p}}$, where $n_{cr} = \epsilon_0 m\omega^2/e^2$ is the critical density, and ω is the laser frequency [10]. For a plasma wake at the density of 8×10^{18} cm^{-3} (usual for laser driven wakes), and a Ti:Saphhire laser, the phase velocity is $\gamma_\phi \sim 9.5$. The low value of γ_ϕ in a laser driven PWFA is a problem because as the accelerated electrons reach high energies, they start to outrun the laser and the wake. This effect put a limit on the accelerating length, which is called the dephasing length. However, due to the high γ_b, this effect is not a concern in an electron driven PWFA. Furthermore, for the same reason, the different ξ slices of the drive beam can be assumed to be stationary with respect to each other.

Another difference between the laser and the particle beam driver is that the electric field

of the particle beam is much lower than comparable laser pulses. The dominant component of the electric field, which is the radial electric field can be expressed as [11]

$$E_r^{\max} = 10.4 \left[\frac{\text{GV}}{\text{m}}\right] \frac{N}{10^{10}} \frac{10}{\sigma_r[\mu\text{m}]} \frac{50}{\sigma_z[\mu\text{m}]}, \tag{1.11}$$

which peaks at 10 GV/m for the parameters specified. In contrast, a laser with a wavelength of 1 μm and a power of $P = 650$ TW, focused to a FWHM of $w_{FWHM} = 45$ μm would have a peak intensity of $I_0 = 2P/(\pi w_0^2) = 2.8 \times 10^{19}$ Wcm^{-2} and an electric field of $E_r = \sqrt{2\eta I_0} =$ 15 TV/m, three orders of magnitude higher than the field of the electron beam. Here, $w_0 = w_{fwhm}/\sqrt{2\ln(2)}$ is the spot size and $\eta = 376.73$ Ω is the impedance of the free space.

This difference has important experimental implications for the electron beam driven plasma wakefield accelerators. The high intensity of the laser pulses allows for the plasma to be formed by the very early edge of the pulse, and so the entire pulse gets to interact with a uniform plasma. The low electric field of the electron beams means that this is not the case, and in fact a small number of elements of the periodic table, such as those in the alkali metal family, can get ionized by an electron beam in a way that allows for a substantial portion of the beam to interact with the resulting plasma.

On the other hand, the lower transverse electric field of an electron beam produces typically fully ionized but low-Z plasma, allowing a possibility of injecting electrons into the wake via the ionization of a second group of atoms within the wake in a process called ionization injection, which is described in the next chapter. Ionization of the second group can occur using the field of a relatively low intensity laser pulse, and it can result in an injected beam with extremely small transverse momentum [12, 13]. This is less straightforward to do with a laser driven wakes although various ideas have been proposed [14, 15].

1.5 Previous Work

What follows is a brief overview of the previous work in the field of plasma based accelerators. This section, which focuses solely on the use of plasma in interactions with an electron beam, is only a sampling of the extensive work that has been done in the field of plasma-based

accelerators since the idea was first introduced in1979 [3].

As mentioned previously, the first proposal for using an electron beam to drive a plasma wake for the purpose of electron acceleration was by P. Chen, J.M. Dawson et al [4], where 1D simulations were used to show the possibility of creating greater than 1 GeV/m acceleration gradients in a linear plasma wave in overdense regime (i.e. $n_b \ll n_p$). In the next few years, the properties of a linear plasma wave were further explored through 1D and 2D simulation and theory, including the study of the effect of a pre-defined electron bunch shape for driving or beam loading plasma wakes in order to obtain uniform acceleration and high energy transfer efficiency from the driver to the beam-load [16, 17].

This was followed by theoretical study of nonlinear 1D plasma waves [18], and the investigation of what came to be known as the "blowout regime", where all the electrons are expelled from the region immediately behind the drive beam [19]. As mentioned above, this regime was extensively studied in [6] (and references therein), where it was shown that it possesses ideal properties for use as an accelerating structure for electrons. The theory for beam loading in the blowout regime was then developed in [20], showing the possibility of very high energy extraction efficiency and low energy spread by a beam-load of appropriate shape that is placed judiciously in the blowout region.

The theoretical studies of PWFA in recent years have been greatly aided by high performance computer clusters, such as Hoffman 2 at UCLA, which is extensively used to perform simulations for this thesis. The massively parallel simulation codes that run on this cluster for the results presented in this thesis are comprised of 2D Cylindrically Symmetric OSIRIS [21] and QuickPIC [22, 23]. OSIRIS and QuickPIC are both a fully relativistic 3D particle-in-cell codes, but the difference is that QuickPIC uses the quasi-static approximation. At the time this thesis is written, trapping, which is an important component of the results presented in this thesis, is not modeled in QuickPIC, and so most of the results presented here are based on OSIRIS. These codes have been developed extensively by the UCLA Simulation Group of Professor Mori and IST in Portugal.

The first experimental evidence of a beam-driven plasma wakefield acceleration was ob-

served at the Argonne National Laboratory's Advanced Accelerator Test Facility [24]. In that experiment, an electron drive bunch with 2-3 nC of charge and 21 MeV of energy with $\sigma_r \sim \sigma_z \sim 2.4$ mm was used to drive a wake in a 20-35 cm plasma source (a DC hollow cathode source) with density of $n_p \sim 10^{13}$ cm^{-3}. A witness electron beam with 15 MeV of energy and having a variable delay with respect to the drive beam was used to sample the wake, and results showed that at the right phase, they could gain energy at the rate of ≈ 1 MeV/m. Thus this experiment showed the existence proof of the substantial longitudinal field of a plasma wake driven by an electron beam to accelerate electrons.

A drive beam with higher current density (4 nC, $\sigma_r = 1.4$ mm, and $\sigma_z = 2.1$ mm) was used in a followup experiment [25] to investigate accelerating and focusing properties of a nonlinear plasma wake. An accelerating field of up to 5 MeV/m was measured, and the focusing field was found to be capable of reducing the beam width to a third of its original size in half a betatron cycle.

The idea that the transverse force of a plasma wake can produce focusing gradients higher than MG/m prompted exploration of using a plasma wake as a lens to focus the electron drive beam. This idea was explored theoretically [26, 27], with experimental investigations occurring at various electron beam facilities around the world with energies in a few to tens of MeV range, including Argonne National Laboratory [25], Tokyo University [28], and at UCLA [29], where an electron bunch with 3.8 MeV of energy and a length of 3 c/ω_p was used to drive a plasma wake. Here, while the head of the beam created the plasma wake, the rest of the beam sampled the focusing force, showing that the transverse size of the beam can be reduced from an initial value of 2.7 mm to about 0.57 mm. This effect was consistent with the calculation of the transverse force of the wakefield, indicating the potential of the plasma wake to generate a much stronger focusing lens than the typical quadrupoles used in LINACs.

While the focusing and accelerating properties of the plasma wakefields were experimentally demonstrated using drive beams with tens of MeV of energy, the effort to combine plasma science with high energy physics, where particle beams with tens of GeV of energy

or greater are common, started at the Final Focus Test Beam facility (FFTB) at the SLAC National Accelerator Laboratory. Following on the demonstration of the focusing forces of the plasma wake, a collaboration of E-150 was formed to explore the application of plasma lens to high energy electron [30] and later positron beams [31]. In parallel, an experiment for demonstration of 1 GeV energy gain in a plasma source of 1-1.5m using the FFTB beam as a driver was proposed [32] and approved as E-157 experiment[33, 34].

The E-157 collaboration and subsequent experiments E-162, E-164, E-164X, and E-167 resulted in great advances in standing of the plasma wakefield accelerators as well as many milestones. The multi-GeV energy gain of electrons in a plasma wakefield accelerator was first observed in [35], and in a later experiment, accelerating gradients of 54 GeV/m were sustained in over 80 cm of plasma, resulting in energy doubling of a fraction of the originally 42 GeV electron bunch that was produced by the 3 km LINAC, bringing their total energy to over 80 GeV in less than 1 meter of plasma [36].

The various physics phenomena studied in the course of the FFTB experiments include the study of the transverse properties of the blowout regime [37], which demonstrated the oscillating behavior of the electron beam's envelope. The oscillating beam envelope, a consequence of the oscillating motion of electrons in the linear focusing force, resulted in x-ray radiation of tens of keV and up to tens of MeV as reported in [38] and [39], respectively. Moreover, the oscillation of the electron bunch in a radially offset plasma channel results in what is called the "hosing instability", which was studied using 3D simulations in [40].

Another important topic of investigation at FFTB was the ionization of various gases and elements by the high field of the electron beam. Initially, the ionization of the neutral species by the electron beam was studied as a possible means to generate a self-ionized plasma for PWFA experiments[11]. More importantly, it was discovered that ionization of neutral or ionic species within the blowout regime, which occurred as a result of the combination of the electron beam field and the field of the wake, could potentially lead to injection of such electrons and creation of high quality electron beam-loads in the wake [41, 42]. This latter discovery is of great significant for experiments laid out in this thesis as explained in the

next chapter.

The success of the experiments at FFTB led to the commissioning of the next facility at SLAC National Laboratory for the study of phenomena in plasma wakefield accelerators. This facility used the first 2 km of the SLAC LINAC and was called the Facility for Advanced Accelerator Experimental Tests (FACET). The experiments detailed in this thesis took place at FACET. Concurrent with the experiments detailed in this thesis were other plasma based electron acceleration experiments to which the author of this thesis heavily contributed. The most important was the drive-trailing (two-bunch) plasma based accelerator experiment (codenamed E-200), in which a dense electron beam was used to drive a wake in a plasma with 5×10^{16} cm^{-3} density, where a second electron bunch of 76 pC was loaded and accelerated at a gradient of 5 GeV/m, with a remarkable drive to trailing efficiency that approached 50% [43]. Another important experiment done by the E-200 collaboration was the demonstration of the longitudinally-uniform, linear focusing force in the blowout regime by studying the transverse properties of the electron spectrum. This study resulted in the first experimental verification of the Panofsky-Wenzel theorem (i.e. Eq. 1.6) in the blowout regime [44]. In another experiment from the same group, it was shown that the high gradients can be sustained in a self-ionized plasma produced in a higher ionization potential gas, such as argon or hydrogen, over an interaction length comparable to the β parameter of the beam in vacuum, which is much longer than the head erosion length (to be described in the next chapter) that was expected to limit interaction length in a self-ionized plasma [45, 36, 46, 47]. These experiments led to the approval of the next facility (FACET II), which is approved for commissioning, will encompass the middle km of the SLAC LINAC, and will produce the 10 GeV electron drive beam that will be used to study the next challenges in plasma wakefield acceleration such as generation and acceleration of low emittance, low energy spread beams, and staging of accelerating plasma sections.

1.6 Work Carried Out in This Thesis

Over a period of 6 years, the Plasma Wakefield Accelerator collaboration at the FACET facility at SLAC carried out a series of campaigns under the approved experiment called E-200. The work described in this thesis began as part of the E-200 but spun off as a second approved experiment called E-217. The author of this thesis was responsible for taking and analyzing the data described in this thesis. In addition the author made significant contributions to the development and operation of the lithium and rubidium plasma sources that were used by the entire collaboration. The main motivation for the work and the results are summarized below:

1) Beam loading of the wake due to distributed trapping of Rb II electrons: As previously mentioned, in electron beam driven PWFA experiments at FFTB, a dense electron beam generated over 85 cm of self-ionized lithium plasma, while at the same time driving a wake with an unloaded accelerating gradient of over 50 GeV/m [36]. The limiting factor in the acceleration length in that experiment was found to be a phenomenon called "head erosion", and not the energy depletion of the driving electron beam. This head erosion phenomenon will be explained in chapter 2, but in short, as a result of beam evolution, the electric field of the electron beam can only sustain ionization of lithium up to that distance.

Rubidium plasma source was investigated as a higher Z, lower ionization potential replacement for the lithium plasma source. Because of the lower ionization potential of rubidium, it was expected that the drive electron beam would ionize rubidium more easily than lithium. Furthermore, it was expected that the ease of ionization of rubidium would translate to longer self-ionized plasma, longer interaction length, and correspondingly higher energy gain.

However, envelope oscillation of the initially mismatched drive electron beam in the linear focusing force of the blowout regime resulted in the enhancement of the electric field and led to ionization of ions present in the blowout region (in the case of rubidium oven, these were Rb^{1+}, Ar, and Ar^{1+}). It has been shown that such electrons that are ionized within the blowout regime can get injected into the accelerating structure ([41, 48, 42]), whereas as it

will be shown later, the electrons ionized ahead of the blowout region cannot get injected in an electron beam-driven PWFA. This "ionization injection" resulted in formation of a "dark current" in the accelerating phase of the wake, and this unwanted beam loading resulted in reduction in the effectiveness of the accelerator as will be fully explained in chapter 2.

2) Ionization injection of helium electrons in lithium wakes and measurement of their emittance: Although the ionization of the rubidium electrons resulted in generation of dark current, this experiment also highlighted an opportunity to generate a beam load and inject it in the accelerating field in a controlled manner provided that the injection length is limited. This idea was explored in the lithium plasma, where the injection of electrons in the ramps of the lithium plasma was studied. In this region, the electron beam ionizes lithium atom and can drive a wake in the gradually increasing density ramp. The helium atoms do not get ionized by the field of the electron beam initially, but once the beam pinches due to the betatron oscillations, the increased electric field of the electron beam in addition to the electric field of the wake can ionize even helium. Once again, these electrons are injected in the wake, and get accelerated, but since the region of injection is limited to the ramp, the accelerating field does not get completely loaded and in fact, it remains in the range of $\sim 20 - 30$ GeV/m.

By studying the electron beam generated, we found that the emittance of the injected beam is much lower than the drive beam. The emittance (ϵ) of the accelerated beam is an important parameter that underlies its quality. In terms of phase space, the emittance is defined as the area of the electron beam. Therefore, an electron beam with very low emittance can be focused down to a very small spot size. In chapter 3, the results of the experiment are described in detail including the method that was used to measure normalized emittance of the generated electron beam.

The variable emittance in this sense is analogous to the wavelength for a laser. Emittance is an important physical parameter, because it is conserved during beam operations such as focusing, bending or free space propagation. Normalized emittance, which is defined as $\gamma_b \epsilon$, is conserved even during acceleration. Additionally, the emittance of the electron beam is an

important determinant of the applicability of the accelerated beam to areas such as creating x-rays in an FEL. This quality is measured by the parameter known as the brightness of the electron beam, which is calculated using $B = \frac{1}{8\pi^2}\frac{I}{\epsilon_x \epsilon_y}$, and therefore an electron beam with lower emittance has a higher brightness.

3) Generation of low energy spread and emittance beams by localized injection: Although the experiments showed the possibility of using ionization injection to obtain an electron beam with much lower emittance than the drive beam, the resulting electron beam still has a large energy spread. To investigate the possibility of creating electron beams with lower energy spread, a series of OSIRIS simulations were performed with an injection region that was reduced to a single beam oscillation cycle, thus reducing the length of injection and reducing the energy spread. As it is described in chapter 4, the energy spread can be reduced to a few percent, which in turn can help reduce the emittance growth during acceleration [14].

Finally, the effect of reducing the plasma width on the experiment is explored in simulation. This work aims to simulate the viability of axicon produced plasma in PWFA experiments, which as explained can have a width as low as 3 σ_r. Even though the pointing jitter of the laser was the limiting factor in the experiments with pre-ionized hydrogen plasma, the question remains whether under ideal conditions (i.e. perfect alignment and no jitter) a plasma column with small width can be used for the PWFA experiments. As part of the simulation work, we explored how the properties of the blowout regime change for such a narrow plasma. This latter simulation work has important implications on the experiments that seek to use axicon-like optics for ionization injection experiments.

In summary, this thesis aims to explore important challenges to the plasma-based particle accelerators using the data from the experiments performed at FACET, and the simulation codes OSIRIS and QuickPIC. This thesis experimentally investigates the viability of using a rubidium source for plasma-based wakefield accelerators, using ionization injection on the ramp of a lithium vapor source to generate low emittance electron beams, and finally use the simulations to demonstrate possibility of generating low-emittance electron beams in the

case of carefully controlled injection lengths.

CHAPTER 2

Limitation on the Accelerating Gradient of a Wakefield Excited by an Ultra-Relativistic Electron Beam in Rubidium Plasma

2.1 Introduction

The first phase of research on plasma wakefield accelerators (PWFAs) at the Final Focus Test Beam (FFTB) of the SLAC National Laboratory demonstrated the ability of a PWFA to achieve ultra-high acceleration gradients of over 50 GV/m [36] in a meter scale plasma. The experiments were carried out in the so-called blow-out regime [7, 19], where the electron beam density, n_b, was larger than the plasma density, n_p. In this regime, the drive-beam electrons expel plasma electrons, creating an ion cavity. A trailing electron beam placed inside this cavity will experience a linear focusing force, which preserves its transverse phase space and emittance, while (at the right phase) experiencing an accelerating longitudinal field. The maximum accelerating field is given by [7]

$$eE_{\text{peak}}/(mc\omega_p) = -\frac{1}{2}k_p R_b, \tag{2.1}$$

where R_b is the maximum blowout radius, m is the electron mass, e is the electron charge, c is the speed of light, and $k_p = \omega_p/c$ is the inverse skin depth of the plasma. In a bi-Gaussian beam with $k_p\sigma_z \approx 1$, $k_p\sigma_r \ll 1$,

$$k_p R_b \approx 2\sqrt{\Lambda}, \tag{2.2}$$

where Λ is the normalized charge per unit length given by $\Lambda = \frac{n_b}{n_p}(k_p\sigma_r)^2$. For a bi-Gaussian beam, $n_b = \frac{N}{(2\pi)^{3/2}\sigma_z\sigma_r^2}$, where N is the number of electron in the bi-Gaussian bunch and σ_r

and σ_z are the rms bunch width and bunch length, respectively [6]. Thus for the parameters used in [36], i.e. a plasma density of $n_p = 2.7 \times 10^{17}$ cm^{-3} and a drive beam with charge of $N = 1.8 \times 10^{10}$ electrons and $\sigma_z = 15$ microns, the expected gradient given by Eq. 1.9 is 82 GV/m. In the experiment the observed maximum gradient can be smaller than the above value if the electron bunch is not long enough to probe the highest value of the accelerating field as was the case in reference [36]. Nevertheless, electrons in the tail of the Gaussian drive beam were accelerated from an initial energy of 42 GeV (produced by the 3 km SLAC linac) to 85 GeV, i.e. some electrons doubled their energy in just over 80 cm, representing an average accelerating gradient of 54 GeV/m.

The interaction length in the above mentioned self-ionized PWFA experiment was limited by "head erosion". In self-ionization, the plasma is produced by the transverse electric field of the front (head) of the highly relativistic beam that also drives the plasma wake. Since the plasma electrons are expelled over a distance of $\frac{2}{k_p}\sqrt{\frac{n_p}{n_b}}$ [46], the blowout region, which is the region where electrons experience focusing force, forms behind the ionizing head of the beam. Therefore, the ionizing head of the beam does not experience this focusing force and expands due to the beam's inherent emittance. This expansion in turn reduces the transverse electric field at the head of the beam and as a consequence, the ionization front continuously moves back in the frame of the beam during the interaction. This effect is called beam head erosion [49], and in the extreme case, it can result in an interaction length that is smaller than the beam's β function in vacuum.

Head erosion is undesirable because it can effectively reduce the length over which the wake can be formed to a distance smaller than the pump depletion length – when the energy of the drive bunch particles is almost depleted and the bunch is no longer able to excite a wake. The head erosion speed of a matched beam (matching is defined later in the paper), V, depends on the normalized beam emittance ϵ_n, its current I, the beam energy γ_b, and the ionization potential (IP) of the medium being ionized [46, 49, 47] according to

$$V[\mu m/m] \propto IP^{1.73}[\text{eV}]\epsilon_N[\text{mm-mrad}]\gamma_b^{-1}I^{-3/2}[\text{kA}]. \tag{2.3}$$

For a given drive bunch, one can reduce the head erosion speed and thereby achieve a

longer interaction length by using a medium with lower ionization potential. Therefore, to potentially achieve larger interaction length than in reference [36], one could replace the lithium plasma source with one of the handful of elements that have a lower ionization potential. For example, the ionization potential (IP) of the first electron of Rb is 4.4 eV (compared to 5.4 eV for Li), so the SLAC electron beam is expected to propagate 40% further (and therefore give a correspondingly higher energy gain) in the beam-ionized Rb plasma compared to the previously used Li plasma according to Eq. 2.3.

This choice of Rb is also expected to reduce the problem of emittance growth of the accelerating beam due to ion motion [50, 51] in future PWFAs. In the present experiments, the plasma ions are assumed to remain stationary on the scale of the bunch length. However, in future experiments, it is expected that $n_b/n_p > m_i/m_e$, where m_i and m_e are the ion and electron mass, respectively. In such a case, the Coulomb force of the drive or the accelerating trailing electron bunch will cause the plasma ions to move toward the axis, degrading the linear focusing force of the ion cavity, and leading to the emittance dilution of the electrons. Since Rb atoms are 10 times heavier than the Li atoms, the use of Rb is expected to help mitigate the ion motion problem for high beam density experiments. It should be noted that even with the higher Z of the Rb ions, emittance growth due to small angle (electron-ion) scattering is not a serious issue for electron beam energies greater than 10 GeV [52].

For the two reasons given above, we tested a Rb plasma source for PWFA experiments at FACET. However, we expected that the maximum acceleration gradient of the wakes in Rb plasma may be smaller than the Li source. The origin of this effect is the smaller ionization potential of the Rb^{1+} (IP 27.3eV) compared to Li^{1+} (IP 75.6 eV). For a beam with $\sigma_z = 40\mu m$, the threshold field for the ionization of neutral Rb and Li are 3.0, 4.7 GV/m, and for Rb^{1+}, and Li^{1+} are 52 and 290 GV/m, respectively. Here, ionization threshold is defined as when the beam ionizes 10% of neutral atoms. The method for calculation of these values is explained later, but the important point is that the onset of the ionization of Rb ion can occur at a much lower electric field than for Li ion.

Furthermore, the electrons resulting from the ionization of Rb^{1+} ion (Rb II electrons)

are born inside the wake and can be accelerated by it. The ionization of Rb^{1+} ion within the wake occurs as a result of the combined effect of the wake fields and the beam field even if the beam field alone is below the threshold value for field-induced ionization. This injection of charge may be quite localized if the drive bunch is initially not matched to the plasma. As it will be shown later, if the drive bunch radius is larger than the matched radius, the bunch undergoes periodic envelope oscillations. Thus the ionization threshold of Rb^{1+} may be exceeded in the tightly pinched regions of each oscillation of the electron beam envelope [37] in the plasma, leading to the distributed injection of what amounts to "dark current".

While the distributed injection of this charge does not affect the decelerating field because of causality, it does reduce the accelerating field because of the beam loading effect [20] and reduces the average transformer ratio $\langle R \rangle$ [7]. In the experiments described here, $\langle R \rangle$ is reduced from its weakly loaded value of about 1.5 to 0.75. In the simulation, the reduction of the $\langle R \rangle$ is shown to be associated with the reduction of the maximum accelerating gradient from an unloaded value of 82 GeV/m to about 46 GeV/m. This problem is not unique to Rb. Indeed, other alkali elements with lower ionization potential considered to replace lithium in plasma wakefield acceleration face the same problem.

2.2 Beam Loading and Transformer Ratio

An important figure of merit for a beam-driven PWFA is the transformer ratio R, which is the ratio of the peak accelerating field to the peak decelerating field, i.e. $R = E^+/E^-$. In a non-evolving wake, this ratio also indicates the energy gained by a trailing beam or a 'beam load' in the accelerator to the energy lost by the drive beam. Since the total energy gained by the beam load cannot exceed the energy lost by the drive beam, the number of particles in the beam load must be less than $1/R$ of the number of particles in the drive beam. In other words, in a plasma wakefield accelerator, there is an inverse relation between the charge and the energy of the beam load, in an analogous way to the relationship between current and voltage on a load in a transformer– hence the term transformer ratio. It is well known that in the linear regime of the PWFA, R is less than two for symmetric beams and unloaded

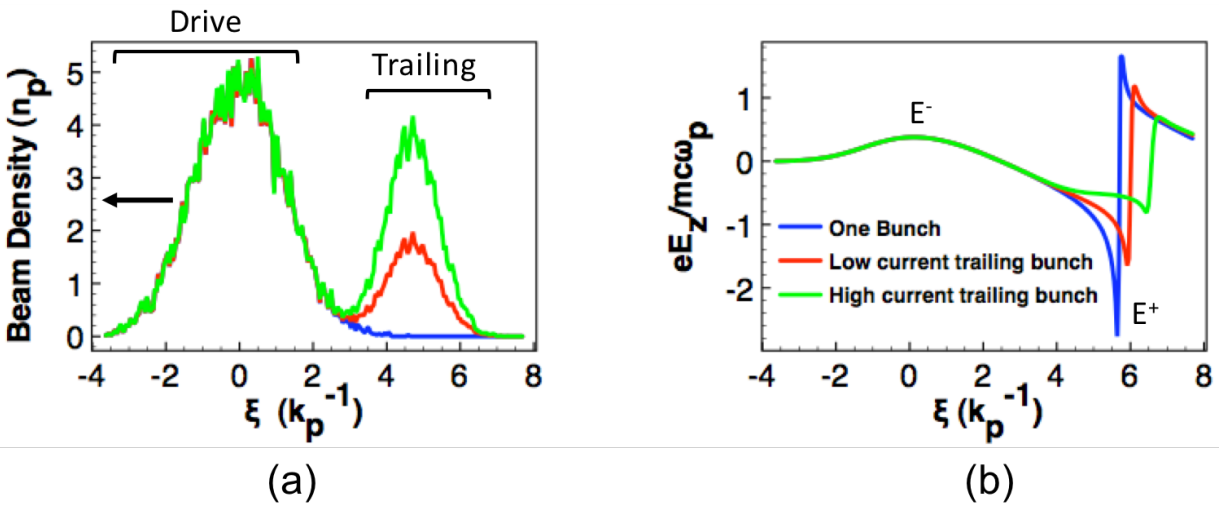

Figure 2.1: Beam loading in a drive/trailing electron-driven plasma wakefield accelerator (a) The longitudinal density profile of drive and trailing electron beams in three different beam loading scenarios. The drive beam density is the same ($n_b \sim 5n_p$) in all three cases. The three cases of trailing beam are: no trailing beam, i.e. unloaded wake (blue), trailing beam with peak density 40% that of the drive bunch (red), and trailing beam with peak density 80% that of the drive bunch (green). (b) The on axis longitudinal electric field for each of the three cases in (a). One can see progressively stronger beam loading that leads to flattening of the wake and reduction in the transformer ratio as described in the text.

wakes [53, 54], which means that 20 GeV electrons in the drive beam can at most add 40 GeV of energy to electrons that are being accelerated. In the nonlinear regime, $R > 2$ may be possible to obtain by the careful shaping of drive and trailing beams [55].

We first give a physical picture of beam loading and its effect on R since we shall use the average transformer ratio $\langle R \rangle$ to quantify the extent of beam loading in this work. As shown in Fig. 2.1 (figure originally appeared in [56]), the accelerating field of the wake can be locally flattened and reduced by the particles comprising the "beam load". The beam load may be provided by a second trailing bunch or it may be "dark current" injected from the plasma itself or some combination of the two.

Wake flattening due to beam loading is a necessary and indeed a very desirable effect

when it is caused by a second (trailing) bunch that is being accelerated. This is because flattening of the wake helps to reduce the energy spread. It is also necessary for an efficient energy extraction from the wake by the trailing beam as the energy previously stored in the electric field of wake is absorbed by the beam load. However, severe intentional or unintentional (dark current) beam loading will damp E^+ and drastically reduce R. For plasma wakes in the blowout regime, the amount of charge that is required to reduce the accelerating field of the wake from $E_{\rm peak}$ (as given by Eq. 1.9) to a flat value of E_s can be estimated using [20]

$$Q[nC] = \frac{0.047mc\omega_p}{eE_s}\sqrt{\frac{10^{16}}{n_p}}(k_pR_b)^4. \tag{2.4}$$

Using the parameters that will be relevant to the experiment, where the plasma density is $n_p = 2.7 \times 10^{17}$ cm^{-3}, the initial beam has $N = 1.8 \times 10^{10}$ particles with r.m.s. bunch length of $\sigma_z = 40$ μm, Eq. 1.9 can be used to obtain the values of $k_pR_b = 2.0$ and $E_{\rm peak} = 50.2$ GV/m. Therefore, reducing the peak accelerating field to $E_{\rm peak}/2$ requires $Q > 300$ pC and reducing it to $E_{\rm peak}/4$ requires $Q > 600$ pC according to Eq. 2.4. Note that this value is calculated for a charge with specific shape that produces a uniformly flat accelerating field for $\xi > \xi_i$, where $E(\xi_i) = E_s$ (similar to the case of the green curve in Fig. 2.1(b)). It is therefore possible for a wake to trap a much larger amount of charge if beam loading is nonuniform. Nevertheless, the values of Q calculated here give an indication of the amount of the charge that would cause heavy beam loading.

2.3 Ionization Injection into the Plasma Wakefield

An important problem in the field of plasma wakefield acceleration is to place an electron bunch – or the beam load – at an appropriate position in the accelerating phase of the plasma wake. The issue is that the wakefield moves through the plasma at a phase velocity equal to the velocity of the electron beam driver. For the 20.35 GeV electron beam at FACET, that represents a phase velocity with $\gamma_b \approx 40,000$. Therefore, the beam-load needs to be injected into the plasma wakefield with high enough γ_b such that it can remain in the accelerating

structure for a long distance. The process of electrons being positioned inside the wakefield with sufficient energy that will enable acceleration over a long distance is referred to as injection.

One method of injection into the wakefield is external injection. In this method, the second electron beam is separately prepared and accelerated to a sufficient energy such that it can move synchronously with the wake. This method was used at FACET to create a secondary bunch that extracted energy from a plasma wakefield at a gradient of 5 GeV/m and at efficiency of up to 30% [43].

The other method of injection is known as ionization injection. This method uses the large separation between the ionization potentials of two elements to produce electrons within a fully formed wake [41, 48]. The electrons from the element with the lower ionization potential are used to form the wake, while the element with the higher ionization potential is ionized within the wake, where the high accelerating field can impart enough energy to these electrons such that they travel near the phase velocity of the wake. The physics of ionization injection for such electrons was described by [41, 48]. The constant of motion for an electron interacting with the wakefield can be shown to be $\bar{H} = \gamma_b mc^2 - v_\phi P_z - e\Psi$, where v_ϕ is the phase velocity of the wake, $\Psi \equiv \Phi - \frac{v_\phi}{c} A_z$ is defined as the wake potential, where Φ is the electrostatic potential and A_z is the z component of the vector potential. For an electron born at rest with some initial Ψ to become trapped, i.e. $v_z = v_\phi$,

$$\bar{H}_i = \bar{H}_f, \tag{2.5}$$

$$1 - \frac{e\Psi_i}{mc^2} = \gamma_b - \frac{v_\phi P_z}{mc^2} - \frac{e\Psi_f}{mc^2}, \tag{2.6}$$

$$\Delta\bar{\Psi} + 1 = \frac{\gamma_b}{\gamma_\phi} = \frac{\sqrt{1 + (P_\perp/mc)^2}}{\gamma_\phi}. \tag{2.7}$$

Here, $\Delta\bar{\Psi} = \frac{e}{mc^2}(\Psi_f - \Psi_i)$ and $\gamma_\phi = (1 - (v_\phi/c)^2)^{-1/2}$. In the experiments , $\gamma_\phi \sim \gamma_b \sim 40,000$, meaning that transverse momentum remains much smaller than the longitudinal momentum, and the trapping condition simplifies to $\Delta\bar{\Psi} \leq -1$.

As it will be shown in the simulation section, this condition is only satisfied for electrons

Table 2.1: Plasma and beam parameters in the experiment. and are calculated with $\sigma_z = 40\mu m$. L_{FWHM} is the full width at half maximum of the rubidium density profile (shown as an inset in Fig. 2.2)

Parameter	Value
Number of electrons in drive bunch	1.8×10^{10}
$\sigma_z(\mu m)$	39-60
$\sigma_r(\mu m)$	35
n_b (cm^{-3})	2.3×10^{16}
n_p (cm^{-3})	2.7×10^{17}
$R_b(\mu m)$	21
L_{FWHM} (cm)	28

that are ionized within the wake cavity(also discussed in reference [42]). In other words, only for electrons that are born inside the wake is there a chance to get trapped by such a high-phase-velocity wake. In the present experiment, this ionization occurs via field ionization, because as will be shown later, the combined field of the wake and the evolving beam is strong enough to ionize Ar, Ar^{1+} and Rb^{1+} electrons, which will lead to their trapping since they can satisfy $\Delta\bar{\Psi} \leq -1$.

2.4 Experimental Setup

This experiment was performed at the FACET facility [57] at the SLAC National Accelerator Laboratory. The schematic of the experimental setup is shown in Fig. 2.2. The 3 nC, 20.35 GeV electron beam was focused on the rising density edge of a column of Rb vapor, which was generated in a heat-pipe oven [58]. The density profile of the Rb in the heat pipe oven is shown as an inset in Fig. 2.2. Also shown is the density of the Ar buffer gas, which confines the Rb to the hot region of the oven by cooling the Rb atoms via collisions. Accordingly, the density of Ar rises as the Rb density falls and vice-versa. The important beam and plasma parameters of the experiment are shown in Table 2.1.

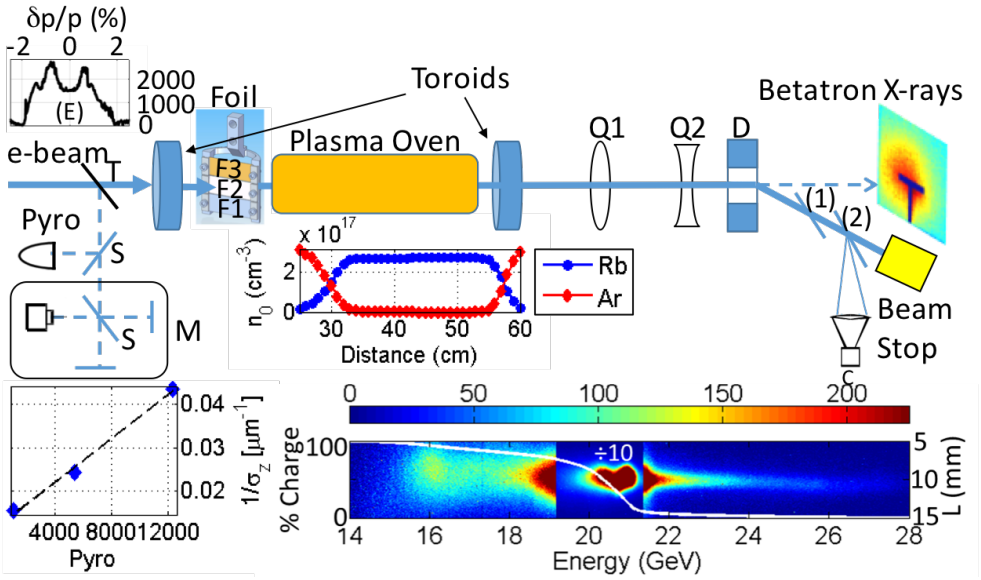

Figure 2.2: Experimental Setup. The electron beam enters from the left. The energy spectrum of the beam before plasma is shown as the inset (E) on the top left. Transition radiation generated as the beam traverses the 1 μm Ti foil (T) is observed simultaneously by a pyroelectric detector (Pyro) and a THz Michelson interferometer (M). Correlation between the pyro and the inverse of the bunch length deduced from the Michelson interferometer is shown beneath the setup. Foils with progressively higher scattering strength (F1-F3) can be inserted in the path of the beam before it enters the plasma oven, leading to progressively increased beam emittance (see Table 2.2 for details). The density profiles of neutral Rb and Ar are plotted underneath the schematic of the oven in blue circles and red diamonds, respectively. Absolutely calibrated toroids upstream and downstream of the plasma record the amount of charge entering and exiting the plasma. The quadrupole magnets Q1 and Q2 along with the dipole magnet D form the imaging energy spectrometer. The Cherenkov radiation emitted by the dispersed electrons between silicon wafers (1) and (2) is detected by camera C to give the electron spectrum after the plasma. An example of the energy spectrum with the white curve showing the integrated charge is shown below camera C. The charge near 20.4 GeV has been attenuated by a factor of 10. The Lanex screen, shielded by a 1mm copper foil, detects the betatron x-rays.

The normalized emittance of the beam in the experiment is manipulated by inserting foils (F1-F3) in the electron beam path 65.2 cm upstream of the plasma source and the waist. Because the head-erosion rate is a function of emittance (see Eq. 2.3), these foils are used to change the head-erosion rate, and consequently the distance over which the wake is excited by the beam – or the interaction length. The scattering of the electron beam as it goes through a foil can be modeled using the rms multiple scattering angle ($\Delta\theta$), which can be calculated using the standard formula [59]. Using this model, and the values of the vacuum waist and emittance $\sigma_r^* = 35$ μm and $\epsilon_n \sim 250$ mm-mrad, respectively, the values of ϵ, and the Twiss parameters (α, β, and γ) can be calculated using:

$$\epsilon = \epsilon_n/\gamma_b, \tag{2.8}$$

$$\beta = \sigma_r^2/\epsilon, \tag{2.9}$$

$$\gamma = \frac{1+\alpha^2}{\beta}. \tag{2.10}$$

At the waist, $\alpha^* = 0$, $\beta^* \sim 0.19$ m, and $\gamma^* \sim 5.1$ m^{-1}, where the $*$ denotes the values at the waist. The propagation of the Twiss parameters in vacuum can be calculated using

$$\begin{bmatrix} \beta \\ \alpha \\ \gamma \end{bmatrix} = \begin{bmatrix} 1 & -2L & L^2 \\ 0 & 1 & -L \\ 0 & 0 & 1 \end{bmatrix} \begin{bmatrix} \beta^* \\ \alpha^* \\ \gamma^* \end{bmatrix}, \tag{2.11}$$

At the location of foil, where $L = -65.2$ cm, i.e. 65.2 cm upstream of the plasma entrance, the Twiss parameters are $\alpha_v = 3.3$, $\beta_v \sim 2.4$ m, and $\gamma_v \sim 5.1$ m^{-1}. Here, the subscript 'v' denotes the values in vacuum (i.e. no foils), and L=-0.625 m. The change in the Twiss parameters due to a foil is given by equations [60, 61, 62]

$$\epsilon_f = \sqrt{\epsilon_v(\epsilon_v + \beta_v\Delta\theta^2)}, \tag{2.12}$$

$$\beta_f = \beta_v\epsilon_v/\sqrt{\epsilon_v(\epsilon_v + \beta_v\Delta\theta^2)}, \tag{2.13}$$

where the subscript 'f' denotes the values at $L = -0.625$ m in the presence of the foil. Finally, using Eq. 2.13, 2.11, and 2.9, the value of the σ_r at the entrance of the plasma after propagating through a foil can be calculated. The properties of these foils and their effect

Table 2.2: Properties of scattering foils used in the experiment and their effect on normalized emittance and σ_r at the entrance of plasma. See text for how the normalized emittance is calculated.

Name	Composition	Thickness (μm)	$\Delta\theta$ (μrad)	ϵ_n (mm-mrad)	σ_r (μm)
No Foil	———	———	———	250	35
Foil 1	Nicusil 3(71.15 Ag/28.1 Cu/0.75 Ni)	25.4	35	302	58
Foil 2	25/75 Au/Cu	50.8	58	377	64
Foil 3	Nocoro 80 (81.1 Au/16 Cu/2 Ni)	38.1	64	399	66

on the emittance and σ_r at the entrance of plasma are shown in Table 2.2. Note that these emittance numbers are similar to those calculated in [63], which used the simulation code ELEGANT to calculate the value of the normalized emittance and σ_r due to the foils.

Data from the following diagnostics, which were recorded for every data point, will be used in this paper: the charge monitor (toroids), the electron energy spectrum before and after plasma, the X-ray yield (betatron screen), and the bunch length (σ_z) from the pyro detector, all of which are shown in Fig. 2.2.

The bunch length (σ_z) was measured on every shot using a pyroelectric detector (pyro), which detected the coherent transition radiation (CTR) that was generated as the electron beam traversed a 1 μm thick titanium foil. The CTR signal varies as N^2/σ_z [35], and since the number of electrons, N, is nearly constant during the experiment, the variation in pyro correlates with a variation in $1/\sigma_z$. This linear relationship between the pyro and inverse bunch length was confirmed in the region of interest using a THz Michelson interferometer ([64]), which could monitor the CTR simultaneously with the pyroelectric detector as shown in an inset in Fig. 2.2.

The incoming and outgoing charge were measured upstream and downstream of the plasma using toroidal current monitors – toroids. By comparing the charge upstream and downstream of the plasma, we measured any "excess charge" generated during the experiment.

The energy spectrum of the electron beam after the plasma was measured using an imaging spectrometer. The spectrometer included a dipole magnet, which bent and dispersed the electrons according to their energy, and a pair of quadrupole magnets, which focused electrons at a specific energy. As the dispersed electrons propagate through the air, they generate Cherenkov emission. This broadband visible light emitted by the electrons between a pair of Si wafers 5 cm apart was imaged by a lens onto a CCD camera to record the dispersed spectrum of the electrons. These dispersed spectra are analyzed for the maximum energy gain and the maximum energy loss. The maximum energy gain $\left(\int E^{+}_{\max} dl\right)$ and the maximum energy loss $\left(\int E^{-}_{\max} dl\right)$ for each shot are defined as the 2% and 98% contours of the integrated Cherenkov signal, and an example is shown as a white curve on the spectrum in Fig. 2.2.

The x-rays generated during the betatron oscillations [38, 39] by the electrons in the ion cavity of the wake were detected using a Lanex film after the plasma. To measure the x-ray signal generated during the betatron motion only, the region of Lanex screen that showed radiation in the absence of plasma was blocked; this region is shown as solid blue T-shaped region on the betatron x-rays diagnostic in Fig. 2.2. A significant portion of this blocked radiation comes from the upstream and downstream quadrupoles and other magnets in the beam-line. The remaining x-ray signal is mostly due to betatron emission. This x-ray signal is then normalized for the amount of the beam charge that actually resides inside the wake and therefore generates betatron radiation. This "participating charge" is found by subtracting the charge that has lost no energy from the total amount of charge on the dispersed electron spectrum. This process is explained later in the paper. The resulting x-ray yield is used as a measure of x-rays generated per electron in the experiment.

Finally, the spectrum of the electron beam before the plasma was recorded in each shot.

This spectrum was measured in a region of the linac with significant spatial dispersion resulting in a correlation between energy and the transverse coordinate. The beam is then sent through a magnetic chicane, resulting in emission of synchrotron radiation by these electrons. The radiation is captured using a screen of YAG:Ce crystal, and because of energy chirp of the beam, the brightness of the x-rays corresponds to the current verses energy of electrons. This spectrum may be used for the recovery of the longitudinal beam profile using the LITRACK simulation code [35]. In these experiments however, the beam spectrum was merely used to isolate data points with nearly identical spectra (and therefore longitudinal profile) in different datasets. Additionally, because of the relationship between the pyro signal and the bunch length, the similar YAG spectra were seen within a narrow range of the pyro signal.

2.5 Physics of Distributed Injection

Comparing the toroids upstream and downstream of the plasma shows that a large amount of excess charge (ΔQ) is generated during the experiment. The physics of generating this excess charge can be explained by exploring the beam evolution through the plasma.

In the absence of the foils (F1-F3), the electron beam enters the Rb gas column with $\sigma_r \sim 35$ μm and $\sigma_z \sim 40$ μm. The value of σ_z is inferred from the pyro signal using the calibration curve shown in Fig. 2.2. The value of σ_r is measured using the SLAC wire-scanner diagnostic [65] near the beam waist.

The peak electric field of an electron beam with bi-Gaussian profile can be expressed as [11]

$$E_r^{\max} = 10.4 \left[\frac{\mathrm{GV}}{\mathrm{m}}\right] \frac{N}{10^{10}} \frac{10}{\sigma_r[\mu\mathrm{m}]} \frac{50}{\sigma_z[\mu\mathrm{m}]}, \tag{2.14}$$

where N is the number of electrons in the bunch. For the electron beam used in these experiments, $N = 1.8 \times 10^{10}$. The ionization rate of an element due to this electric field can be accurately modeled using the ADK formalism [11, 66]

$$W(s^{-1}) = 1.5 \times 10^{15} \frac{4^n \mathrm{IP(eV)}}{n\Gamma(2n)} \left[20.5 \frac{\mathrm{IP}^{3/2}(\mathrm{eV})}{E(\mathrm{GV/m})} \right]^{2n-1} \times \exp\left[-6.83 \frac{\mathrm{IP}^{3/2}(\mathrm{eV})}{E(\mathrm{GV/m})} \right], \quad (2.15)$$

$$n_e = n_0 \left[1 - \exp\left(- \int W dt \right) \right]. \quad (2.16)$$

Here, E is the electric field, IP is the ionization potential, Γ is the mathematical gamma function, and $n = 3.69Z/\mathrm{IP}^{1/2}$ is the effective principle quantum number, with Z the state of ionization, i.e. equal to 1 for a single ionized atom, n_e is the electron density, and n_0 is the initial neutral density.

Thus the ionization rate of various ionic species of elements in our experiment can be obtained for different electric fields (E) using Eq. 2.15 and is plotted in Fig. 2.3(a). The peak rate of 10^{14} s^{-1} will result in full ionization for an electric field with a Gaussian profile and with $\sigma_z = 40$ μm. Therefore, from Fig. 2.3(a), E_0 of approximately 4 GV/m fully ionizes the first electron of the Rb atom (Rb I).

The ionization fraction contours for an electron beam with $\sigma_z = 40$ μm and $\sigma_r = 35$ μm are plotted in Fig. 2.3(b). It is clear that a portion of the beam's electrons in the front of the beam cannot ionize the Rb atoms since the beam's electric field up to this front is below the threshold value needed for ionization. These electrons, called the unaffected charge, therefore propagate through the Rb column with unmeasurable energy loss and appear at 20.35 GeV on the spectrometer screen. The rest of the charge, which we call the participating charge will not only produce the plasma but also the wake and in doing so these electrons will lose some of their energy. Using the ADK model described above, we can define an ionization threshold as the location where 10% of the neutral atoms are ionized. It is then possible to estimate the amount of participating charge in the Gaussian profile by calculating the charge contained in the beam where the ionization threshold is exceeded. For a beam with $N = 1.8 \times 10^{10}$, $\sigma_z = 40$ μm and $\sigma_r = 35$ μm (without any foils), the value of participating charge is $N^* = 1.3 \times 10^{10}$ electrons, i.e. 72% of the initial charge. It is important to note

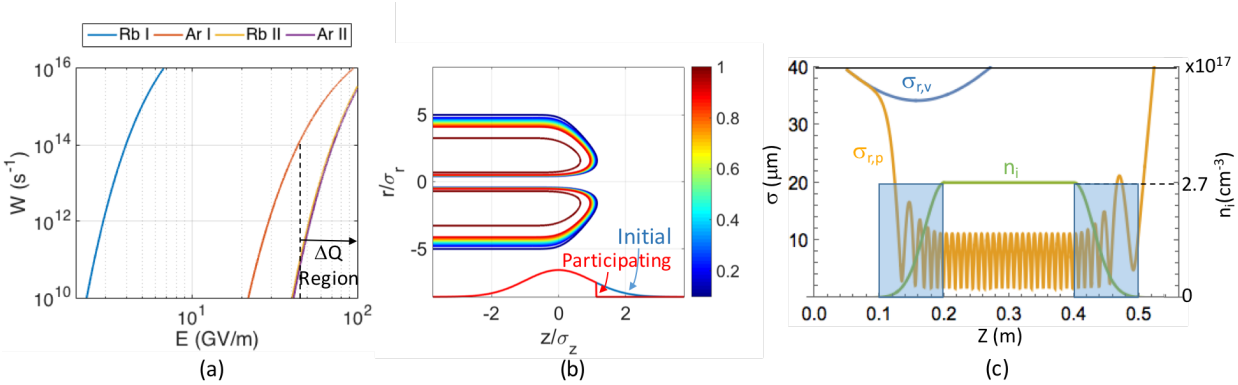

Figure 2.3: (a) Ionization rates for neutral Rb, neutral Ar, Rb^+, and Ar^+ ions as a function of electric field. (b) The ionization fraction for neutral Rb using an electron beam with $\sigma_z = 40$ μm and $\sigma_r = 35$ μm. The rates are obtained from ADK model. The longitudinal profile of the initial beam is shown in blue lineout and the longitudinal profile of the participating charge is shown in red lineout. (c) Envelope evolution of a beam slice with normalized emittance of $\epsilon_n = 250$ mm-mrad in an ion column with ion density n_i having the same profile in z as the rubidium plasma. The plot of density is shown in green. The propagation of the electron beam in vacuum and in the presence of blowout regime is shown in blue and orange, respectively. Regions with significant presence of Ar are shown in blue shade. The beam size below $\sigma_r < 7.9$ μm ionizes neutral Ar and $\sigma_r < 4.5$ μm ionizes Ar^{1+} and Rb^{1+}.

that the peak current of the participating charge is the same as the original beam (red curve in Fig. 2.3(b) vs blue curve in Fig. 2.3(b)).

The bulk of the participating charge resides in the fully formed wake or the ion cavity where it experiences a linear transverse focusing force [7]. In other words, once the ionization threshold is exceeded, the beam electrons rapidly ionize the Li atoms and blow out the plasma electrons. The evolution of the beam envelope in this ion column is described by [67]

$$\frac{d^2r}{dz^2} + k_\beta^2 r = \frac{\epsilon_n^2}{\gamma_b^2 r^3}, \tag{2.17}$$

$$k_\beta = \frac{\omega_p}{c}\frac{1}{\sqrt{2\gamma_b}}. \tag{2.18}$$

A beam with the transverse size equal to the matched spot size, given by $\sigma_{r,\mathrm{matched}}^2 = \epsilon_n(c/\omega_p)\sqrt{2/\gamma_b}$, would maintain its transverse size while propagating in the plasma because its tendency to expand due to emittance is exactly balanced by the focusing force of the plasma ions. For our typical experimental parameters – taking ϵ_n as 250 mm-mrad- $\sigma_{r,\mathrm{matched}} \sim 4\mu$m. Since the input beam radius in the experiment is larger than the matched spot size, the beam envelope's radius initially collapses as it enters the density up-ramp of the Rb column and then oscillates at half of the betatron wavelength ($\lambda_\beta = 2\pi/k_\beta$) as shown in Fig. 2.3(c). In the uniform density region ($n_p = 2.7 \times 10^{17}$ cm^{-3}) of our experiment, $\lambda_\beta = 1.8$ cm. Note that the presence of the ramp causes a reduction in the amplitude of the envelope oscillation down to about 10 μm, which is less than half of R_b as stated in Table 2.1. This is important because the focusing force implicit in Eq. 2.17 applies to electrons within the blowout region ($r < R_b$) only.

As the radius of the beam envelope decreases, the electric field of the beam increases according to Eq. 2.14, which results in an increase in the ionization rate according to Eq. 2.15. The different species can then be ionized inside the wake when the integrated ionization rate exceeds the threshold for their ionization. These species are the second electron of rubidium (Rb^{1+} to Rb^{2+}) and the first and second electrons of argon buffer gas in the density up and down ramps. Using the current profile shown in Fig. 2.3(b), the radius at which the ionization fraction of various species would surpass a threshold of 10% can be calculated. For instance, neutral Ar is ionized when $\sigma_r < 7.9$ μm and Ar^{1+} and Rb^{1+} are ionized when

$\sigma_r < 4.5$ μm. These electrons are ionized within the wake, gain energy from the wakefield, and can accumulate at the rear of the wake [41] as the electron drive beam executes more and more betatron oscillations.

Argon electrons are ionized and trapped in the ramp region only. The electrons resulting from ionization of Rb^{1+} on the other hand are ionized and captured at every cycle of the betatron oscillations, and with the betatron wavelength of 1.8 cm, this represents about 22 discrete regions (there are two envelope oscillations per betatron wavelength, which is defined for the oscillatory motion of a single electron in the ion column) along the density plateau of the plasma when σ_r goes below 4.5 μm. This means that unlike Ar electrons, Rb II electrons can be generated and injected in a distributed fashion along the length of the beam-plasma interaction. Therefore, in this scenario, the injection of Ar electrons is localized to the ramp regions, whereas the amount of the injected Rb electrons is proportional to the interaction length.

One way to circumvent the ionization and injection of this secondary charge in future experiments is to use a large matched beam. This could be done by increasing the emittance or reducing the plasma density or by a combination of the two.

In addition to causing secondary ionization of Rb, the betatron oscillation of the electrons in the blowout region generates x-ray radiation because of the transverse acceleration of the electrons due to the linear focusing force of the ion column. Most of the radiation is emitted at the extrema of the electron orbit where the velocity is zero and the acceleration is maximum. The average energy radiated by a single electron in the blowout region can be calculated from [68]

$$W_s = \bar{P}_s \times t = \left(\frac{e^2c^2}{12}\gamma_b^2 k_p^4 r_0^2\right)\left(\frac{N_\beta \lambda_\beta}{c}\right), \tag{2.19}$$

where the first factor represents the average power generated by an electron in a betatron cycle, and the second factor represents the interaction time. In this expression, N_β is the number of betatron oscillations, γ_b represents the energy of the participating charge, and r_0 is the amplitude of an electron's oscillation in the blowout region. In other words, for a given plasma density and beam energy, the amount of radiation depends on the interaction

length, $N_\beta \lambda_\beta$, and the radius of oscillation in the blowout region, r_0.

The insertion of foils F1-F3 affects the measurable quantities in the experiment through its effect on the emittance and the transverse size of the electron beam. By increasing the beam emittance (see Table 2.2), the insertion of a foil results in higher head erosion rate and therefore shorter plasma length. This results in a reduction in the value of all measurable quantities. Note that the increase in emittance here is not sufficient to match the beam to the plasma.

The effect of the increased emittance is compounded by an increase in σ_r, also shown in Table 2.2. The increased σ_r results in lower radial electric field of the beam according to Eq. 2.14, which affects the experiment in three ways.

First, the reduced electric field results in a reduction in the fractional ionization of neutral Rb as the electron beam enters the plasma. The initial rubidium plasma forms farther away from the r=0 axis, and simulations show that this effect results in a delay in the formation of the blowout regime. Similar to the head erosion effect, this hollow plasma formation thus contributes to a reduction in the interaction length.

Second, the increased σ_r and the delay in the generation of the blowout regime mean that the beam slices may not experience the effect of the ramp. Therefore, the peak oscillation amplitude of the beam radii for various beam slices may not reduce below the value of R_b. This results in reduction of participating charge in each slice. The reduced participating charge per slice results in a proportional reduction in the x-ray signal as fewer electrons perform betatron oscillations. In the experiment, we accounted for the reduced participating charge by normalizing the total x-ray signal count by the amount of participating charge in each shot. The participating charge was measured for each data point by measuring the charge outside energies of 19.9 and 21.2 GeV. Additionally, the reduced participating charge per slice in the blowout region can be interpreted as reduced current, and since the head erosion rate depends strongly on the current, the increased σ_r implies a shorter plasma.

Third, the increased σ_r results in an ionization front that is closer to the center of the beam; i.e. closer to z=0 in Fig. 2.3(b). This backward motion of the ionization front results

in further reduction in the interaction length due to having an effectively shorter σ_z for head erosion.

Through the mechanisms described above, the insertion of each foil is expected to strongly reduce the interaction length incrementally from Foil 1-3.

2.6 Evidence for Distributed Injection

The evidence for the distributed injection of electrons throughout the interaction length comes from the examination of the excess charge ΔQ with respect to other parameters that depend on length. The two parameters that depend strongly on length and are therefore used here for its assessment are the x-ray yield and the energy loss. It is important to study the variation of both, because even though both share a dependence on the interaction length, the energy loss is dependent on the longitudinal profile of the beam (Λ, as described above), but the x-ray yield is dependent on the transverse dynamics of the beam. Therefore, a correlation of both energy loss and x-ray yield is an indication of a change in the interaction length, which is the common parameter between the two. The interaction length in this experiment was varied by either changing the beam current as measured by the pyro signal or by changing the beam emittance, which was achieved by inserting one of the foils F1-F3 in the beam path.

The effect of beam current on the experiment can be observed from one data set with 77 shots (Fig. 2.4), where the change in σ_z came about due to random phase variations in the linac. This set of data, was chosen because of relatively wide variation in various quantities, which allows for meaningful correlation of various parameters in the experiment; pyro signal varies from 3500 (representing $\sigma_z \sim 48$ μm) to 5500 (representing $\sigma_z \sim 39$ μm), ΔQ varies from 100 pC to 700 pC, ΔW^- from 3.5 to 5.5 GeV, and x-ray yield varies by nearly a factor of two. Larger σ_z corresponds to lower current, and since the head erosion rate depends on $I^{-3/2}$ [46, 47], the reduced beam current is expected to lead to higher head erosion rate, and decreased interaction length.

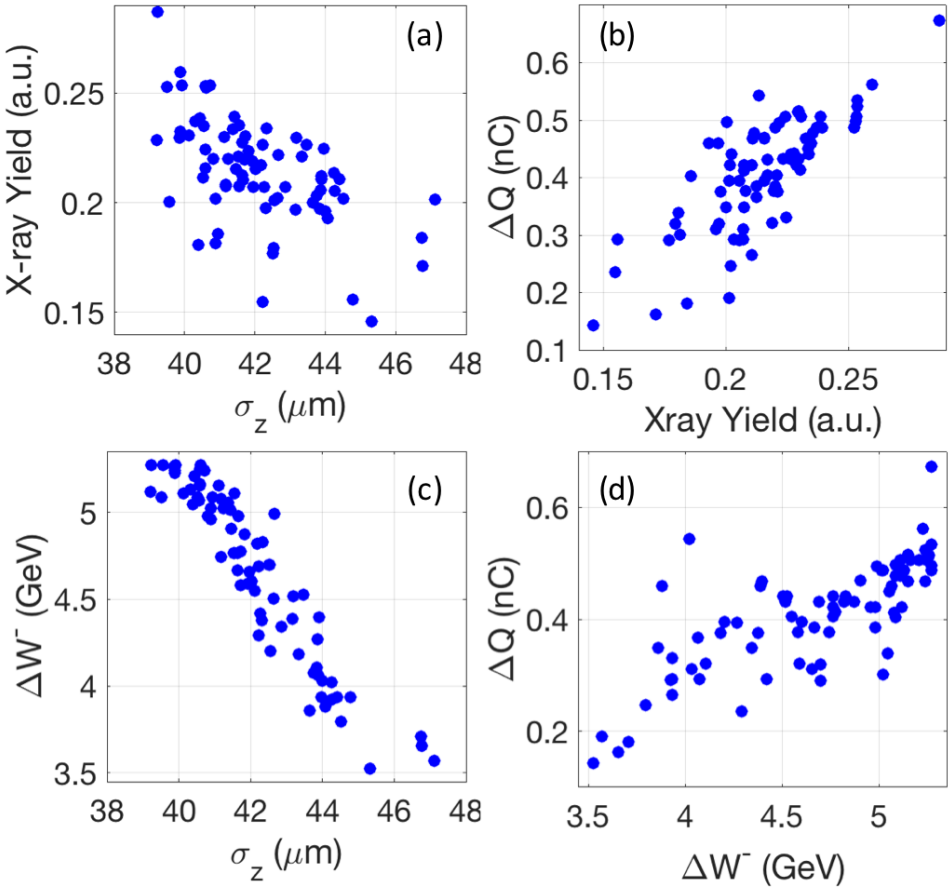

Figure 2.4: (a) X-ray yield for a set of 77 consecutive shots sorted as a function of σ_z. In this dataset, Foil F1 is inserted and the the variation of σ_z is due to the shot-to-shot jitter of the phase of the linac (b) ΔQ and x-ray yield are plotted against each other for each shot. (c) ΔW^- sorted as a function of σ_z for the same data. (d) ΔQ correlation with ΔW^- for the same data.

The x-ray-yield in this dataset, i.e. integrated x-ray signal per electron, increases by a factor 1.9 for increasing values of current (lower σ_z) as shown in Fig. 2.4(a). Other parameters besides interaction length responsible for this variation (see Eq. 2.19) include plasma density, which is constant for this data, γ_b , and the transverse oscillation radius, r_0. The variation in γ_b is on the order of the 10% (29000-33000), which implies a corresponding change in x-rays on the order of 30%. Assuming relatively small changes in transverse radius, the reduction in interaction length, i.e. $N_\beta \lambda_\beta$, accounts for the rest of the difference in x-ray yield. In other words, the length of the interaction was reduced by up to 63%.

The correlation between ΔQ and the x-ray yield (Fig. 2.4(b)) is nearly linear, which suggests that x-rays and ΔQ electrons are generated in proportion as expected based on the physical picture described above, i.e. both are associated with the spot size oscillation during betatron cycles of the beam in the ion column and therefore their yield increases as the plasma length increases. It is also important to emphasize here that the oscillations of the different longitudinal slices of the beam are not in phase, as will be shown in the simulation section. This means that x-rays and ΔQ do not increase with length in discrete steps of λ_β and therefore the relationship between the two shows a continuous curve.

A second correlation between the beam current and the maximum energy loss of the beam electrons ΔW^- (Fig. 2.4(c)) further implies that the reduction of interaction length (and therefore ΔW^-) is due to the reduction of beam current for the data shown in Fig. 2.4. As previously mentioned, ΔW^- depends on the decelerating field E^- and the interaction length and is independent of the transverse dynamics of the beam which determines both the x-ray yield and ΔQ. Therefore, the linear correlation between ΔQ and ΔW^- (Fig. 2.4(d)) is important as it underscores the fact that the change in ΔQ, ΔW^- and x-ray yield are all caused by variations in interaction length and further strengthens argument for the distributed injection of electrons.

The second way to reduce the propagation length is by increasing the beam emittance by inserting one of foils (F1-F3) in the beam path as discussed earlier. Since each foil contributes to progressively larger emittance it is expected that the interaction length decreases with a

higher-numbered foil.

Once again, the reduced interaction length can be inferred by examining the x-ray yield and ΔW^-. By solving the beam envelope equations (Eq. 2.17), one can show that the amplitude of the betatron oscillations would grow by a factor of three as a result of the increased spot size at the entrance of the plasma as shown in [60] and Appendix B. The minima of the oscillation on the other hand, remains nearly the same. In other words, had the beam propagation length remained unchanged, a significant increase (about a factor of 9) in x-ray yield per electron would have been observed due to much larger oscillation amplitude (r_0) as a result of inserting a foil. In the experiment however, insertion of a foil led to a significant decrease in the x-ray yield, as shown in Fig. 2.5(a). The data in this figure is selected such that the beam current is the same for the data points. In this case, the value of pyro chosen implies a beam with $\sigma_z \sim 39$ μm. The similarity in the longitudinal profile of these data points is confirmed by inspecting the beam energy spectrum, which is shown in Fig. 2.5(c).

In addition to x-ray yield, ΔQ also decreases significantly for each increasing number of the foil (Fig. 2.5(a)). Once again, this correlation is consistent with a reduced beam propagation distance in the plasma as the beam emittance is increased. To corroborate the dominant role of reduction of the interaction length as the cause of the decrease in both ΔQ and x-ray yield, ΔQ is plotted as a function of ΔW^- for the same data in Fig. 2.5(b) (figure originally appeared in [69]). It is observed that ΔW^-, which depends on E^- and interaction length rather than σ_r and the transverse dynamics of the beam, monotonically increases with higher ΔQ. Once again, this result shows that the longer the interaction length, (i.e. the higher the ΔW^-), the higher the number of excess electrons that are generated and injected into the wake, and so the source of electrons comprising ΔQ is likely distributed over the interaction length. Since the linear relationship between the charge and length is a characteristic of the electrons ionized and trapped from rubidium and not argon (which is localized at the either ends of the Rb column), the source of the increase in the dark current is consistent with being comprised mainly of the Rb II electrons.

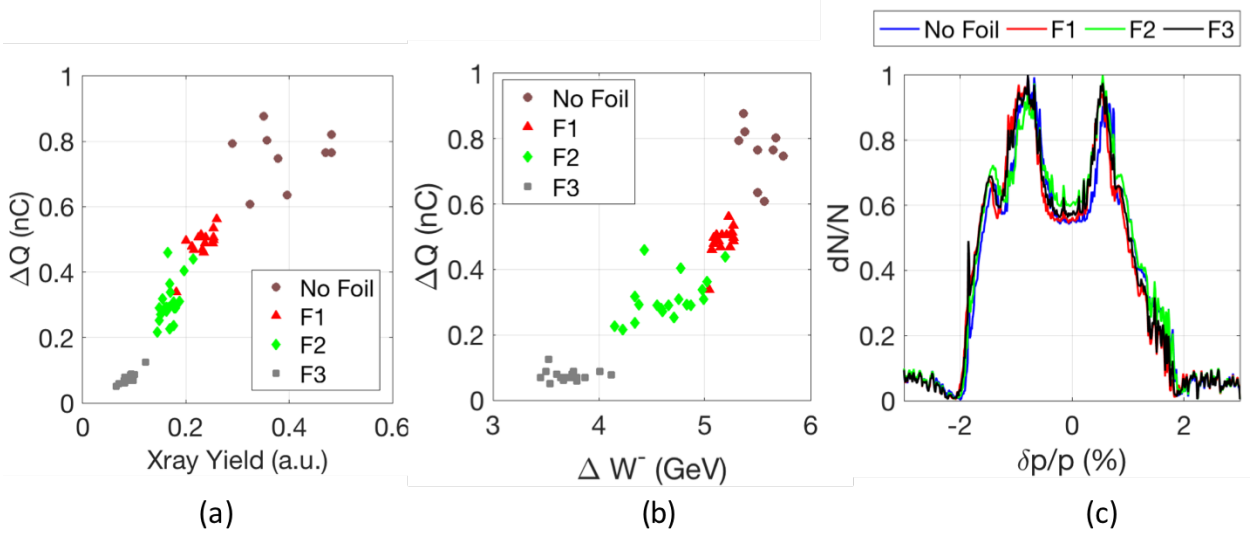

Figure 2.5: (a) Excess charge as a function of the x-ray yield in four cases obtained with the insertion of various foils that change the beam emittance. The data is filtered by selecting pyro values between 5000 and 5300, ($\sigma_z \sim 40$ μm) so that the current profiles are nearly identical as judged by the similarity of the electron beam spectra before the plasma. The data shown in red triangles is a subset of data in Fig. 2.4. (b) Energy loss is shown as a function of excess charge for the same data as in (a). (c) The electron beam energy spectra for the data shown in (a) and (b). The spectra related to each foil is averaged.

2.7 Beam Loading due to Distributed Injection

The Rb II electrons ionized along the length of the interaction can accumulate at the back of the wake, thereby beam loading the wake and reducing the accelerating field. This effect was observed in the experiment as reduced average transformer ratio. The transformer ratio is defined as the ratio of the accelerating field to decelerating field ($R = E^+/E^-$). But since the electric fields were not directly measured in the experiment, the energy loss and energy gain are used instead to define an average transformer ratio $\langle R \rangle = \Delta W^+/\Delta W^-$ in order to examine the effect of distributed injection of Rb II electrons on the fields in the experiment.

To illustrate the beam loading effect of the Rb II electrons, energy loss and gain for another dataset with 71 consecutive shots are examined as shown in Fig. 2.6. This particular data set is of interest because ΔW^- for most of the data is confined to a small range of values between 3.5 and 3.8 GeV (Fig. 2.6(a)). Therefore, the reduction of the average transformer ratio due to the beam loading of the excess charge can be clearly attributed to the beam loading of the accelerating field. It is important to note that as discussed in the previous section, ΔW^- increases with increasing σ_z, as shown in Fig. 2.6(a).

Even though the general trend of the peak energy loss increasing with σ_z is observed in this dataset (Fig. 2.6(a)), there is a large variability in the energy loss in each group. The spread in this dataset is attributed to the effect of the transverse size of the beam on the integrated pyroelectric signal. In general, the correlation of the integrated signal from the pyroelectric detector with σ_z is correct as observed in Fig. 2.6(a). Within a small range of variation of the pyro however, the changes in the transverse size of the beam can affect the signal observed by the detector. To remove this effect from the interpretation of the ΔW^- data, the data points within a small range of pyro (corresponding ± 1.5 μm in σ_z) are grouped together as shown in Fig. 2.6(a).

Removing the spread of the data in the energy loss makes the correlation with ΔQ more observable. This was done in Fig. 2.6(b), where the mean and standard deviation of the ΔQ is plotted for the mean of ΔW^- within each group identified in Fig. 2.6(a). Although the change in the interaction length is expected to be fairly small, even within this small

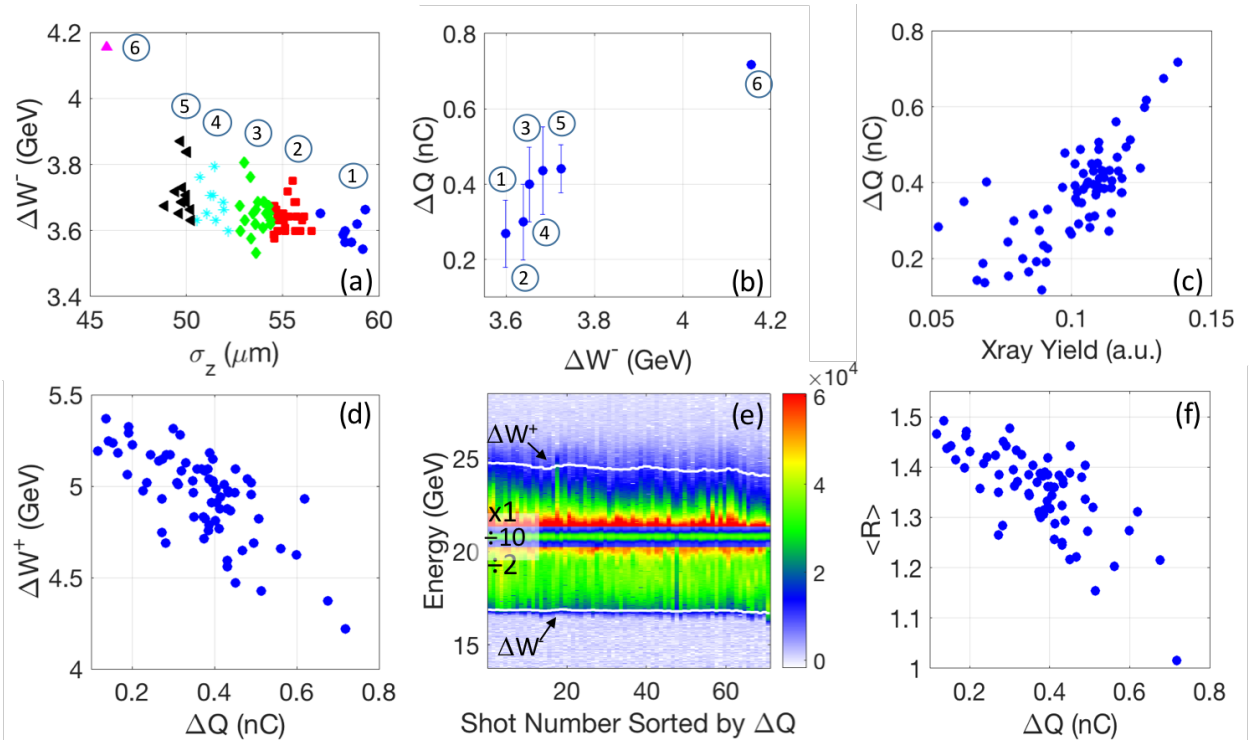

Figure 2.6: Data from a 71 shot dataset where no foils F1-F3 were inserted. (a) Peak energy loss ΔW^- as a function of σ_z, grouped by a range of 300 in pyro corresponding to ~ 3 μm change in σ_z. (b) ΔQ plotted as a function of ΔW^-, where each point corresponds to one of the six groups in (a). The corresponding groups in (a) and (b) are indicted by numbers above or below data points. The value of ΔW^- for each data point in (b) corresponds to the mean value of ΔW^- for a group in (a) and the mean of ΔQ for each group is plotted with the error bars representing the standard deviation of ΔQ in a group. (c) Correlation of X-ray yield and ΔQ data shown in (a). (d) Peak energy-gain ΔW^+ as a function of ΔQ for the same data. 1GeV is added to the raw ΔW^+ value to compensate for the head-to-tail energy chirp of the incoming electron beam. (e) Waterfall plot for data shown in (a). Each slice represents an integration of the spectra along the non-dispersive direction, which are sorted by ΔQ. The shot number is shown on the horizontal axis. The counts near the initial beam energy (~ 20.35 GeV) and the counts below the initial energy (energy loss area) are divided by ten and two, respectively, as indicated on the images. (f) Average transformer ratio, $\langle R \rangle = \Delta W^+ / \Delta W^-$ plotted for the same data set shown in (e).

change, one can observe the correlation of ΔQ with energy loss as evidence of distributed injection, as explained earlier. Note that if the range of pyro is extended by adding data from other datasets such that the overall change in pyro is dominated by beam current and the range of ΔW^- is extended, the same correlation between ΔQ and ΔW^- as described earlier is clearly observed [69].

The relative small change in ΔW^- implies that the peak current and the interaction length are fairly constant. On the other hand, both ΔQ and x-ray yield show several folds of variability and are again strongly correlated (Fig. 2.6(c)), further supporting our model, which asserted that over every cycle of x-ray generation, excess charge is produced, i.e. injection occurs in a distributed fashion. Therefore, in this scenario, we can examine the effect of the accumulated charge on the energy gain directly for a relatively constant length.

As ΔQ increases from 100 pC to over 700 pC, the ΔW^+ decreases by over 1 GeV (Fig. 2.6(d)). Note that this variation is about 5 times higher than the variation in ΔW^-, and that this change is very strongly correlated with the change in excess charge. Using Eq. 2.4 in Section 2.2, one can observe that this ΔQ is enough to reduce the accelerating field by half.

Correspondingly, the value of $\langle R \rangle$ decreases from 1.5 to about 1 (Fig. 2.6(f)). This effect is visually illustrated in Fig. 2.6(e), where data is sorted according to how much ΔQ was generated during each shot. The energy gain can be clearly seen as decreasing while the energy loss stays more or less the same. It is important to note that while this reduction in the average transformer ratio is accompanied by variation in the longitudinal beam size inherent in the shot to shot variations of the LINAC, this effect is not important to calculations of $\langle R \rangle$. As will be seen later in the simulation portion of this paper, the injected electrons accumulate at a certain phase in the wake, where the accelerating field becomes significantly suppressed. The accelerating gradient experienced by electrons behind that phase in the wake will be suppressed due to beam loading and therefore those electrons do not contribute to the 2% of the charge that is used to determine the energy gain.

The effect of beam loading can also be observed when the longitudinal profile is carefully

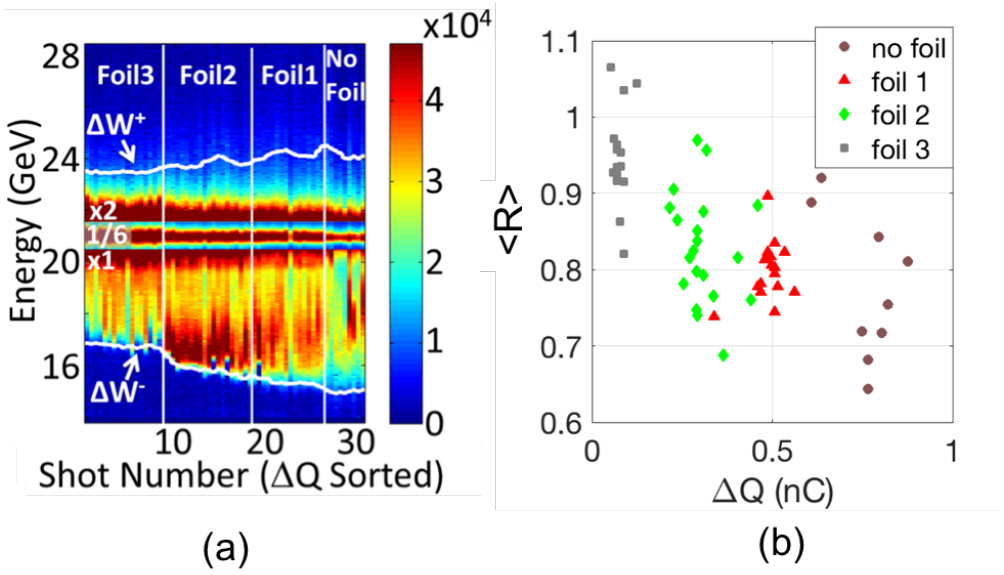

Figure 2.7: (a) Measured energy spectra for the same shots as displayed in Fig. 2.5. The white line shows ΔW^- and ΔW^+, where each point represents moving average of 5 shots. (b) The measured average transformer ratio $\langle R \rangle = \Delta W^+ / \Delta W^-$ as a function of ΔQ

controlled as well. For instance, taking the same profiles used to make Fig. 2.5, it is possible to observe increased beam loading and suppression of transformer ratio in Fig. 2.7 (figure originally appeared in [69]). In this case, the energy loss increased due to the increased interaction length as lower numbered foils are inserted in the beam path as discussed earlier. As the energy loss is increased, the energy-gain increases as well, but it does so at a slower rate because the ΔQ (accumulated up to 1 nC) heavily beam loads the wake. In other words, increasing excess charge (ΔQ) leads to a reduction of the transformer ratio.

2.8 Simulations

2D cylindrical symmetric OSIRIS PIC code [21] was used to simulate the interaction of an electron beam with a rubidium plasma. The simulation confirms the physical picture of beam loading by distributed injection described above. The results show that both argon atoms and rubidium ions are ionized inside the wake as a result of reduction of the beam radius in

a betatron cycle, and as a result both contribute to ΔQ. Additionally, the simulations show that ΔQ causes significant beam loading.

The plasma density is modeled as a trapezoid with a 20 cm plateau region at a density of 2.7×10^{17} cm^{-3} and 10 cm ramps on either side that reduce the density to zero. The simulation box has 480×400 square cells of 0.05 k_p^{-1} wide, where k_p^{-1} is the plasma skin depth. A speed-of-light moving window is used in the direction of beam's propagation. Ionization model used in the simulation was the ADK formalism (Eq. 2.15) and ionization of Rb, Rb^+, Ar, and Ar^+ were included, with 8 particles per cell allocated to Ar and Ar^+ while 4 particles per cell was allocated to Rb and 16 allocated to Rb^+ ions. Rb and Rb^+ ions are treated as separate species, so that the ionization injection and self-injection events can be separated. The electron beam is allocated 4 particles per cell and contains 1.8×10^{10} electrons with $\sigma_z = 35$ μm, $\epsilon_n = 250$ mm-mrad and is focused to a waist of $\sigma_r = 35$ μm.

A snapshot of the simulation, shown in Fig. 2.8, illustrates secondary ionization and injection of Rb II electrons. In this snapshot, the electron beam has already propagated 7 cm into the plasma (i.e. still within the ramp), its transverse radius has already been reduced from the original value of 35 μm, and its envelope is executing betatron oscillations. Several important characteristics of the experiment can be observed from this figure.

First, it can be observed that various longitudinal slices of the beam perform envelope oscillations at different phases with respect to each other. The slices where the envelope radius is at its lowest value (the valley in Fig. 2.3(c)) produce an increased beam electron density (darker red), while those slices with the highest radius (peak of their oscillation) produce lower density (lighter red). The reason for the phase variation in the longitudinal slices is the blowout distance, which is given by $\frac{2}{k_p}\sqrt{\frac{n_p}{n_b}} \sim 2c/\omega_p$ [46]. The electron density continuously decreases down to zero (blowout) over this distance, which means the various longitudinal slices over this distance see different plasma density. Additionally, the longitudinal field structure results in different energies for the various longitudinal slices. Since the transverse dynamics of the beam [37] and particularly the betatron wavelength (Eq. 2.18) depend on density and energy, different slices of the beam will come to perform

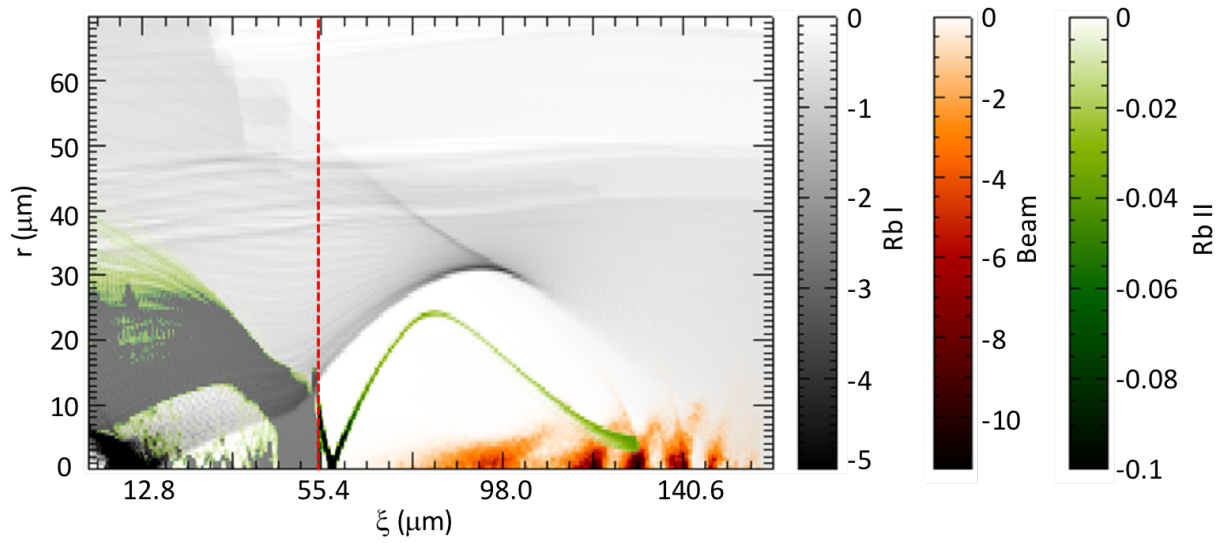

Figure 2.8: A density plot of a snapshot in the simulation. All densities are normalized to 2.7×10^{17} cm^{-3}. Rb II electrons in the area to the left of the red dashed line are made transparent, so that the deflection of the sheath due to the beam loading of excess charge is visible. Since the simulation is cylindrically symmetric, only $r > 0$ is shown in this image. Rb I electrons form the wake and are shown in grayscale while Rb II electrons, shown in green, are tracked separately from Rb I electrons. The color plots are restricted for better visibility of lower density features.

their betatron oscillations at different phases with respect to each other.

Second, Rb II electrons (shown in green color scale) are generated inside the wake at a transverse distance approximately equal to the radius of a beam slice at the pinch point of its oscillation cycle. Rb II electrons ionized earlier in the simulation can be observed moving within the wake (thin green line). Since different slices reach their minimum size at different times, and hence different distances along the interaction length, Rb II injection takes place continuously along the length of the interaction rather than in a periodic manner, which would have been expected if all slices performed their betatron oscillations in phase.

Third, the trajectory of the newly ionized Rb II electrons can be easily inferred from Fig. 2.8. These electrons move to the back of the wake and start accumulating there. The on-axis density of these electrons, which occupy a very small space, reaches as high as 8.1×10^{19} cm^{-3}, 300 times greater than the initial neutral density, which in turn leads to a tremendous transverse space charge field, peaking at over 460 GeV/m. This radial electric field ionized a vertical sheet of Rb II electrons (green), which are then immediately pushed out even through the sheath of the blowout region (grey) that is composed of Rb I electrons. Note that in this simulation, only the first two ionization levels of Rb atoms were included. However, had the higher ionization levels of Rb been included in the simulation, some would likely be ionized as well and likely reduce the value of this field.

Although argon electrons (not shown in Fig. 2.8) are generated in the same way, their effect is localized only to the ramps and therefore, the number of argon electrons trapped is lower than Rb II electrons. In this simulation, the maximum number of trapped argon charge, measured as charge with $\gamma_b > 200$ was 100 pC, reached at 10 cm– or at the top of the ramp. From that point, the number of argon electrons slowly decreased, such that by 15 cm, only 30 pC of these argon electrons remained within the wake. In comparison, Rb II electrons with $\gamma_b > 200$ monotonically increased to 350 pC at 15 cm. In other words, after the ramp, Rb electrons kept being trapped while Ar electrons left the simulation box.

Finally, the beam loading of the wakefield by the injected charge can be observed in Fig. 2.8 in the form of the sheath crossing point being pushed back in the frame of the

beam. This is expected because the longitudinal field of the wake is related to the slope of the sheath [6, 20], and as the injected electrons beam-load the wake, they absorb the electric field of the wake and reduce it. Thus, this beam loading results in a modification of the slope of the sheath, and the significantly reduced slope at the site of the injected electrons can be interpreted as a clear indication of significant beam loading.

The beam loading of the injected charge can be quantified by investigating the longitudinal accelerating field as illustrated in Fig. 2.9. Two simulation times are shown in this figure, one where beam has propagated 12 cm, which is 1 cm after the beam has entered the plateau, and the second, where the beam has traveled 30 cm, 1 cm before the beam enters the down-ramp. To emphasize the effect of beam loading, another simulation was performed, which is identical to the first, except that the secondary ionizations are turned off; in other words, the only ionization state allowed is the ionization of Rb I. The on-axis electric field in the simulation with and without secondary ionization are shown in blue and red, respectively.

Comparing the two simulations at 12 cm, it can be observed that the accumulated Ar and Rb II electrons have already reduced the peak electric field from about 82 GV/m in the unloaded case to about 46 GeV; a drop of nearly a factor of two. At this point, with peak decelerating field being 32 GV/m, the transformer ratio at this point is reduced from ~ 2.7 in the unloaded case to 1.6 in the beam loaded case.

Between 12 cm and 30 cm, the beam loading region widens as more charge is added. It can be observed that after 30 cm of propagation, the accelerating field is reduced almost to zero, where it would have been at its maximum in the unloaded (red lineout) case. As a result of this beam loading, the sheath crossing is pushed backwards resulting in the spike of the accelerating field to be moved from the original $\xi = 58$ μm to $\xi = 45$ μm (Fig. 2.9(b)). It is also noteworthy that the decelerating part of the wakes are nearly identical with and without secondary ionizations as expected because of causality.

Additionally, there is no excess charge observed in the simulation without secondary ionization. This can be explained by inspecting the values of $\bar{\Psi}$, which are shown for the

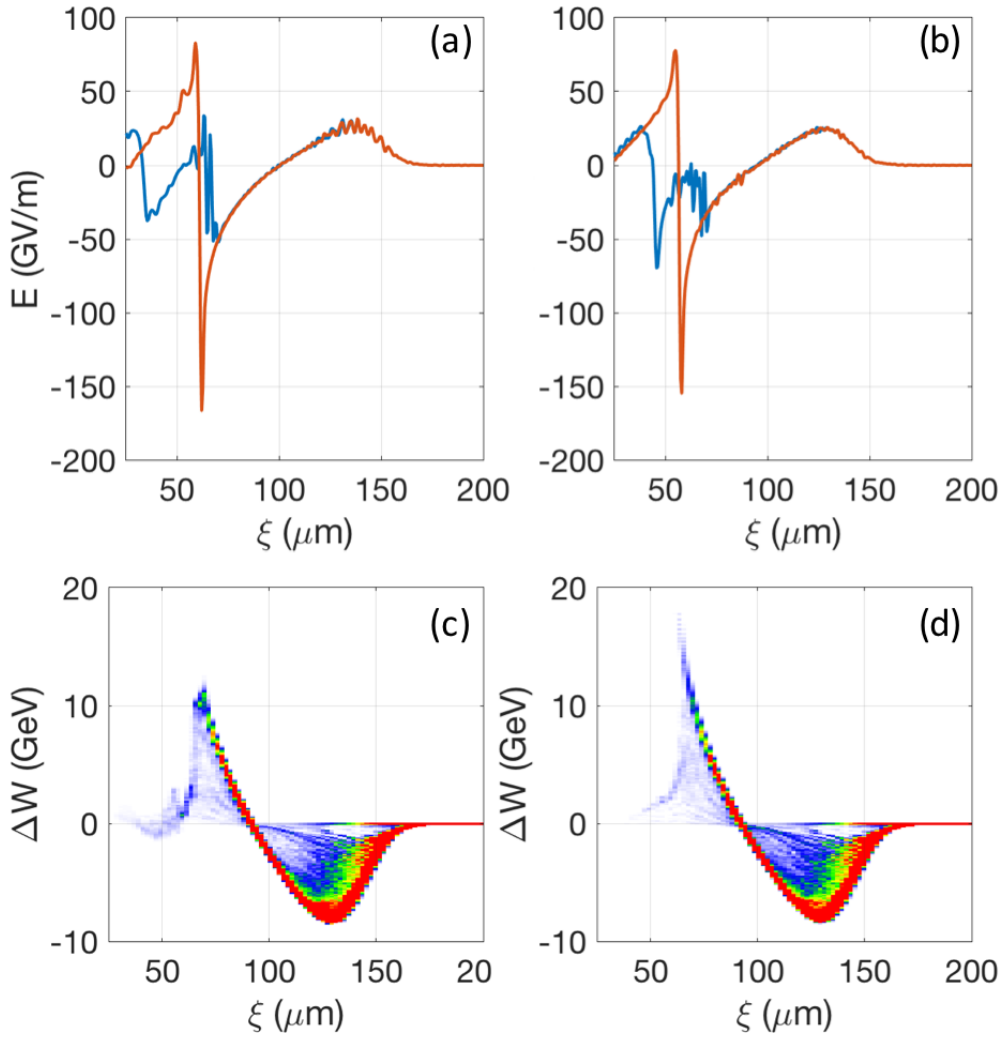

Figure 2.9: Comparison of simulations with and without Ar and secondary Rb ionization. (a) On axis electric field for the two simulations with the beam having propagated 12 cm in the plasma in each simulation. The red curve represents the value of the field where only ionization of Rb I is present. For the blue curve both ionization levels of Ar and Rb are included. (b) Same parameters plotted as (a), except that the frame represents a time at 30 cm of beam propagation. (c) The energy space of the beam at the end of the simulation for the beam loaded case. Peak energy loss of 8 GeV and energy gain of 12 are clearly observed. (d) is the same for the simulation without beam loading – i.e. secondary ionization injection.

same condition as Fig. 2.9(a) in Fig. 2.10. In Fig. 2.10(a) the $\bar{\Psi}$ function is shown as a color map and the outline of the wake's sheath is overlaid on the color map as black line. The location of the sheath is important because the focusing force of the ion column exists only in the region bounded by it. In particular, it is important for the trapping condition to be satisfied before the high density spike at the back of the wake, which is ~ 70 μm on axis (see Fig. 2.10(b)). This is because The high density spike at the back of the wake has a very high transverse field, and if the electrons are trapped before they reach this spike, they would get ejected transversely out of the wake region at this location..

As discussed in the Section 2.3, an electron that will have $\Delta\bar{\Psi} < -1$ can get trapped in the wake. Since the value of the $\bar{\Psi}_f$ at the back of the wake (just ahead of the density spike) is ~ -0.3 (see Fig. 2.10b), the electrons born outside the wake will have a maximum $\Delta\bar{\Psi}$ of -0.3. This value of $\Delta\bar{\Psi}$ is too low to allow for trapping and therefore background plasma electrons are not trapped by the wake. The electrons born inside the wake on the other hand, can have a $\bar{\Psi}_i$ of up to 1.9 depending on where they are born. Because $\bar{\Psi}_f \sim -0.3$, those electrons with $\bar{\Psi}_i > 0.7$ will be able to satisfy the trapping condition $\Delta\Psi < -1$. This region of $\bar{\Psi}_i > 0.7$ is indicated in Fig. 2.10(b). Therefore, the Rb I electrons that are ionized early by the beam do not get trapped in the simulation, and the excess charge is present only due to the ionization injection of electrons from Ar and Rb^1+ ions.

The final energy space of the beam in loaded and unloaded simulations (Fig. 2.9(c) and 2.9(d)) shows how the energy gain and loss are affected by beam loading. This figure is important because energy gain (ΔW^+) and energy loss (ΔW^-) have observable counterparts in the experiment. In the simulation without beam loading (Fig. 2.9(d)), the average transformer ratio $\langle R \rangle = \Delta W^+/\Delta W^- = 17.5/8 = 2.2$, whereas in the beam loaded case, $\langle R \rangle = 12/8 = 1.5$. In the experiment, the $\langle R \rangle$ varies from 1.5 to 0.75 depending on the excess charge (see Fig. 2.6 and Fig. 2.7). The smaller $\langle R \rangle$ *is to be expected* because in the experiment, the tail electrons in the drive bunch apparently do not sample the maximum electric field of the wake.

We note that although nearly 0.8 nC of RbII electrons were injected in the simulation,

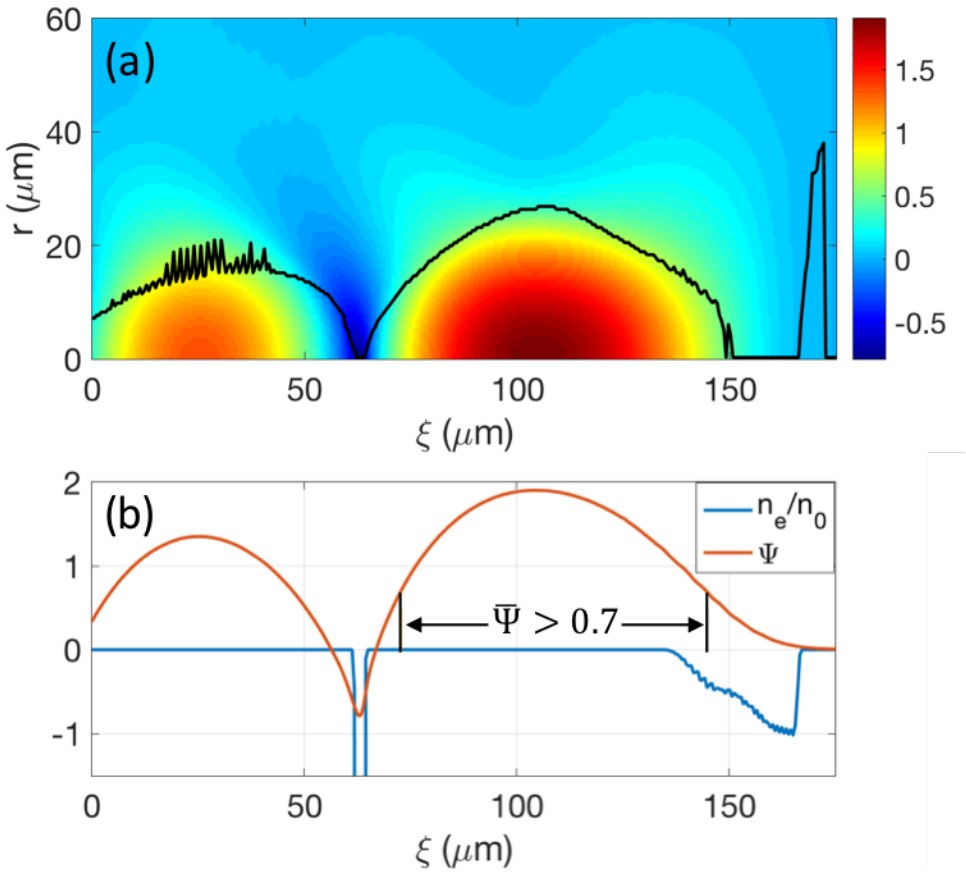

Figure 2.10: (a)$\bar{\Psi}$ for the simulation frame shown in Fig. 2.9(a) for the case where no secondary ionization is present. Black curve shows the outline of radial location, where Rb I electron density corresponds to 50% neutral density, i.e. the bubble sheath for $\xi < 160$ μm. The spike in the region $165 < \xi < 170$ μm indicate the region over which the neutral Rb is ionized. (b) The outline of on-axis plasma density (blue) and $\bar{\Psi}$ (shown in orange) corresponding to the $r = 0$ line in (a). On axis density reaches 1 (indicating full ionization on axis) at $\xi = 165\mu$m. In the region 73.0 μm $< \xi <$ 144.8 μm, $\bar{\Psi} > 0.7$. Electrons born in this region that reach the back of the wake where $\bar{\Psi} \sim -0.3$ satisfy the trapping condition $\Delta\bar{\Psi} < -1$.

i.e. with $\gamma_b > 200$, not all these electrons are necessarily being accelerated at the location of the initial accelerating spike and thus do not contribute to beam loading at that location. Of the total ΔQ of up to 1 nC, only about 300 pC of Rb II electrons are injected and accelerated at the site of the initial spike and the rest of the secondary injection occurred at the second spike, which was generated due to the elongation of the back of the wake. Only the former contribute to the beam loading and the reduction of R. This latter amount is consistent with the estimate of the charge that would reduce the accelerating field by half from the "Beam Loading and Transformer Ratio" section. It is further interesting to note that the excess Rb II charge gained over 10 GeV in energy (peak energy of about 10.7 GeV was observed in this simulation) and in principle could be observed in the experiment.

2.9 Conclusions

In summary, an electron beam produced Rb plasma was investigated as a source for plasma wakefield acceleration. This source was explored for mitigating the problems of head erosion and ion motion. However, if the experiment is operated in the blowout regime at a high plasma density such that the drive beam can strongly pinch down and ionize the Rb further, Rb II electrons can be injected into the wake and act as dark current. Beam loading by accumulation of the Rb II electrons can severely reduce the accelerating field and thereby reduce the average transformer ratio in such a plasma. The PIC simulations have confirmed the physical picture emerging from the experimental results. Simulation values for the transformer ratio, and the excess charge are consistent with that seen in the experiment.

The work at UCLA was supported by NSF grant PHY-1415386 and DOE grant DE-SC0010064. The simulations were carried out on the Hoffman cluster at UCLA. Work at SLAC was supported by Department of Energy contract DE-AC02-76SF00515.

CHAPTER 3

Generation of Low Emittance Electron Beams

3.1 Introduction

The work described in this thesis was part of a larger effort to show that a single stage plasma wakefield accelerator can not only provide a high accelerating gradient, but also that the energy stored in the plasma wakefield structure can be extracted with a high efficiency. The next major challenge for a plasma wakefield accelerator is to demonstrate the possibility of accelerating low emittance electron beams. This is important, because both collider and light source applications require extremely low emittance electron beams.

Generating low emittance beams from a plasma wakefield accelerator is an active area of research. Recently, several simulation papers have reported on the possibility of obtaining low-emittance electron beams using ionization injection [14, 70, 12]. The process of ionization injection was fully described in Section 2.3. The sources in the literature have discussed using ionization injection within the wake via the combined action of the electric field of the driver and the wake [41, 48, 71, 42] or by using the electric field of additional sources such as one or more trigger laser pulses [14, 70, 12].

In this attempt to characterize the electron generated via ionization injection, we have performed experiments to investigate the characteristics of injected electron beams that can be generated without using an external trigger such as a laser pulse. In particular, we explored the use of a relatively high emittance drive bunch to produce a wake that can accelerate a lower emittance bunch to energies comparable to the drive bunch energy. In this chapter, we report our initial findings where we employ the ionization-injection technique to inject the electrons in the wake, which are accelerated at high gradients. This self-generated,

secondary bunch contains tens of pC of charge and energies up to 30 GeV. Furthermore, emittance measurements of the injected beam imply an emittance value that is many times smaller than the initial emittance of the drive beam.

We therefore investigated the possibility of using the plasma wakefield acceleration (PWFA) scheme to produce such low emittance beams. In particular, we will show that the injected beam can be identified using an electron energy spectrometer and that the energy spectra can be used to determine the charge, energy spread, and emittance of these beams. Additionally, we establish the scaling of the energy gain with length from 10 GeV to over 30 GeV by using a 30 cm and a 130 cm-long plasma source. The injected beams achieve energies that are up to 50% greater than the initial drive electron beam while maintaining a normalized emittance 30 mm- mrad, which is less than one tenth of the initial drive beam's emittance.

3.2 Experimental Setup

The experiments described here were performed at the FACET facility at the SLAC National Accelerator Laboratory using the single compressed bunch configuration similar to Chapter 2. The FACET drive beam had 2×10^{10} electrons (3.2 nC) with 1.4% rms energy spread.

Both self-ionized and pre-ionized plasma generation were used during the experiment. The plasma source was a lithium vapor, which is described in Appendix A. The ionization occurred either via the transverse electric field of the beam itself or by an auxiliary laser pulse. The resulting lithium vapor was contained by helium gas, which is in pressure balance with the lithium vapor as expected at thermodynamic equilibrium. The presence of helium as the buffer gas led to the creation of lithium density ramps. Where the density and pressure of lithium vapor falls, residual helium atoms maintain the pressure balance. The resulting number density of the neutral lithium and helium atoms is shown as an inset in Fig. 3.1. Two different configurations were used in this experiment: one was a 30 cm long column of 2.5×10^{17} cm^{-3} lithium vapor density and the other was a 130 cm column of 8×10^{16} cm^{-3} lithium vapor density. The primary diagnostic used to observe the injected helium charge

was an imaging electron energy spectrometer [72], as illustrated in Fig. 3.1. Toroidal charge monitors were used to observe excess charge generated during the plasma interaction [69], which is calculated as the difference between the upstream and downstream toroids.

3.3 Observation of Injected Electrons

The first evidence for the injected charge comes from the difference in charge registered by the downstream and upstream toroids. This excess charge was first seen by E. Oz et al. [41] and subsequently analyzed by N. Kirby et al. [42] and N. Vafaei-Najafabadi et al. [69]. Although much of this charge comprises sub 100 MeV electrons from trapping occurring in the exit downramp, tens of pC charge with multi GeV energies was previously observed [42]. It was soon realized through theoretical analysis and computer simulations, that far from being a source of dark current that would drain the energy stored in the wake, the ionization-injected charge could be a source of very low emittance electron beams. In this work we report our progress towards generating such beams.

In these experiments as in the previous work, when the plasma was formed via beam ionization (without the presence of an ionizing laser), the electron spectra resulting from the interaction of the drive beam and the 30 cm plasma showed two distinct groups of electrons (see Fig. 3.2 for several examples). The first group of electrons, which belonged to the drive beam, can be observed on the spectra with energies spanning from 10 GeV to over 20 GeV. The second group, typically narrower than the first, is comprised of electrons between 6-10 GeV, which is completely disconnected from the first group in frames (a)-(c). This disconnect strongly suggests that the two groups had different origins and that the second group was produced in the course of the interaction of the drive beam with the plasma, meaning that this is the accelerated injected charge. The charge contained in the injected beamlets was between 10-20 pC. This charge estimate is based on the pixel counts on the spectrum, which is calibrated against the number of electrons in the drive beam in the case of no plasma interaction. The estimates for the beamlet charges are made for the cases where the charge of the injected electrons is clearly separate from those of the drive beam electrons. The

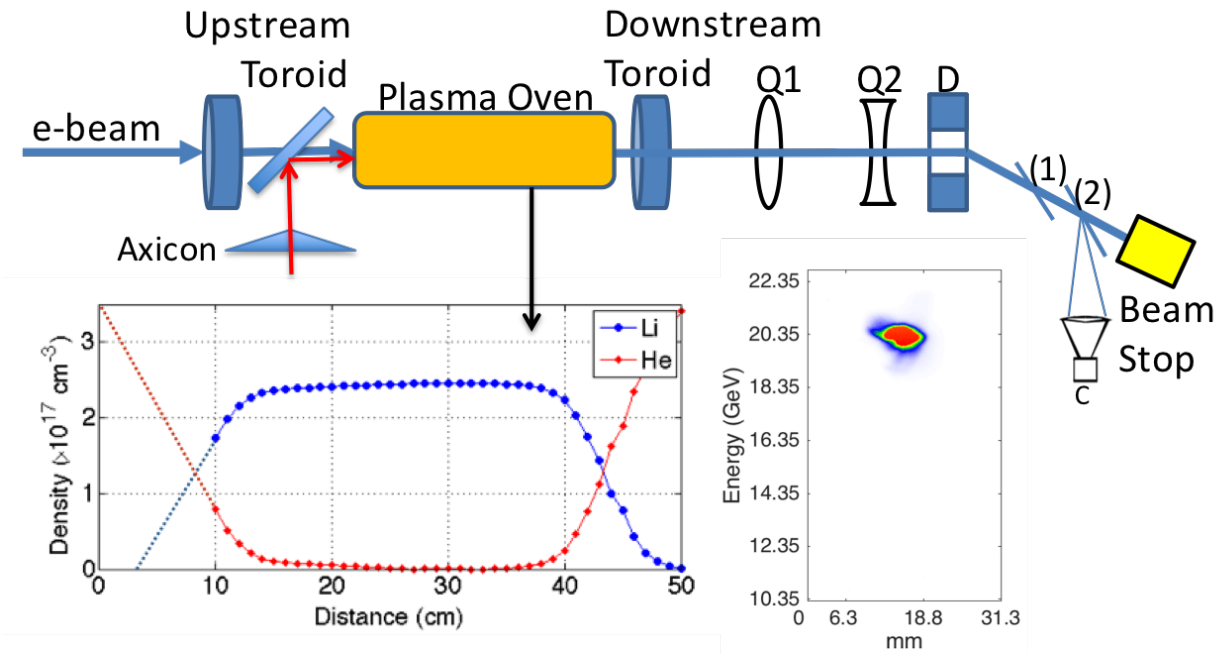

Figure 3.1: Experimental setup. Toroidal charge monitors upstream and downstream of the plasma monitor the input and output charge. The inset shows the neutral density profile of lithium and helium in a nominally 30 cm long oven. The spectrometer is formed by the dispersive element (D) and a pair of quadrupoles (Q1, and Q2) used to focus particular energies. Cherenkov radiation is produced by the dispersed electrons in the 5 cm air space between two Si wafers marked (1) and (2) and is recorded by the camera C. An example of the drive beam spectrum before plasma interaction is shown as an inset. The electrons are dumped into the beam stop. An axicon optic was used to preionize the plasma (see Section 3.5).

peak energy of the injected charge ranged from 6-10 GeV, which implies a peak acceleration gradient of over 30 GV/m. The energy spread of the injected charge was several GeV, with the lowest observed value being 1.2 GeV FWHM for the case in Fig. 3.2(b), or about 20%. The divergence angle of the narrow injected beamlets was deduced by comparing the width of two features in the non-dispersive (horizontal) plane at energies different from the energy focused by the spectrometer. For data in Fig. 3.2, quadrupoles of the imaging spectrometer were set such that the electrons at 6.35 GeV were imaged. As both injected charge and the beam electrons can be observed at energies near 9 GeV in Fig. 3.2(d), this image is particularly well suited for comparing the divergence of the two beams. The rms width of a slice of the injected charge at 8.4 GeV is 0.6 mm as compared to 2.8 mm for a slice of the drive beam at 9.4 GeV. The expected location of an electron can be calculated using transport matrix elements,

$$\begin{bmatrix} x_1 \\ x_1' \end{bmatrix} = \begin{bmatrix} R_{11} & R_{12} \\ R_{21} & R_{22} \end{bmatrix} \begin{bmatrix} x_0 \\ x_0' \end{bmatrix} \tag{3.1}$$

where x_1 and x_1' are the transverse location and angle at the Cherenkov screen, x_0 and x_0' are the transverse location and angle at the exit of the plasma,and R_{mn} are the elements of the transport matrix, which are determined by our spectrometer configuration.

In our system, $|R_{11}| < 2.5$, and $R_{12} = 10.9$ and 13.1 for the 8.4 GeV (corresponding to injected-beam slice) and 9.4 GeV (corresponding to drive beam slice), respectively. Since the maximum value of x_0 is the radius of the blowout regime ($R_b \sim 26\mu m$ as will be shown in Table 3.1), the value of $R_{11}x_0 \sim 70\mu m$ and therefore is negligible compared to the size of the above slices. This means that the difference in the size of the two beam slices is primarily due to divergence. Using the values of the beam rms and R_{12}, it is observed that the divergence of the drive beam is 3.8 times higher than the injected charge. For lineouts at other energies, this value remains between three and four. In the case of similar sizes for the drive beam and the injected beam at the exit of the plasma therefore, it can be concluded that the emittance of the injected charge is at least three to four times smaller than that of the drive beam. A more direct calculation of emittance using a high-resolution fluorescent screen is described in Section 3.6. Fig. 3.2(d) also shows the difficulty of estimating the charge and

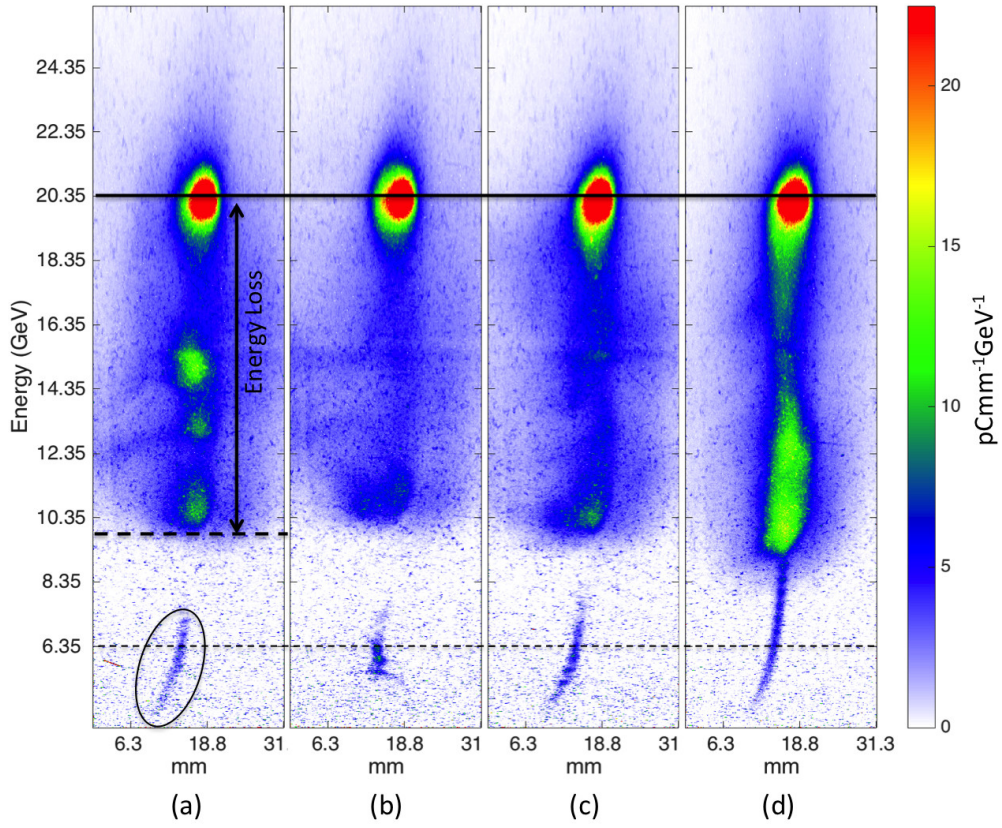

Figure 3.2: Energy spectra resulting from the interaction of the drive beam and the 30 cm plasma. The spectra are from nominally identical conditions with the variation occurring because of shot- to-shot jitter in the linac. The solid black line indicates the initial drive beam energy at 20.35 GeV. The energy spread on the drive beam was 1.4% rms (see inset in Fig. 3.1 for example spectrum). Electrons with energy of 6.35 GeV are focused by the spectrometer's quadrupole magnets, and marked by thin dashed black line. The injected charge in (a) is identified with an ellipse and the peak energy loss is indicated by a thick dashed black arrow. (b) The energy distribution of injected charge peaks at 5.8 GeV and has an energy spread of 1.2 GeV FWHM (20%). (d) Energy gain can reach over 10 GeV, in which case the maximum energy of the injected charge is difficult to discern as it merges into and overlaps with the energy loss feature of the drive beam. The tilt angle observed in the injected beam is due to slight misalignment in the trajectory of of the beam with respect to the center of quadrupoles (Q1 and Q2 in Fig. 3.1).

energy spread in the cases where beamlets obtain higher energies. When the trapped beam and the drive beam electron signatures merge on the spectrometer, the charge and energy spread are difficult to estimate. It can be reasonably assumed that when the drive beam electrons experience a higher energy loss, there is a higher amount of charge that can be trapped because the larger fields accommodate more electrons before they are beam-loaded [20]. Therefore, the 10-20 pC represents a lower estimate of the injected charge.

3.4 Helium as Source of Injected Charge (Simulation)

The ionization of the first helium electron is identified as the source of the injected beamlet in a 2D cylindrically symmetric, particle-in- cell (PIC) OSIRIS simulation of the experiment [21]. An electron beam with 1.8×10^{10} electrons is initialized with a bi-Gaussian profile and $\sigma_r = \sigma_z = 30\mu m$. The moving window has a grid of 720x400 square cells, with the size of the cells being 0.05 k_p^{-1}, and all parameters normalized to $n_0 = 2.5 \times 10^{17}$ cm^{-3}. The ionization of the first electrons of helium and lithium are included in the code using the ADK tunnel ionization model, and each species has 16 particles per cells. The other ionization levels are ignored as the fields in the blowout region are not strong enough to ionize them. Ionization fraction (n_e/n_0) is calculated by [66] using

$$W(s^{-1}) \approx 1.52 \times 10^{15} \frac{4^{n^*}\xi(\text{eV})}{n^*\Gamma(2n^*)} \left(20.5\frac{\xi^{3/2}(\text{eV})}{E(\text{GV/m})}\right)^{(2n^*-1)} \exp\left(-6.38\frac{\xi^{3/2}(\text{eV})}{E(\text{GV/m}}\right), \quad (3.2)$$

$$\frac{n_e}{n_0} = 1 - \exp\left(-\int W dt\right). \quad (3.3)$$

Here, E is the electric field in GV/m, ξ is the ionization potential in eV, Γ is the mathematical gamma function, n^* is the effective principal quantum number and is equal to $n^* \approx 3.69Z/\xi^{1/2}$ (eV), where Z=1 is the charge state of the ion. The density profiles of lithium and helium used in the simulation are similar to those shown in Fig. 3.1. The lithium density is modeled as a trapezoid with 10.4 cm long density ramps on either side of a 31.2 cm density plateau at to $n_0 = 2.5 \times 10^{17}$ cm^{-3}, and helium density is modeled as an inverted trapezoid, such that its density ramps down to zero at a point where the lithium

plateau begins.

Ionization of helium on the lithium density ramp occurs primarily due to the transverse electric field of the electron drive beam. The transverse spot size of the mismatched electron beam oscillates as the electron beam undergoes betatron oscillation [37, 67]. Once the transverse size of the beam gets sufficiently small, it will lead to ionization of helium. The threshold transverse size that leads to appreciable ionization of helium can be calculated using the ADK tunneling model (Eq. 3.2). The calculations show that a Gaussian electric field profile with $\sigma_z = 30\mu m$ will need a peak field of 62.5 GV/m to ionize 10% of helium atoms. Given the equation of the transverse field of an electron beam, $E_r^{max} = 17.3[\text{GV/m}](N/10^{10})(10\mu m/\sigma_r)(30\mu m/\sigma_z)$, where $N = 1.5 \times 10^{10}$ is the observed number of electrons participating in producing the wake in the simulation, the 10% ionization of helium requires a $\sigma_r^{th} = 4.1\mu m$. During the propagation of the electron beam in the density ramp, the transverse size of various beam slices decreases to below this value, leading to ionization of helium. In Fig. 3.3(a) for instance, generation of helium electrons is clearly observed near the slice with $\sigma_r \sim 2\mu m$, generating over 100 GV/m of electric field, which easily ionizes helium. Although many of these electrons are left behind by the wake, some of these electrons are "trapped" and form a stable beamlet that is accelerated by the wake. This beamlet of electrons is shown to persist after 31.2 cm of propagation in Fig. 3.3(b), with 20.8 cm of propagation occurring in the plateau region. The energy spectra of this beam after 31.2 cm propagation is shown in Fig. 3.3(c), and it has several features that corroborate those of the beamlets observed in the experiment such as a wide energy spread and a peak energy of nearly 10 GeV. It is also interesting to note that a small number of electrons in the simulation gain as much as 20 GeV of energy. The on-axis electric field and density of the trapped charge are shown in Fig. 3.3(d). The field can be observed to be heavily beam loaded, with the peak loaded gradient of the wake around a normalized value of -1 or 36 GV/m, which is half the value of the useful accelerating field, defined by linearly extending the field to the back of the wake (dashed black lines in Fig. 3.3(d)).

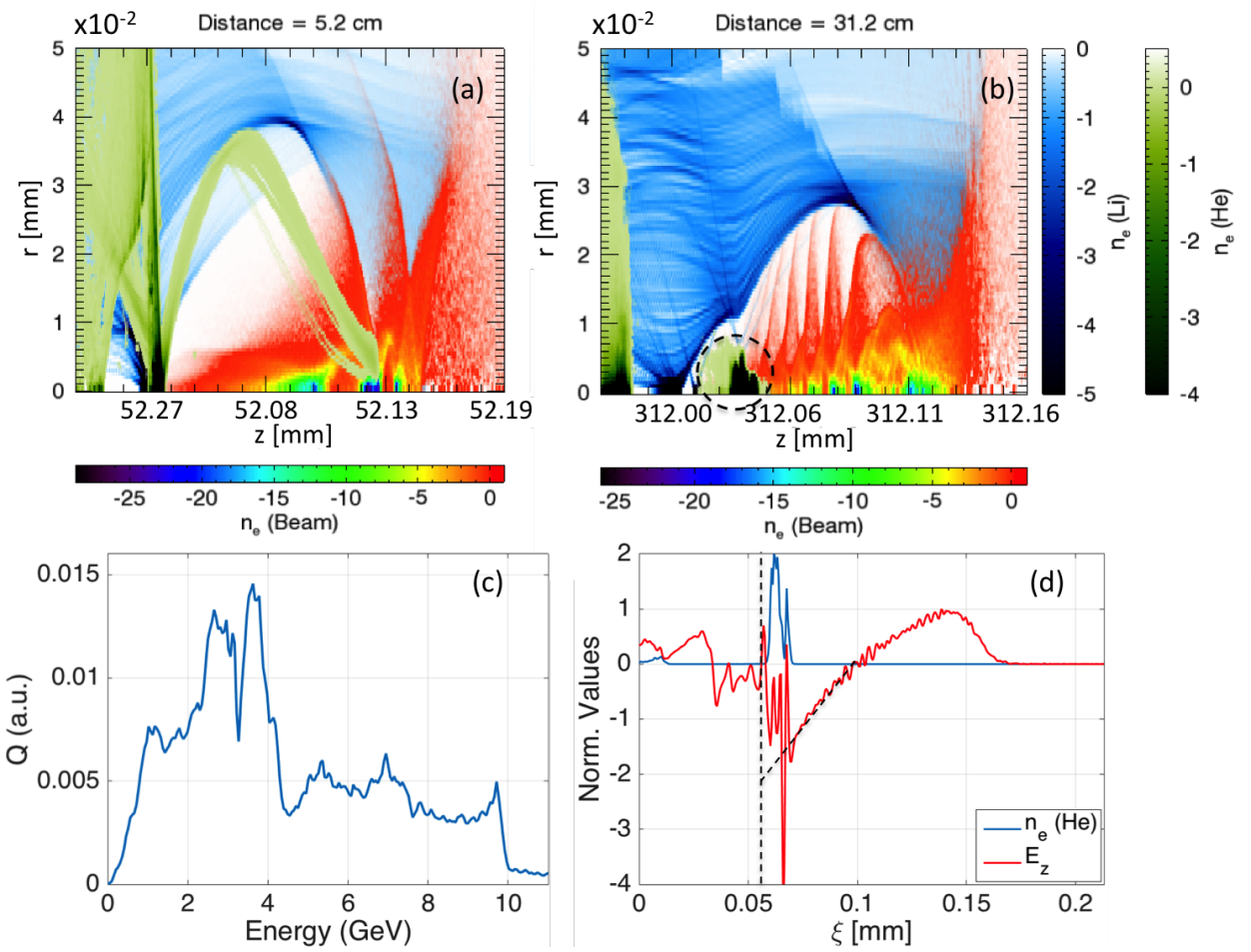

Figure 3.3: OSIRIS simulation results. (a) shows an r-z slice of the cylindrically symmetric simulation, where the e-beam has propagated 5.2 cm (halfway up the ramp). The color table for the drive beam electrons is shown below the figure. Lithium and helium electron densities are shown in blue and green, respectively. The process of helium electron injection can be observed. (b) r-z slice of simulation after the e-beam propagates 31.2 cm (20.8 cm in the plateau region). Color map for the beam electrons is displayed below the image. Lithium and helium electrons are shown with same color maps as (a). The helium electrons at the back of the wake are encircled with a dashed black circle. (c) Energy spread of the helium electrons after the e-beam propagates 31.2 cm. (d) The on-axis longitudinal electric field (red) normalized to 36 GV/m and the on-axis density of the helium beam (blue) normalized to 6×10^{19} cm^{-3}. The dashed black line indicates the useful accelerating field without beam loading.

3.5 Helium as Source of Injected Charge (Experiment)

As explained in the Section 2.3, the trapping condition for an electron in PWFA is expressed as $\Psi_f - \Psi_i < -1$ [41, 48], where Ψ is the normalized pseudo potential, and Ψ_i refers to the value of the pseudo potential where the electron is born and Ψ_f is the final value of this potential as an electron slips back in the wake..

If $\Psi_f - \Psi_i < -1$ for these electrons, then they have achieved the wake's velocity and therefore are trapped and this tends to occur near the back of the region of blowout. For a wake in the blowout regime, electrons which are born via laser preionization of both lithium atoms and the buffer helium atoms will have a $\Psi_i = 0$ resulting in $\Psi_f - \Psi_i > -1$ [48] leading to no trapped electrons. For the case of no laser preionization (most of the results in this paper), the lithium atoms are easily ionized by the electron beam itself and are thus necessarily born near the head of the bunch, just prior to their radial blowout. As in the laser trigger case, since they are born before the wake formation, their Ψ_j will also be near zero. However, as the beam within the lithium ion column of the wake executes betatron oscillations, its radial field at a local minimum of its spot size can be sufficient to ionize the (formally neutral) helium atoms within the wake, thus reducing Ψ_j. If the field of the wake is sufficiently high, these helium electrons will become trapped towards the rear of the wake.

Therefore, the origin of the low divergence electron feature seen in Fig. 3.2 as being ionization injection of helium electrons can be experimentally tested using an intense laser pulse to preionize the helium atoms in the density up-ramp of the lithium source before the electron bunch arrives to produce the wake. A 500 mJ, 100 fs laser pulse from the nominally 10 TW FACET Ti:Sapphire laser was focused using an axicon optic with an angle of $\alpha = 1.5$ degrees. The axicon was located 95 cm upstream of the start of the lithium density plateau. The laser intensity distribution after the axicon for a flat-top laser can be calculated as [73]

$$I(r,z) = I_0(2\pi)^2 \frac{z\delta\sin(\delta)}{\lambda\cos^2(\delta)} J_0^2(k\delta r), \tag{3.4}$$

where $k = 2\pi/\lambda$, with λ the laser wavelength, and δ is the angle of approach as calculated from $\sin(\delta+\alpha) = n\sin(\alpha)$, where n is the index of refraction for the axicon. The axicons used

at FACET are made from fused silica, where n = 1.45. The laser pulse has an approximately flat-top profile with a width of 40 mm at the location of the axicon, leading to intensity of $I_0 = 4.0 \times 10^{11}$ Wcm^{-2} on the axicon. According to Eq. 3.4, a flattop laser profile produces a linearly increasing intensity on axis downstream of the axicon as shown in Fig. 3.4(a). Also shown in this figure are the density profiles of the helium and the lithium. Using this intensity distribution and modeling the ionization of helium using the ADK tunnel ionization rate [66], we can calculate the ionization map for the helium atoms in the interaction region using Eq. 3.2. The resulting ionization map (Fig. 3.4(b)) shows that the helium electrons are fully ionized at the location of the helium density ramp. If the helium atoms are ionized before the arrival of the electron beam, they are blown away by the head of the electron beam just like the lithium electrons and therefore no injection into the wake can happen. We would therefore expect the additional beamlets seen in Fig. 3.2 to disappear. Indeed, when laser pulses were sent ahead of the electron beam in this experiment, the trapped charge disappeared in almost every case. An example of such side-by-side comparison using the short plasma can be observed in Fig. 3.5(a) and Fig. 3.5(b), where the difference in the two shots is the presence of the laser. Similarly, the low- divergence, high-energy signal seen with the longer length plasma (see Section 3.6) disappears when the laser pulse is sent ahead of the electron beam as seen in Fig. 3.5(c) and Fig. 3.5(d). In the case of the long plasma, a 0.75-degree axicon was used 120 cm upstream of the lithium plateau with the other laser parameters unchanged. Although similar calculations as presented in Fig. 3.4(b) indicate possible 50% ionization of the helium, the presence of the laser nevertheless removed the injected beam. Furthermore, when the laser energy was reduced to 1/4 its nominal full energy, the injected charge reappeared. In other words, as long as the laser energy was above the threshold of ionization of lithium, but not helium, the injected charge features appeared in the experiment strongly indicating that the injected charge comes from the ionization of the helium atoms by the combined action of the beam and the wakefields within the fully formed wake.

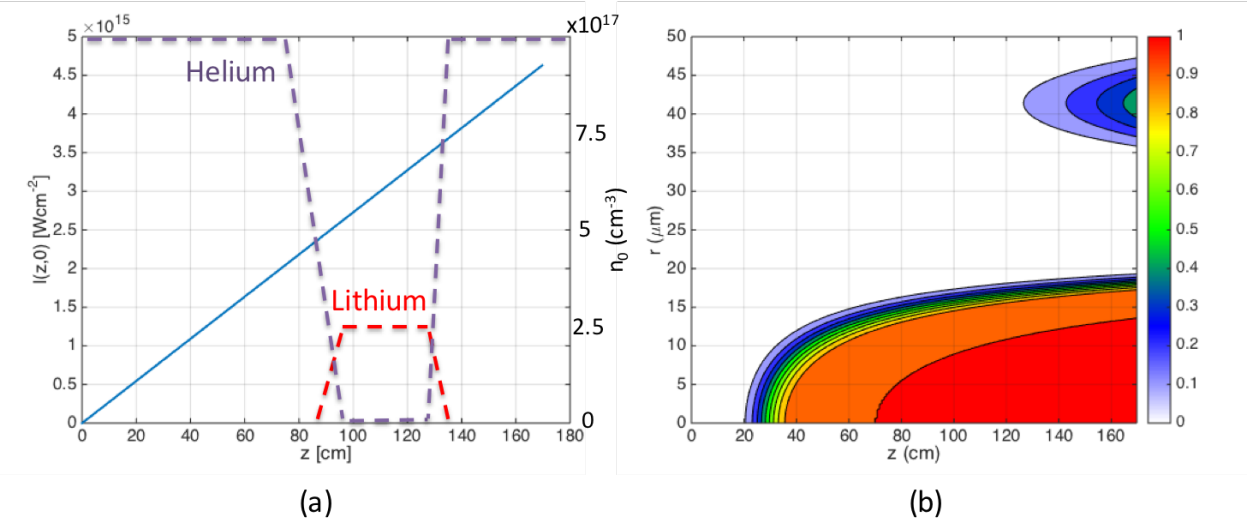

Figure 3.4: Calculation of the region in space where the laser is intense enough to ionize helium atoms. (a) Blue solid line is the intensity profile of a 500 mJ, 100 fs laser pulse with a 40 mm wide flat top profile incident upon a 1.5 degrees axicon. The neutral density profiles of lithium and helium are overlaid on the intensity profile as dashed red and purple lines, respectively. (b) Ionization fraction contour (n_e/n_0) of helium subject to laser intensity in (a) calculated from the integrated ionization rate (Eq. 3.2) over 100 fs.

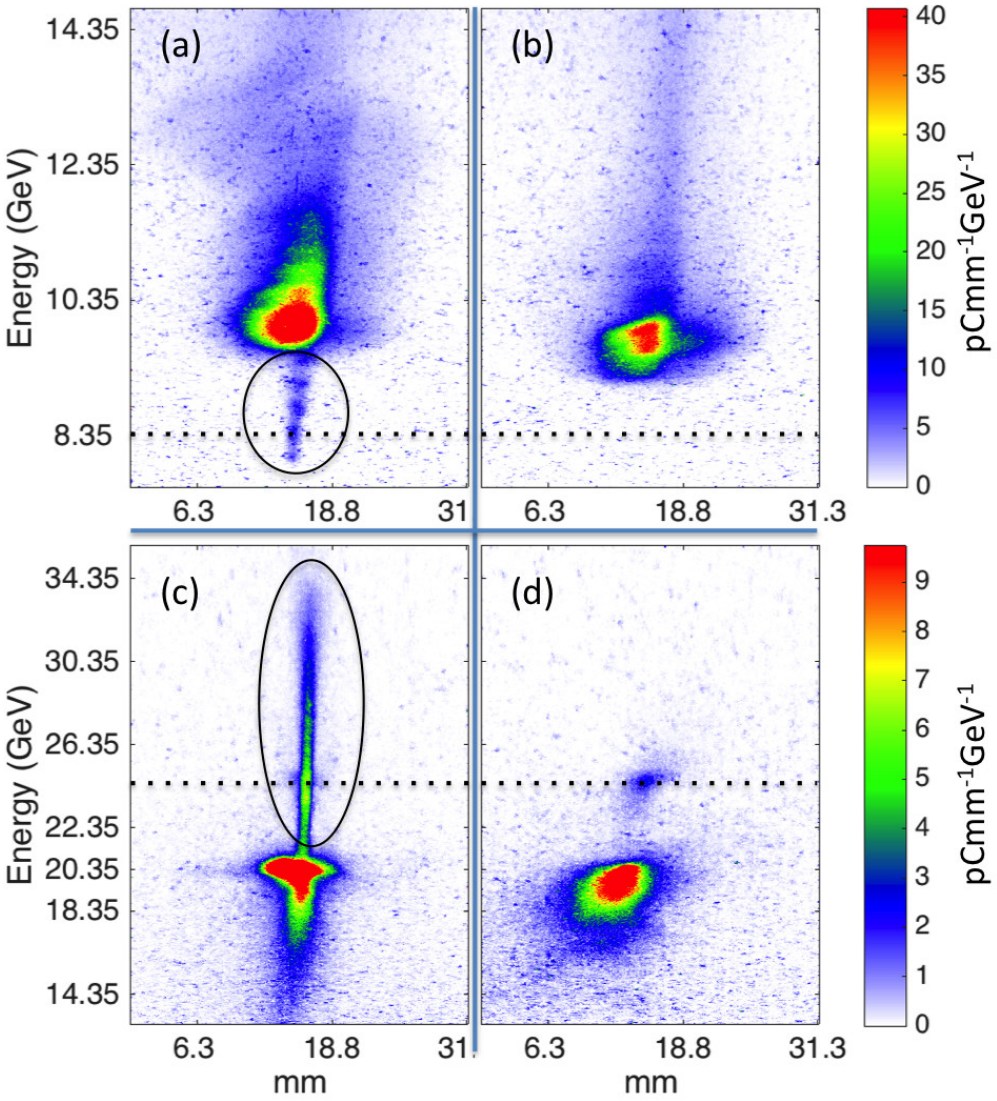

Figure 3.5: Spectra resulting from the interaction of the electron beam with (a) the 30 cm lithium vapor without preionization laser. (b) 30 cm lithium vapor with laser pulse preionizing the plasma. (c) 130 cm lithium vapor without preionization laser. (d) 130 cm lithium vapor with laser pulse preionizing the plasma. The energy focused by the quadrupoles of the spectrometer is marked with a dashed black line. The color table for (a) and (b) is defined by the top color bar and the one for (c) and (d) is defined by the bottom color bar. Injected charge is marked with solid black ellipses.

3.6 Plasma Length Scaling

The injected beamlets were also observed when a second, longer plasma source was used. The plasma density was reduced from 2.5×10^{17} cm^{-3} in the case of short plasma to 8×10^{16} cm^{-3} in the case of the long plasma to increase the plasma wavelength and thus reduce the number of accelerated drive beam electrons. This was done to enhance the visibility of the injected charge on the spectrometer. Because of the high energy of the drive beam ($\gamma \sim 40,000$), each longitudinal slice of the electron beam maintains its relative distance with respect to the other slices during the interaction and does not dephase with respect to the wake. Therefore, with increasing plasma length, we expect an increase in the energy of the injected charge for as long as the beam can drive the wake. The expected scaling of the electron energy can be estimated using the equations for the accelerating fields in the blowout regime [6]. The peak accelerating field is given by $eE_{\max}/(mc\omega_p) = -\frac{1}{2}k_p R_b$, where R_b is the maximum blowout radius and $k_p = \omega_p/c$ is the inverse skin depth of the plasma. In the case of a bi-Gaussian beam, where $k_p\sigma_z \approx 1$ and $k_p\sigma_r \ll 1$, $k_p R_b \approx 2\sqrt{\Lambda}$, where Λ is charge per unit length and can be expressed as $\Lambda = n_b/n_0(k_p\sigma_r)^2$, where n_b is the beam density. Thus in the blowout regime, we can make a rough estimate for the expected energy from the short and the long plasma source as shown in Table 3.1.

In the case of the short plasma, the peak energy gain ($\Delta W_{\max}^{\exp}$) of the helium electrons was observed to be in the 8-10 GeV range. One possible explanation why the observed gain was less than the calculated value of 18 GeV from nonlinear wakefield theory is that the beam loading reduced the wake strength.This effect was observed in the simulation,where the $E_{\max}^{\text{sim}}$ was seen to reduce by 50% due to beam loading to about 36 GV/m (Fig. 3.3(d)). This resulted in an energy gain of 9.7 GeV after 31.2 cm propagation in the plasma, which is similar to observed energy range in the experiment. The peak energy gain and the peak field amplitude are related by the length of the plasma: $\Delta W_{max} = E_{max}L$

For the long plasma, the theoretical peak unloaded energy gain is 43 GeV (Table 3.1). Assuming a similar level of beam loading for the plasma wakefield in the long oven as in the case of short oven, the expected value for the energy gain in the long oven is in the

	Long Plasma	Short Plasma
$n_0(\mathrm{cm}^{-3})$	8×10^{16}	2.5×10^{17}
$n_b(\mathrm{cm}^{-3})$	4.7×10^{16}	4.7×10^{17}
Λ	1.49	1.49
$K_p R_b$	2.44	2.44
$R_b(\mu m)$	46	26
$E_{\mathrm{max}}^{\mathrm{th}}$ (GV/m)	33.3	55.8
L (m)	1.3	0.3
$\Delta W_{\mathrm{max}}^{\mathrm{th}}$ (GeV/m)	43	18
$\Delta W_{\mathrm{max}}^{\mathrm{exp}}$ (GeV/m)	33	10
$E_{\mathrm{max}}^{\mathrm{exp}}$ (GV/m)	25.4	33

Table 3.1: The interaction parameters as predicted by the 3D nonlinear theory and as measured in the experiments for the short and the long oven. L is the length of the oven as measured using the FWHM of the density profile. All other symbols are defined in the text. The superscript 'th' and 'exp' designate values obtained from theory and experiment, respectively. The $E_{\mathrm{max}}^{\mathrm{exp}}$ for the short plasma is comparable to $E_{\mathrm{max}}^{\mathrm{sim}} \approx 36$ GV/m, the beam loaded peak electric field from the simulation (Section 4). Note that the experimental and simulation values denote those of a beam-loaded wake, whereas the theoretical values are for a wake that is not beam loaded.

range of 19-24 GeV. The results observed from the long plasma corroborate this estimation of energy gain as seen in Fig. 3.5(c) and Fig. 3.6. In some instances, such as Fig. 3.6(a), a disconnect can be observed between the electrons from the main beam and the trapped injected electrons, as was also observed in the short-plasma results. The reason for this is the difference in the relatively larger divergence angle of the drive beam electrons compared with the smaller divergence angle of the injected charge. Consequently, whereas the trapped electrons remain visible well away from the spectrometer's energy focus, accelerated electrons from the tail of the drive-beam have their maximum visibility only near the spectrometer focus (23.35 GeV) as shown in Fig. 3.6(b) and are progressively defocused above and below this point. Meanwhile, the discrete injected beam (e.g. Fig. 3.6(b)) appears as a long narrow stripe even though it is 7 GeV away from the spectrometer focus. In some of the data, the injected helium bunch is well aligned with the signature of the accelerated particles from the drive beam (Fig. 3.6(c)). It is important to note that comparable narrow divergence features do not appear in the case of the short plasma at energies over 20 GeV, supporting the idea that these narrow-energy-spread beams have a different source than the drive beam.

The emittance of the injected beam can be calculated using spectra recorded on a high resolution LANEX screen (instead of the Cherenkov detector shown in Fig. 3.1). An example of data from this screen is shown in the inset in Fig. 3.7(a).

Two features can be seen in this image. The first is the stripe that in made by the injected helium electrons and marked as (1) in this figure. The second is a feature that appears in the center (marked as (2) in the inset of Fig. 3.7) and is made by the accelerated electrons from the drive beam, which come to focus at the energy where quadrupoles of the spectrometer are imaging ($\sim$24.4 GeV), but become invisible quickly because of their large divergence. The feature is wide in X (the horizontal dimension) because, due to the constraints of the imaging quadrupoles, the X and Y foci do not exactly coincide. This second contribution can be observed in Fig. 3.6 as well, where the trajectory of the accelerated drive beam electrons is traced in dashed black line. This contribution can also be distinctly observed in the cases where we turn on the laser and the injected charge disappears (Fig. 3.5(d)). The shape

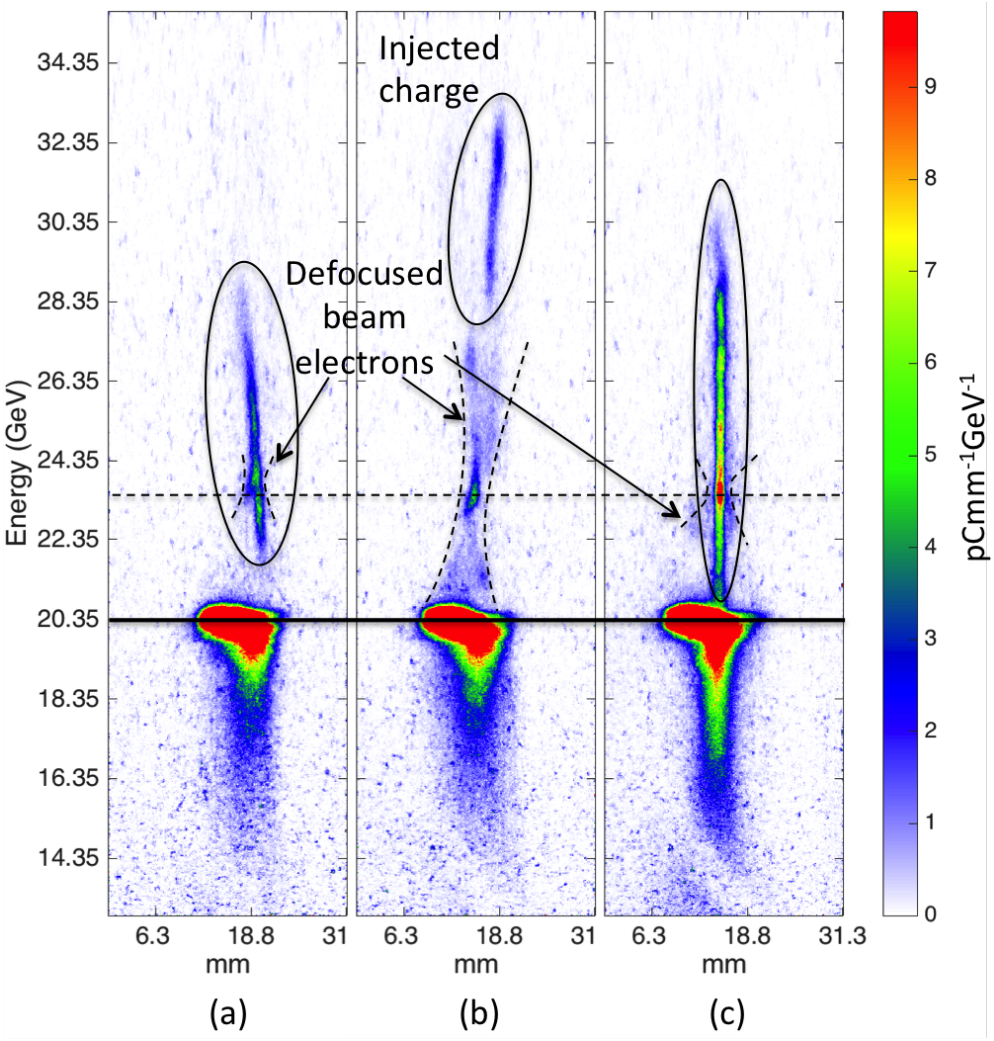

Figure 3.6: Spectra resulting from the interaction of the drive beam with the 130 cm long, 8×10^{16} cm^{-3} plasma. The energy focused by the spectrometer's quadrupole magnets are marked by the dashed black line. The solid black line represents the initial energy of the drive beam. The injected beam in each frame is marked with a solid black ellipse. The outer edges of the defocused beam electrons are traced with two dashed black curves. (a) Example of a narrow divergence feature disconnected from drive beam; the charge is 25 pC. (b) Highest observed energy of the injected charge with limited energy spread. (c) Example of a low divergence injected beam overlapping with the high-energy-spread accelerated drive beam electrons.

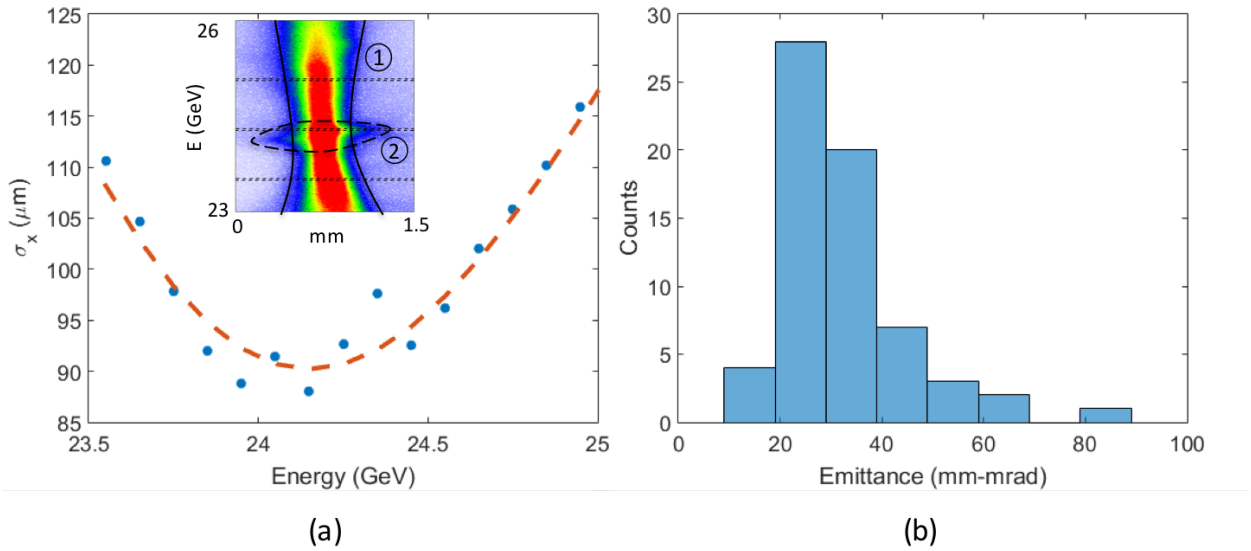

Figure 3.7: Emittance measurement for the injected bunch in the long plasma. (a) Blue circles indicate the values of σ_x at different values of energy for a single spectrum image, which is shown in the inset. The contour of the injected charge is identified by solid black line marked as (1). The dashed black contour identified as (2) belongs to the accelerated electrons of the drive bunch, which are focused by the imaging spectrometer at 24.3 GeV. The top and bottom horizontal black dashed lines in the inset correspond to the highest and lowest energies for which σ_x is calculated. Red dashed line represents the best fit to the data, resulting in emittance value of 36 mm-mrad. (b) Histogram of emittance values ($\epsilon_{n,x}$) for a dataset, where 65 data points belonging to the same dataset could be fit and measured.

and the intensity of this central feature, therefore, is dependent on the current profile of the incoming electron beam and it is observed to vary from shot to shot.

On this high-resolution screen, horizontal lineouts at various energies close to the imaging energy of the spectrometer are fitted with a Gaussian curve and the rms value of the Gaussian at each energy is measured, resulting in a $\sigma_x(E)$ curve, such as the one plotted in Fig. 3.7(a). An iterative, parametric fit based on the configuration of the spectrometer is made to the resulting curve of $\sigma_x(E)$. Using this fit, the beam parameters such as normalized emittance and the location of the waist can be calculated such as was done in [74].

A histogram of emittance values for 65 shots belonging to one dataset is displayed in Fig. 3.7(b), showing emittance values as low as 14 mm-mrad with a mean value of 32 mm-mrad. However, because of the low value of the emittance, only a small number of pixels (on the order of ten pixels) contribute to the measurement. Therefore, there is an uncertainty in the value of the emittance as the measured rms values approach the point-spread function of the optical system. This function is not known for this system, but its effect on the measured values of emittance can be examined by assuming various values for the point-spread function. For instance, the measured value of 21 mm-mrad represents a beam with emittance of 19 and 15 mm-mrad if the point spread function has values of 4 and 7 pixels, respectively. In other words, values reported in Fig. 3.7(b) represent upper estimates for the emittance of the injected beam in the experiment. It is clear that the emittance of the injected electrons (measured in the non-dispersive, x plane) is at least a factor of 10 smaller than that of the drive beam ($\epsilon_{n,x} \sim 358$ mm-mrad) when it is injected into the plasma [43]). The difference in emittance between the injected beam and the drive beam shows the potential for the ionization injection to produce a beam that has a higher brightness than the initial drive beam if the energy spread of the injected beam can be reduced while maintaining its high current.

The region of impurity in this experiment was determined by the boundary region between hot lithium and cold helium. This confined the possible region of helium, but it is way too long and resulted in ionization injection over a long length. The scaling section indicates

that the wake is nearly half loaded. To reduce this loading, it is possible to reduced the region of injection even more. Ideally, the most controlled injection occur over the region that matches the length of one betatron cycle, where the amount of charge will then be controlled by the density of the impurity. This is the subject of next chapter, where a series of simulations are performed with various impurity

3.7 Conclusions

We have shown the ability of ionization injection to produce electron beams at a peak gradient of over 30 GeV/m and with narrow divergence. The electrons are identified as originating from a different source because they are separated from the main drive bunch on the spectrometer and in addition have 10 times smaller emittance than the drive bunch in the plane of the measurement. The injected beam has a charge ranging in tens of pC and has energy spread of several GeV. In order to reduce the energy spread and emittance of the injected charge, the injection region should be limited such that the injection process occurs over a shorter length. Such confined region of helium impurity can be obtained using a capillary setup to inject helium gas within a much longer column of hydrogen and thereby create a localized gas jet used as a narrow region for injection. This technique may lead to the generation of super bright beams needed for future applications.

3.8 Acknowledgements

Work at UCLA was supported by DOE grant number. DE-SC0010064 and the NSF grant number PHY-1415386. Work at SLAC was supported by DOE contract number DE-AC02-76SF00515. Simulations used the Hoffman cluster at UCLA.

CHAPTER 4

Simulations as a Guide for Experimental Design

4.1 Introduction

The experimental results presented in the previous chapter showed that once ionization injection is restricted to the region of the ramp in a lithium plasma (as opposed to the entire length of the interaction), the resulting electron beam appeared with potentially very small emittance. One remaining issue with the results in the previous chapter is that the energy spread of the resulting beam was 10-20%. The process of ionization injection in our experiment occurs due to an increase in the electric field of the drive beam as it pinches during its betatron oscillations. Thus, this energy spread is attributed to the injection region encompassing multiple betatron oscillations. It therefore stands to reason that if the region of ionization injection is restricted to a single betatron oscillation, the energy spread may be greatly reduced.

In this chapter I will show through 2D cylindrically symmetric OSIRIS simulations that one can produce an injected beam with percent level energy spread by designing the ionization injection region to cover only the length of one betatron cycle. Taken together with the experimentally measured emittance, which was much lower than the drive beam produced by the linac, this chapter shows the potential of the plasma wakefield accelerator to produce an electron beam competitive with those produced by a conventional accelerator.

Table 4.1: Beam and normalizations parameters for all the simulations in this chapter. $n_0 = 2.5\times10^{17}$ cm^{-3} is the normalization density used in the simulation, i.e. $c/\omega_p = 10.65$ μm

Parameter	Values
Drive beam charge	2×10^{10}
σ_z (μm)	30
σ_r (μm)	30
ϵ_n (mm-mrad)	120
n_0 (cm^{-3})	2.5×10^{17}
Box Size	720×400
Grid Size	0.05 k_p^{-1}
c/ω_p (μm)	10.65

4.2 Single Betatron Cycle Simulation

To investigate the effect of an injection zone that is only one oscillation cycle long (i.e. half the betatron wavelength), we have performed a 2D cylindrically symmetric OSIRIS simulation with beam parameters shown in Table 4.1. The plasma in these simulations is assumed to be pre-ionized and the region of impurity consists of helium. Helium is implemented as neutral atoms in the simulations and the ADK model is used to model the ionization of helium in the simulations. Experimentally, this configuration is possible using an axicon-produced plasma (see section 3.5 and Appendix A) in hydrogen with the helium impurity being added using a capillary tube.

To explain the important parameters in the simulation, it is necessary to go through one simulation in detail so that for the rest of this chapter the parameters of this first simulation can provide a point of reference while discussing the scalings of various parameters. The density chosen for the preionized plasma (representing hydrogen) in this first simulation (Sim1) is 5×10^{16} cm^{-3}, which for the specified beam and plasma parameters (Table 4.1), results in an envelope oscillation wavelength of 2.1 cm. Therefore the region of helium impurity, representing a helium jet, is designed such that its entire length is confined to 2

Figure 4.1: The setup for the simulation

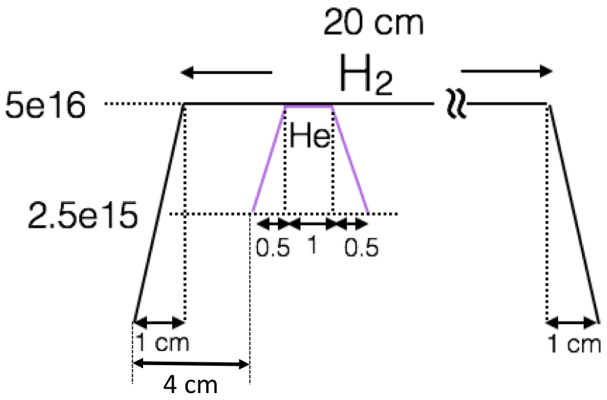

cm. The helium density profile then is modeled as a trapezoid, where the flat region is 1 cm, and two regions of 0.5 cm represent the ramps. Helium concentration chosen here was 5% on the plateau; i.e. the helium density in the plateau region is 2.5×10^{15} cm^{-3}. The helium is injected 4 cm after the start of the preionized hydrogen plasma so that the beam has already produced a fully blown out wake in the pure hydrogen gas. The density layout is presented in Fig. 4.1. For this first simulation, the preionized plasma spans the width of the box (213 μm) to model an infinitely wide column of plasma.

The ionization and injection of helium electrons occurs between 4 and 6 cm in this simulation. A simulation slice taken at 4.5 cm (Fig. 4.2(a)) shows the density map for the electron beam, the pre-ionized plasma and the helium impurity being ionized and injected. The variation in the density of the drive beam is the result of envelope oscillation of the various slices as described in chapter 2. The matched beam radius for the parameters in this simulation is $\epsilon_n(c/\omega_p)\sqrt{2/\gamma_b} \sim 4.5$ μm. Since the σ_z of the drive beam at waist is 30 μm > 4.5 μm, the beam radius oscillates in the focusing field of the ion column. As stated previously, such oscillations of the drive beam slices are asynchronous, i.e. various slices of the beam reach their minimum value at different times. In Fig. 4.2(a), pinching of the particular slice at $\xi = 278.5$ μm leads to an enhancement of the transverse electric field that results in ionization of the helium electrons (shown in blue).

Figure 4.2(b) shows the accumulated helium charge in the wake as a function of distance.

Figure 4.2: (a) A snapshot of density as a colormap 4.5 cm after propagation (immediately after the helium upramp). Helium electrons are represented with blue, the pre-ionized plasma with pink and the beam electrons with red-blue colors (color table shown only for beam electrons). (b) Injected helium charge in the simulation as a function of distance. The two distinct ionization and injection region are marked with (1) and (2). (c) The ξ location of highest transverse electric field for each frame in the simulation. The center of the electron beam density is at 272 μm. The region where no ionization in simulation is observed is clearly marked. (d) Transverse and total electric fields plotted at the location of highest transverse field in the blowout region for each frame in simulation. No ionization injection is observed in frames where $E_{tot} < E_{th} \approx 75\ GV/m$

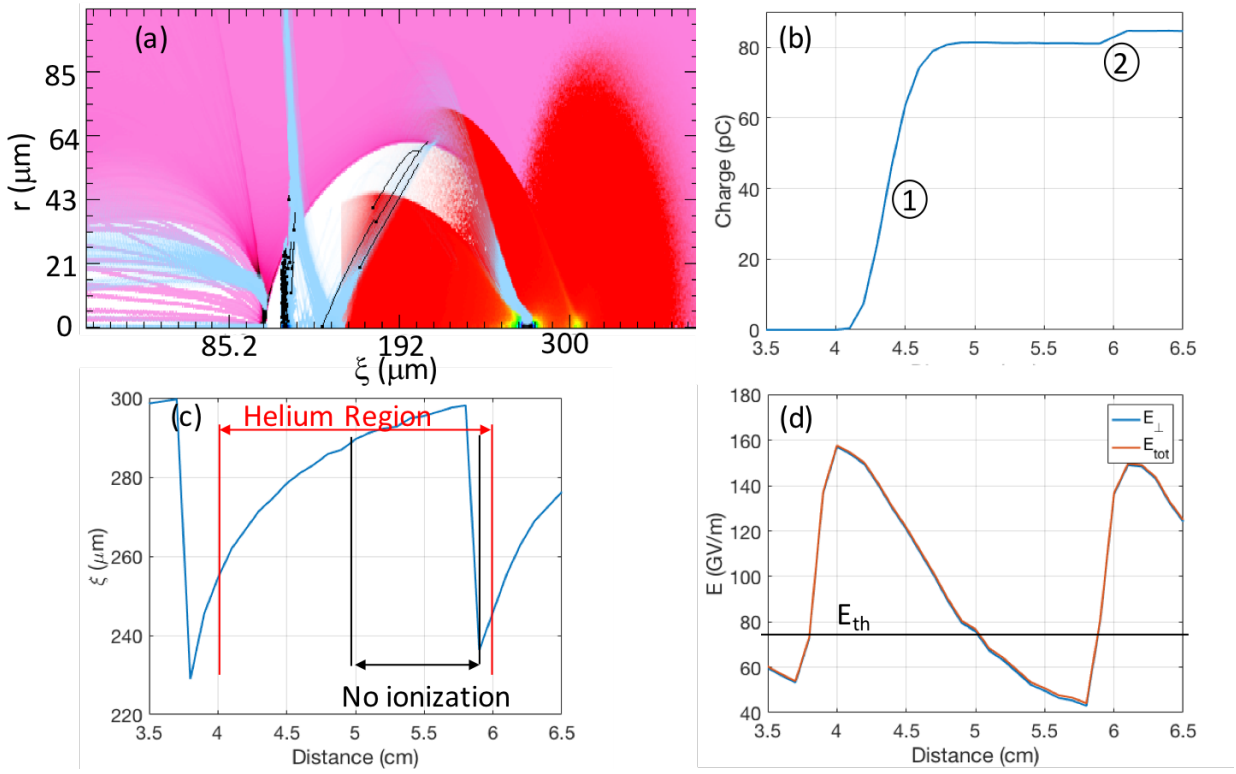

The charge is calculated using the density profile ($n(r,z)$) and equation $Q = 2\pi \int_0^\infty dr \int_{-\infty}^{\infty} dzrn(r,z)$. Two distinct regions of injection are observed in this figure, one between 4.0-5.0 (marked as (1) in Fig. 4.2(b)) and the other between 5.9 and 6.1 cm (marked as (2) in Fig. 4.2(b)). The majority of charge (81.4 pC) is injected between 4 and 5 cm, with the highest portion (78.6) created in the 0.6 cm between 4.1 and 4.7 cm. The second bunch of electrons (region(2) in Fig. 4.2(b)) are generated in the downramp region of the helium impurity region, and therefore result in injection of a small amount (~ 3 pC) of electrons.

The centimeter scale of the region of injection is the result of the various slices reaching the minimum of oscillation at various times, where helium is ionized at the location of the pinch at each time step. This dephasing is illustrated in Fig.4.2(c), where the ξ location of the highest transverse field within the blowout region (i.e. location of pinch) at every time step is plotted. From this image, and recalling that there is no ionization between 5 cm and 5.9 cm, the region of ionization is at 238 μm $< \xi <$ 290 μm. In other words, even though the slices outside of this range pinch, the generated field is not strong enough to ionize helium.

By following the value of the transverse field at the location of the pinch Fig.4.2(d), we find that the value of $E_{th} = 75$ GV/m is the threshold value for the ionization of helium in this simulation. Using the ADK model, and by measuring the width of the pinch for frame corresponding to 5 cm of propagation, we find that the pinch has a $\sigma_{zp} = 4.5$ μm, resulting in a calculated ionization fraction of 12% with the value of peak electric field at 75 GV/m. ADK analysis shows that for such a σ_{zp}, an electric field of below 70.5 GV/m would be below the simulation's ionization threshold rate of 6.25%. This threshold is the result of having 16 particles per cell for helium, where an ionization rate above 6.25% results in ionization of one of these particles. The total field in the simulation drops below 70 between 5 and 5.1 cm in agreement with the ADK calculation. Furthermore, the pinch density at 5 cm is 22, i.e. pinching a slice to a density of greater than 22 times initial peak density will ionize helium.

Both the total field and the transverse field are plotted in Fig. 4.2(d), and it is clear that at this density, the electric field at the location of the pinch is completely dominated by $E_\perp$. Measurement of E_z at the location of the pinch (not shown) indicates that it is an order of

magnitude smaller than $E_\perp$ and therefore does not really contribute to the ionizing electric field in this simulation.

Fig.4.2(d) shows furthermore that in this simulation, the region of helium starts near where the electric field of the pinch is at its highest value (4 cm). The separation between the two regions of ionization corresponds to where the field of the pinched beam is below the ionization threshold and the increasing electric field above the E_{th} in the next oscillation cycle catches the tail end of the helium density down-ramp between 5.9 cm and 6.1 cm, producing the 3 pC marked as region (2) in Fig. 4.2(b). In the experiment, the overlap region will be difficult to control, however by having the region of the helium impurity span the length of the oscillation cycle of the beam, it can be ensured that for some region the threshold of helium ionization will be exceeded and those electrons are injected into the wake.

The FWHM of the current profile is only 2.1 μm, which creates a peak current of slightly over 8 kA as shown in Fig. 4.3(a). As a comparison, the drive beam at FACET has $\sim$ 13 kA of peak current. Helium electrons are ionized over a range of $0.5 < \bar{\Psi}_i < 1.4$ (Fig. 4.3(b)), and they will reach the trapping energy at various locations in the accelerating field, settling in different, but close ξ in the accelerating phase. There are two factors contributing to the narrow current profile. First, $\bar{\Psi}(\xi)$ has a higher slope in the trapping region than the ionizing region, so although the range of $\bar{\Psi}_i$ corresponds to 50 μm, the corresponding $(\Psi_i - 1)$ has a range closer to 20 μm. The ξ corresponding to the interval with the highest charge produced (4.3-4.4 cm) has $\bar{\Psi}_i \approx 1$. The peak of the current corresponds to $\xi \approx 120$ μm, which has a $\bar{\Psi}_i \approx 0$. Therefore the location of injection corresponds with the $\bar{\Psi}_i - 1$ for the ξ location with the highest charge contribution. Second, the order over which the ionization occurs can result in current profile steepening. for instance, if an electron with $\bar{\Psi}_i < \bar{\Psi}_{i1}$ get ionized before the electrons with $\bar{\Psi}_{i1}$, the extra time the first electron spends in the accelerating field may equal the difference in energy as a result of the difference in $\bar{\Psi}_i$, resulting in the two electrons occupying the same position, and steepening the current profile.

The 84 pC of injected charge is stable after the injection ends and gets accelerated to a

peak energy of 6.3 GeV (Fig. 4.3(c)) with an energy spread of 2.7% FWHM. This charge is very stable throughout the simulation and is maintained over the ~ 17.6 cm of acceleration. The peak energy gain is 6.3 GeV, which corresponds to an accelerating gradient of about 36 GV/m. The energy spectrum of the beam shows that the peak energy loss over the 22 cm is 2.64 GeV (see Fig. 4.3(d)), which corresponds to 12 GV/m peak decelerating gradient. Therefore, In this case, the transformer ratio is 3.

It is important to note that as expected, the blowout regime forms after some propagation distance. In this case, after 1 cm the blowout regime is fully formed and does not evolve appreciably throughout the plasma region. Additionally, the predictive quality of the 3D blowout theory is successfully demonstrated in these simulations. In this case, $\Lambda \approx 1.5$, and therefore $k_p R_b \approx 2.44 \approx 58.2$ μm. It can be observed that the maximum blowout radius in this simulation matches the expected value of R_b almost exactly.

4.3 Density Scaling Observed in the Simulation

To study the effect of the density of the plasma and impurity on the future experiment, the results from four simulations are compared in this section. The basis of the comparison is the simulation presented in the previous section. These parameters of the simulations are tabulated in Table 4.2.

First, the plasma density is scaled from 5×10^{16} cm^{-3} to 2.5×10^{17} cm^{-3} in two steps (Sim1-Sim3), while keeping the helium density the same. Because the betatron oscillation wavelength scales with density, the length of the helium impurity is also selected such that it matches the length of one envelope oscillation cycle (equal to half a betatron wavelength) in each case. An additional change was to the start of the helium impurity region, which was moved to 3 cm from 4 cm in order to save on simulation time. Because of the stability of the blowout regime, this change does not have a significant impact on the results. The drive beam is the same for all simulations.

In the fourth simulation, the plasma density is kept at 2.5×10^{17} cm^{-3}, while the helium

Figure 4.3: (a)Current profile of the injected helium charge after 17.6 cm of propagation in plasma. (b) Plot of on axis $\bar{\Psi}$ after 4.4 cm of propagation. The lowest and highest range of $\bar{\Psi}_i$ that lead to ionization and injection are marked as $\bar{\Psi}_{i1}$ and $\bar{\Psi}_{i2}$. The corresponding ξ where $\Delta\bar{\Psi} < 1$ is also marked for each case (c) Energy spectra for the injected helium electrons. (d) Energy spectra for the drive beam

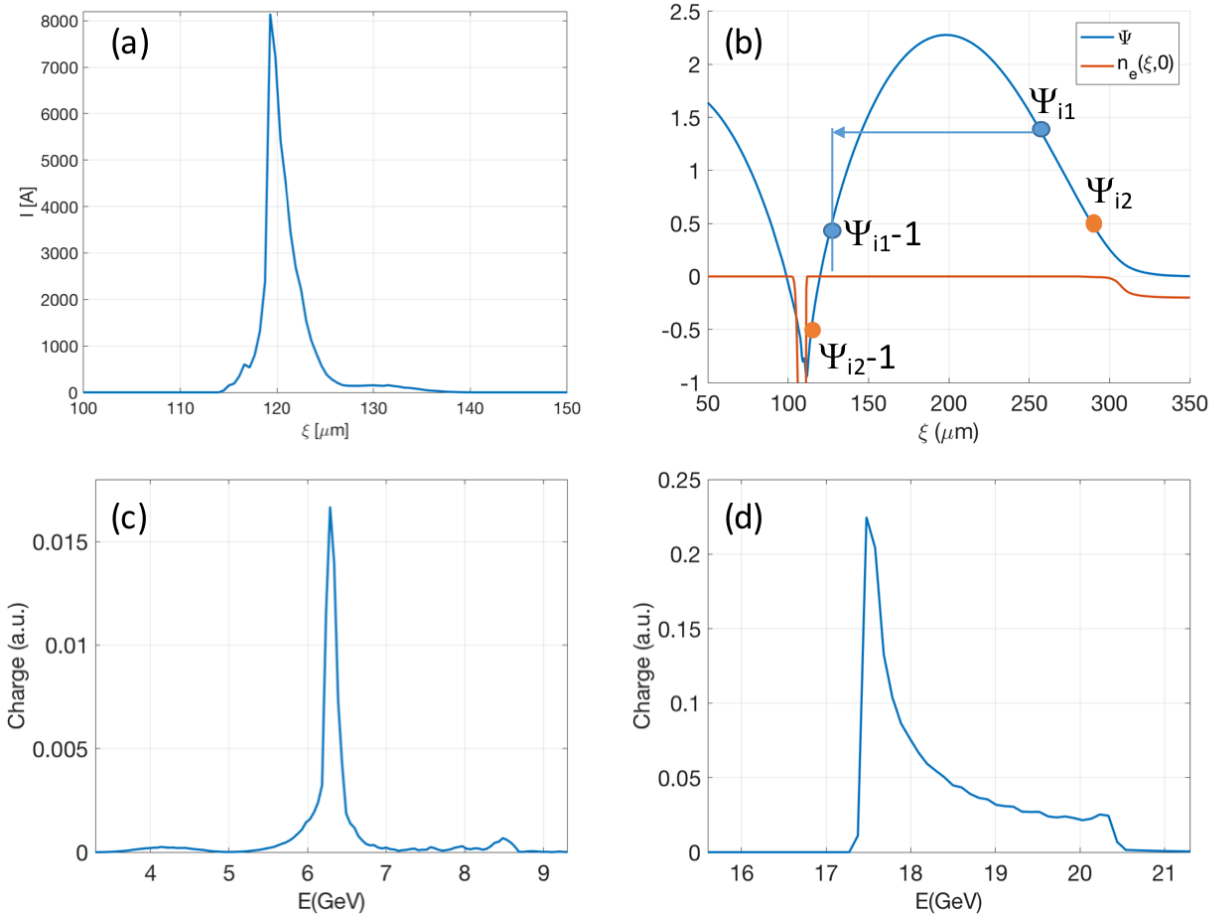

Table 4.2: Simulation parameters for demonstration of density scaling of the simulation. The length of the helium region includes the length of the ramps, whose length is also scaled for each density

Name	H_2 Plateau Density	He Plateau Density	Length of Helium Region
Sim1	5×10^{16}	2.5×10^{15}	2 cm
Sim2	1.12×10^{17}	2.5×10^{15}	1.4 cm
Sim3	2.5×10^{17}	2.5×10^{15}	1 cm
Sim4	2.5×10^{17}	1.26×10^{16}	1 cm

plateau density is raised to 1.25×10^{16} cm^{-3}, so that the impurity level is raised to 5% , which matches the impurity percentage of the first simulation.

4.3.1 Scaling of Plasma Density

Comparing the helium charge in Sim1-Sim3 shows that the amount of the injected charge is higher at higher densities (Fig. 4.4(a)). The higher charge is attributed to the longer ionization length for simulations at higher densities. In the case of Sim3, the ionization and injection length is about two times longer than Sim1. The first injection zone in Sim2 is roughly the same length as Sim1, except that the ramp is shorter (since helium length is scaled with density) and therefore helium density is higher, resulting in higher slope in the charge curve.

To understand the longer injection length of Sim3 compared to Sim1, it is important to compare the electric fields at the location of the pinch in each frame (Fig. 4.4(b)). It can be seen that as density is increased, the peak of the field is reduced and the valley of the field is raised. In other words, the peak to peak difference in the electric field decreases as the density is increased. Therefore, the range of length that falls below E_{th} decreases as the density increases and for Sim3, there is no length where the electric field is below the ionization threshold. This fact has important implications for the experiment because if the length of the helium impurity produced by a capillary is on the order of 1 cm, one can conceivably

Figure 4.4: (a) Measurement of injected charge as a function of distance in the simulations. The beginning of the helium impurity is set to zero. Sim1 is shown in blue, Sim2 in orange, and Sim3 in yellow colors. Same colors are used in all sub-figures(b) Total electric fields as a function of distance for the same three simulations. (c) The 80% plasma density contours for the same three simulations after 3 cm of propagation in the plasma in addition to the density color map of the initial drive beam. The location of ξ where the transition between full and partial blowout occurs is marked by an arrow for each case.

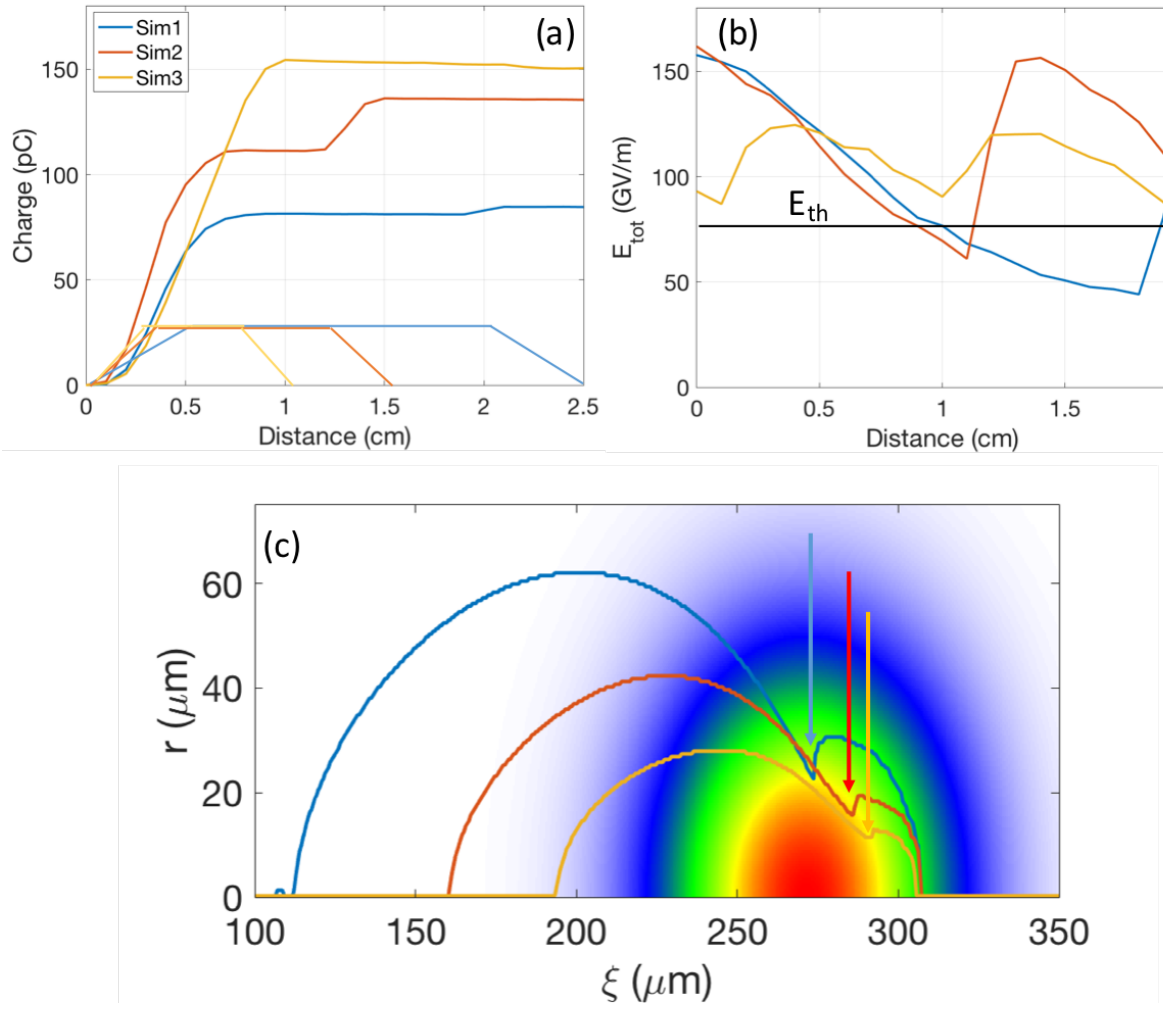

miss ionizing and injecting the electrons if the experiment is at a density of 5×10^{16} (case of Sim1). Therefore, by raising the density, while keeping all other parameters the same, it is possible to transition the experiment to a regime where the ionization injection condition can be continuously satisfied over the envelope oscillation length and thus the length of the injection region is entirely determined by the length of impurity, i.e. over 1 cm for the case of Sim3.

The scaling of the electric field with density can be explained from exploring the blowout regime properties at various densities (Fig. 4.4(c)). In this figure, the 80% density contour for the various densities is superimposed on the initial electron beam density. Because of the finite blowout distance, which is given by $\frac{2}{k_p}\sqrt{\frac{n_p}{n_b}}$ [46], there is a region with partial electron density before the blowout region (i.e. $n_e = 0$) is reached. More importantly, because of the density dependance of the blowout distance, the blowout forms in a smaller distance for the higher density, meaning that in some region (i.e. $\xi \sim 280 - 290$ μm), the high density simulation (e.g. Sim3) reaches blowout but the lower density simulation (Sim1) does not. The beginning of the blowout region is marked with an arrow for different simulations in Fig. 4.4(c). The lowest field occurs on the front ($288 - 298$ μm from Fig. 4.2(c)). This is the region that is not fully blown out in the lower density Sim1 simulation, whereas in Sim3, this region is in full blowout regime, therefore, there is a higher ion force and stronger pinch, leading to increased electric field. The maximum of the electric field occurs near the center of the beam $\xi_0 = 271.6$ μm. In this region, both simulations have reached blowout, and the blue blowout contour belonging to Sim1 encompasses more charge than the higher density yellow contour belonging to Sim3. Additionally, the blowout formation process for this slice involves a gradual increase of positive density that resembles the presence of a density ramp such as the one described in Chapter 2. In other words, as the electron density slowly decreases for this slice over a distance of about 1 cm, the betatron oscillation is modified and σ_r pinches harder at the valley of the oscillation. This leads to a higher electric field at the pinch point for the lower density simulation Sim1. As a result of these differences in the formation of the blowout regime, the peak to peak field in the case of the high density Sim3 is lower than that of the lower density Sim1.

The resulting helium beam's energy spectra after about 6 cm of propagation for the three simulations is shown in Fig. 4.5(a). The energy spectra can be observed to have distinct peaks with low energy spread, which is a very desirable quality for an accelerator. Furthermore, the current density profiles shown in Fig. 4.5(b) show that the current is also high and has a distinct peak. It noteworthy that even though more charge is injected in the case of the high density simulation (Sim3), its peak current is lower. This is because in the case of Sim1 and Sim2, the electric field reduces below the ionization threshold for $\xi \geq 290$ μm, restricting the range of $\bar{\Psi}_i$ for the ionization injected electrons to less than 1(Fig. 4.5(c)). In the case of Sim3, however, beam pinching over all values of ξ result in ionization, increasing the range of $\bar{\Psi}_i$ by 50% to about 1.5 . Therefore, electrons ionized in Sim3 satisfy the trapping conditions at $\Delta\bar{\Psi} > -1$ at a larger range of ξ in the accelerating phase of the wake and result in a wider current profile than the other two cases.

The longitudinal accelerating field is plotted for Fig. 4.5(d) for the same cases, showing that the beam loading due to these high current beams does not result in field flattening over the range of the beam current. Therefore, the energy spectra tend to evolve. However, because of the very high peak current and very localized nature of the injected charge, the widening of the energy spread due to variation in the local field is very small, and therefore the peaked nature of the energy spectra is preserved to the end of the simulation as was shown in Fig. 4.3(c) for Sim1 in the previous section.

4.3.2 Scaling of Accelerated Bunch Parameters with Impurity Density

The increase in helium impurity density (Sim4) resulted in the injection of higher charge as expected. It is noteworthy however that while the helium impurity density was raised 5 folds from 1% to 5%, the injected charge initially increased eight folds to 1.2 nC. In fact the blowout region at the density of simulation (2.5×10^{17} cm^{-3}) could not support this level of injected charge and as seen from Fig. 4.6(a), the trapped charge decreased until stabilizing around 700 pC after 5 cm of propagation from the start of helium region (marked zero in Fig. 4.6(a)). It is also important to note that the charge shown in Fig. 4.6(a) accounts

Figure 4.5: (a) Energy spectra for Sim1-3. The spectra in each case is shown 5.7 cm after the beginning of the helium region. The same colors used in all four figures (b) Current profiles of helium injected charge for Sim1-Sim3, with each curve normalized to the peak current for that case (I_p). The legend shows the value of peak current in each case in amps. (c) The value of Ψ_i corresponding to the pinch in each frame. The range over which no electrons are ionized and injected are marked by double-sided arrows. (d) The longitudinal field corresponding to the three cases.

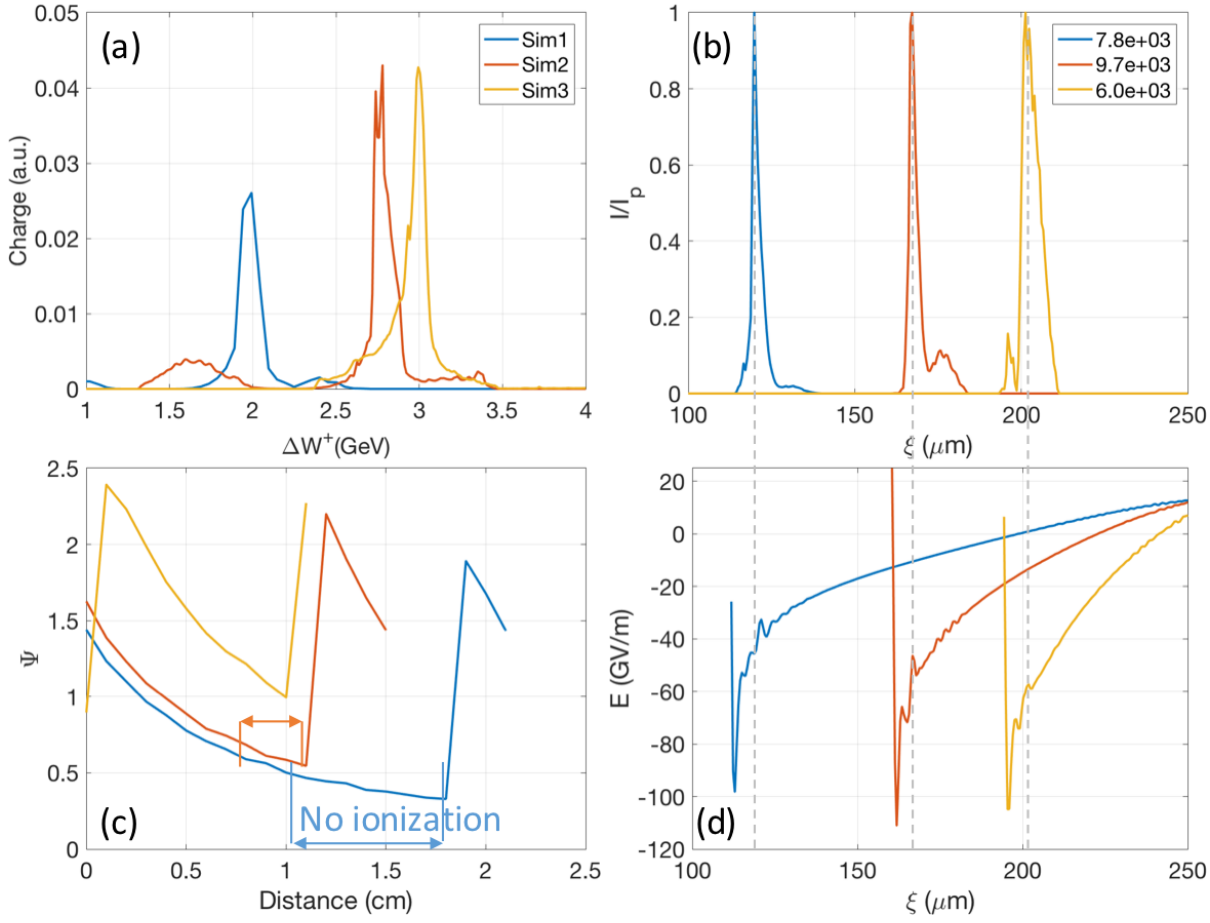

only for the charge inside the first blowout region. The total helium charge injected in the simulation was over 1 nC after 5 cm of propagation from the start of helium region.

The normalized current profile Fig. 4.6(b) of Sim4 is similar to Sim3 because the range of $\bar{\Psi}_i$ is not affected by the level of impurity. With the increased helium charge in the same current profile however, the resulting peak current was increased to 17 kA, 30% higher then the current of the drive beam. The current observed at $\xi \sim 150$ μm is not trapped on axis and does not belong to the first bucket. Rather, it belongs to a ring structure that is formed as a result of the high field of the trapped charge and the modification of the electron trajectories belonging to the blowout sheath. This modification results in a region of partial blowout outside the sheath that supports the formation and acceleration of a ring in the simulation.

The energy spectra of Sim4 shows a multiply peaked structure with the energy of the highest peak around 2.5 GeV compared to 3 GeV for the electron beam in Sim3 after the same acceleration distance in plasma (Fig. 4.6(c)). However, since the amount of charge accelerated to 2.5 GeV in Sim4 is about 2.4 times higher than the charge accelerated to 3 GeV in Sim3, the electron beam in Sim4 has absorbed twice the energy out of the wake than the injected beam in Sim3, i.e. drive to trailing energy transfer efficiency in Sim4 is twice as high as Sim3. Additionally, it is also noteworthy that a large amount of helium charge in this experiment gains less than 500 MeV.

The higher efficiency and the heavy beam loading in Sim4 are observed in the longitudinal field of Sim4 in Fig. 4.6(d). This three fold increase in helium beam current resulted in heavy beam loading of the accelerating field in Sim4. It can be observed for instance that a significant amount of charge at $\xi < 200$ μm experiences an accelerating field on the order of 10 GV/m or less. These are the electrons that gain less than 500 MeV in Fig. 4.6(c).

Additionally, the amplitude of the wake behind the injected beam is significantly reduced compared to Sim3. This is an indication of high drive to trailing efficiency of the accelerator, as the energy previously stored in the field of the wake has been absorbed by the increase helium charge.

Figure 4.6: Comparing the results of Sim3 and Sim4, where the helium density is increased by five folds. (a)Injected charge in the first bubble as a function of distance. Zero indicates the beginning of helium region (3 cm of initial beam propagation in both simulations). The same color is used in the rest of the sub figures (b) Current profile as a function of ξ for both simulations normalized to the peak value of current in each case. The value of peak current in each case is shown in the legend of the figure. (c) Helium spectra in the two cases after 5.7 cm of propagation from the beginning of helium region. (d) Longitudinal electric field compared in both cases.

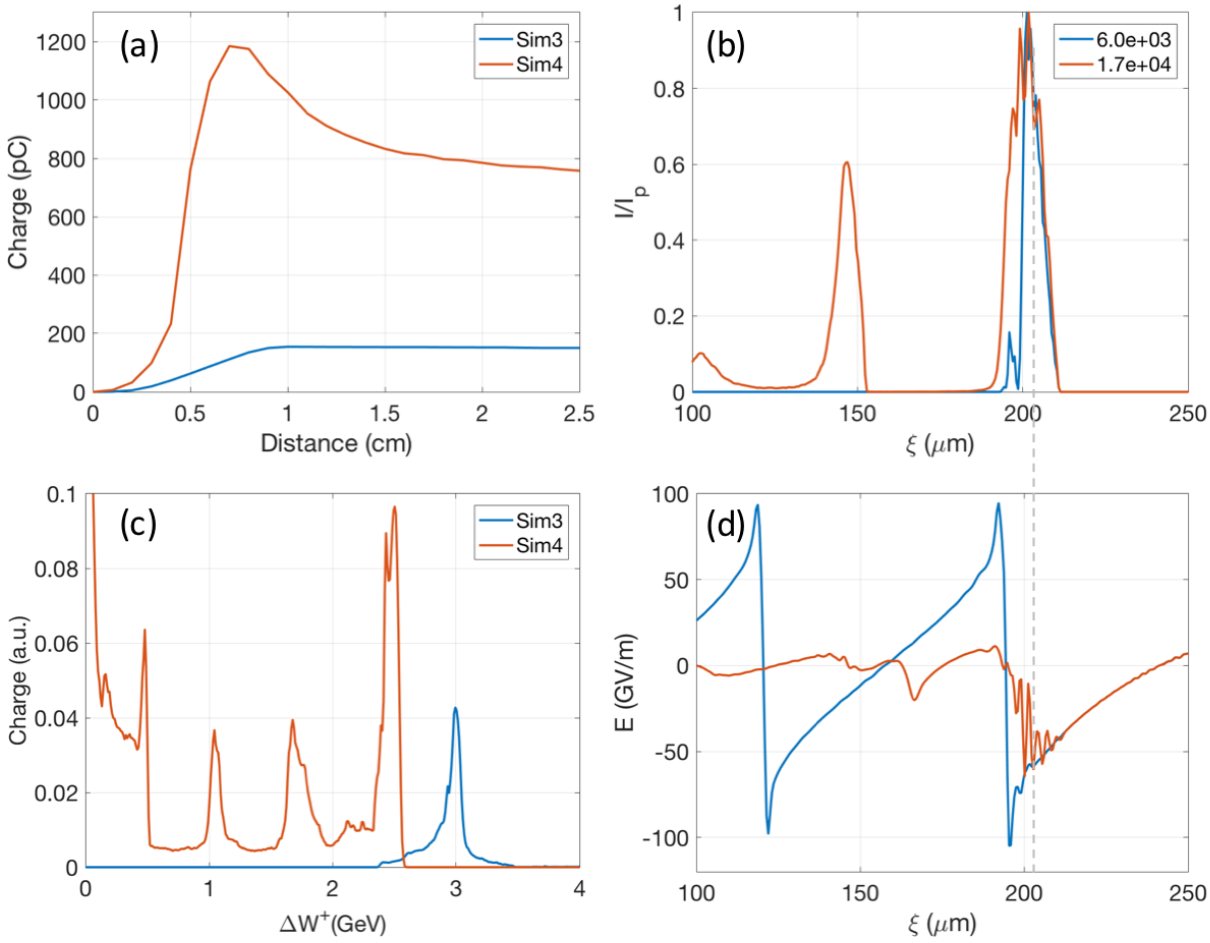

Finally, the longitudinal field ahead of the injected beam current is the same for Sim3 and Sim4 as expected because of causality.

The comparison between Sim3 and Sim4 shows how one can increase the charge and current of the trapped particles by simply increasing the helium impurity in the experiment. Although a five fold increase represents a large increase in impurity density and resulted in features such as a large amount of charge with low energy, which might be undesirable, one can choose an intermediate helium concentration (around 2-3%) in order to minimize the undesirable effects, while still gaining more charge and current in the injected beam. Another effect that accompanies the increase in the injected charge is the higher energy transfer efficiency from the drive to accelerated charge, which is also very desirable for an accelerator. Additionally, other interesting phenomena such as multi-peak energy spectra and a ring of accelerated charge may appear as the impurity levels are increased.

4.4 Emittance Measurement in a 3D Simulation

A 3D OSIRIS simulation in cartesian coordinates was performed to measure the emittance of the injected beams. The simulation uses the parameters of Sim 3 (See Table 4.2), except the helium region is set to 2 cm, which is twice the length of betatron oscillation cycle. This last change was made to observe the difference in the electron beams produced in consecutive betatron cycles. The parameters for the electron beams reported in this section are at $z = 6.2$ cm, or 3.2 cm from the beginning of helium region.

260 pC of helium electrons were trapped in the simulation, producing a peak current of over 8 kA (Fig. 4.7(a)). The electrons generated by the two betatron oscillations create two distinct beams that are clearly separated in the spectrum by 0.5 GeV (the higher energy peak is 1.4 GeV and the lower energy peak is 0.9 GeV as shown in Fig. 4.7(b)). Since the betatron oscillation at this density are about a centimeter apart, the accelerating gradient is estimated as about 50 GV/m, which is consistent with beam loaded accelerating field at this density (see Fig. 4.6). It can also be observed that in terms of beam characteristic, the

two beam are very similar, with very similar peak charge density, energy spread, and energy profile.

The similarity between the two beams is further reinforced by observing the longitudinal phase space as seen in Fig. 4.7(c). The trapping of electrons at various ξ locations can be observed in the phase space. Additionally, it can be seen that the tail centered around 29 μm in Fig. 4.7(a) is actually made of a spray of wide energy spread charge, that can be observed as a weak background overlapping the two peaks in the energy spectra in Fig. 4.7(b).

Because of the clear distinction between the two injected beams, it is possible to calculate the emittance of the beams resulting from each betatron cycle separately. In this instance, the higher energy electron beam, which was injected the earliest has $2400 < \bar{p}_z < 3000$ and $6.20364\text{cm} < z < 6.205$ cm, and the lower energy electrons are confined to $1200 < \bar{p}_z < 2000$ and $6.2037\text{cm} < z < 6.2051$ cm.

The raw parameters for the 10% of the helium injected charge in the simulation are recorded in each frame, making the direct measurement of position and momentum for those electrons possible. The emittance is calculated using equation $\epsilon_{gi} = \sqrt{< x_i^2 >< x_i'^2 > - < x_i x_i' >^2}$, where the i subscript equals to 2 or 3 refers to the variables in the transverse dimension, x represents a position in the transverse coordinate, and the $x_i' = \bar{p}_i/\bar{p}_z$ represents the transverse angle. It is important to note that there is a 'drift' in the transverse coordinate, i.e. x_2 and x_3 are not centered at zero. Therefore the mean value of transverse parameters is first subtracted before calculation of emittance.

The phase space for the high energy beam in x_2 is shown in Fig. 4.7(d). The rms values for the size and angle are 1.4μm and 1.8 mrad respectively. The geometric emittances for the high energy beam therefore are $\epsilon_{g2,3} = 2.5$ nm, and for the low energy electron beam are $\epsilon_{g2,3} = 4.1$ nm.

The normalized emittances are calculated using $\epsilon_n = \gamma\epsilon_g$, where $\gamma = \langle\sqrt{1 + p_{total}^2}\rangle$ is the mean Lorentz factor for the electrons in the simulation. For the high energy beam, the normalized emittance then equals 7.1 mm-mrad and for the low energy beam equals 7 mm-mrad. It can be seen that the two beams are also very similar in normalized emittance.

Figure 4.7: Results of the 3D cartesian simulation after 6.2 cm of propagation. (a)Current profile of the helium electron beam in the simulation.(b) Energy spectral density for the helium charge in the simulation. (c) Longitudinal phase space (z, p_z) for the helium electrons. (d) Transverse phase space for the higher energy injected electrons (indicated by black lined rectangle in (c)), which is produced in the first oscillation cycle.

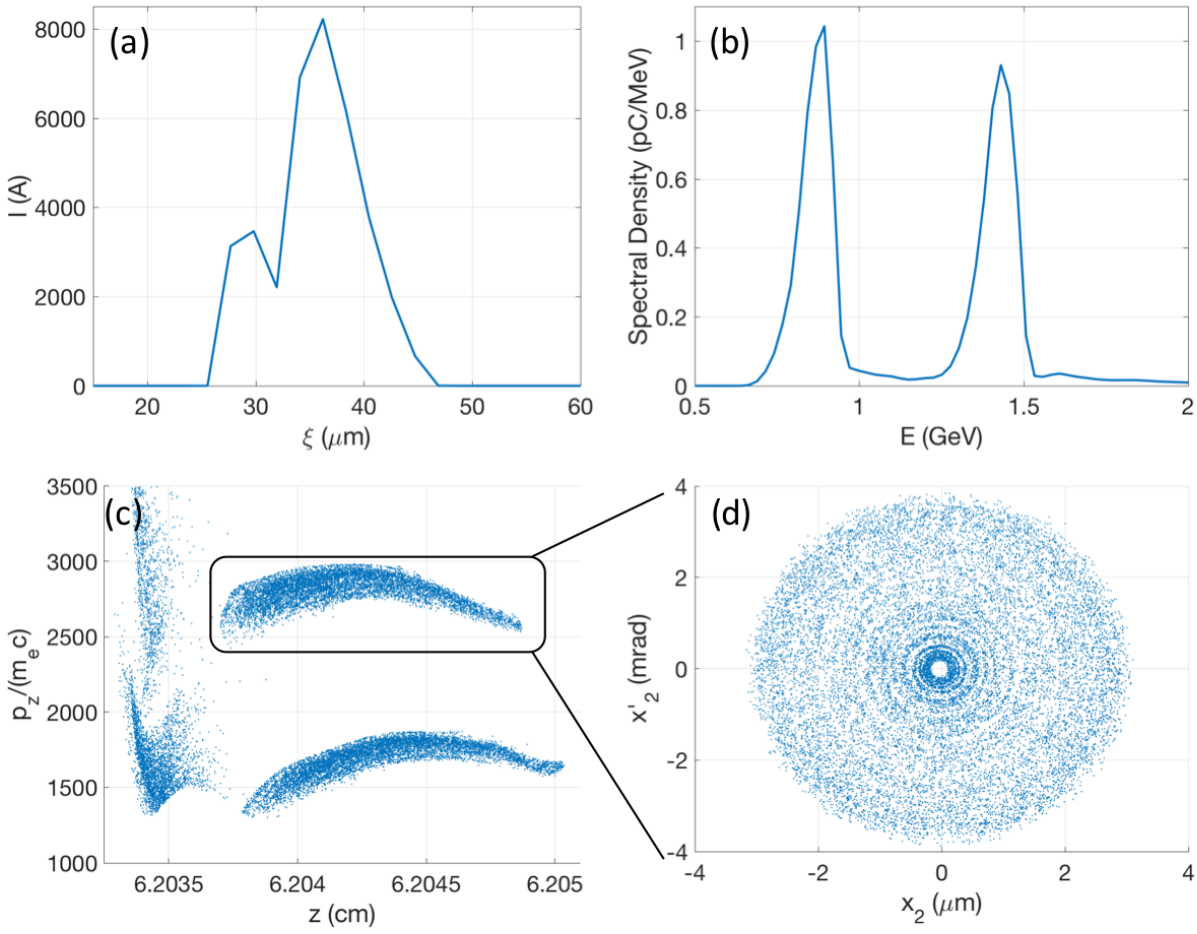

It is also possible to calculate the emittance of the entire beam including the wide energy spread electrons at the back of the wake. In this case, the calculations show that $\epsilon_{g2,3} = 2.9$ nm and $\epsilon_{n2,3} = 6.5$ mm-mrad. The rms size and angle of the total beam is $\sigma_x = 1.4$ μm and $\sigma_{x'} = 2.0$ mrad. Despite the larger divergence compared to the individual beams created, because the mean energy is lower than the highest energy electron bunch, the emittance is reduced by about 10%.

The 3D simulation performed shows the potential for the betatron oscillation to generate a beam that has a micron level emittance.

4.5 Effect of Change of Plasma Column's Radius on Acceleration

The aforementioned simulations were performed assuming a wide plasma. In this case plasma width in the box was 213 μm, whereas the blowout radius $R_b \approx 27 - 53\mu$m. An important point of inquiry is what happens to the fields when the width of the plasma column becomes comparable to R_b. This is an important question to answer experimentally, because a plasma that is generated by focusing a modest laser power ($\sim$ 10 TW Ti:Sapphire) with an axicon in a neutral density back-filled gases such as hydrogen can have a very small radius ($\leq 3\sigma_r$). Therefore, it is important to know whether the blowout regime can be sustained with small radius plasma as it is with a wide plasma.

Another important question is whether the interaction of the edge of the plasma column with the blowout regime of similar size can result in injection of electrons as a result of such interaction rather than being produced by ionization injection. For this reason, the series of simulations in this chapter are performed without helium to investigate possible injected charge with other origin. To investigate such effects therefore, it is important to investigate the result of reducing the width of the plasma column on the interaction.

A series of simulations are reported in this chapter with the plasma density of 2.5×10^{17} cm^{-3} and with various plasma columns widths, such that the radius of the plasma is approximately $2R_{b0}$, R_{b0}, and $R_{b0}/2$, where R_{b0} is the blowout radius established in an

Table 4.3: Simulation parameters for the various plasma column width. H_2 Plateau Density for all cases is 2.5×10^{17} cm^{-3}

Name	r_p (μm)	R_{b0} Multiple
Sim3	213	8
Sim5	53.3	2
Sim6	26.6	1
Sim7	13.3	1/2

infinite plasma. At 2.5×10^{17}, and using the beam described in this chapter, the blowout radius R_{b0} is about 27 μm. The properties of the simulations performed in this chapter are shown in Table 4.3. The Sim3 described in the previous section is used as a baseline to compare the results of this section with.

An important observation in these simulations is that blowout regime was established at all of the various width of the plasma column, even when $r_p \sim R_{b0}/2 = 13.3$ μm. This can be observed in Fig. 4.8(a), which shows the 80% density contour for the various simulations. This is because even with small column width, the blowout regime evolves such that there are enough ions in the blowout to balance the field of the electron beam. This will not be the case if for instance σ_r is reduced to 15 μm from 30 μm that was used in these simulation. In the case of $\sigma_r \sim 15$ μm, the work done by the transverse field of the beam is much higher than the work done by the ion column. In such a case, a wake is not formed. Instead, the sheath electrons are continuously pushed away from the axis and therefore the high accelerating field of the blowout regime is not produced.

Figure 4.8(b) and (c) show that the longitudinal and transverse fields generally decrease for a plasma column with smaller width. An interesting point is the similarity of the fields for the cases of Sim3 and Sim5, where the plasma column is reduced from 213 μm to $2R_{b0} \sim 53.3$ μm. It is clear that the results of a well aligned 100 μm diameter plasma column are essentially equivalent to infinitely wide plasma at this density.

Although the value of the fields generally decrease in narrower plasma column, an

anomaly is the peak transverse field in the case of $r_p = R_{b0}$ compared to $r_p = 2R_{b0}$, where r_p is the plasma column radius. This is because the process leading to establishing of the blowout regime is different in these cases as can be observed from the difference in the established blowout in Fig. 4.8(a). The evolution of the plasma density in the narrower column is analogous to the lower plasma density ramp in a lithium plasma, which was described in Chapter 2. In both cases, the beam evolution in the non-uniform plasma results in stronger pinch (i.e. lower σ_r at the valley of oscillation) and higher peak field, even with the reduced participating charge. However in the case of $r_p = R_{b0}/2$, the participating charge reduces so much that the peak field is reduced precipitously even at tighter pinch.

The longitudinal field gradually decreases in amplitude as shown in Fig. 4.8(c). This is expected because the longitudinal field scales with $k_p R_b$ (Eq. 1.9) and since R_b is lower for narrower plasma column, the longitudinal field also decreases for that case.

The variations in these fields have important implications for the experiment. In the case where the plasma column is $R_b/2$, the transverse field is below ionization threshold and the longitudinal field is so week that no trapping occurs even in the case where electrons are produced inside the blowout region. In contrast, the case where the plasma column radius is equal to R_{b0}, the longitudinal field is intermediate and the transverse field is actually higher. Injection can occur if the electrons are released inside the blowout, and the transverse field is strong enough to ionize helium electrons. Therefore, an intermediate radius may be found such that the longitudinal field can still lead to trapping while the peak transverse field is just below the ionization threshold. In such a case, it is conceivable to experimentally trap over an even smaller range of distance and obtain a higher quality electron beam. Based on the density scaling of simulations in the last chapter, this final step may be easier to achieve in lower density simulations (such as 5×10^{16} cm^{-3}), where the contrast between the highest and lowest transverse peak is even higher.

Finally, it is important to note that despite the evolution of the plasma density to establish the blowout regime, no electrons were injected from the background plasma (whether from the edge or otherwise) into the blowout region.

Figure 4.8: Comparison in cases with different width of plasma column. (a) 80% density contour of the simulations superimposed on the density color map of the initial electron beam (before interaction with plasma) (b) Total field as a function of distance. Zero corresponds to the beginning of helium impurity region for Sim3, corresponding to 3 cm of propagation in plasma. (c) Longitudinal electric field in the same cases as (a). Note that curves for $8R_{b0}$ and $2R_{b0}$ almost exactly overlap in the figures, resulting in $8R_{b0}$ data to be hidden from view under $2R_{b0}$ curves

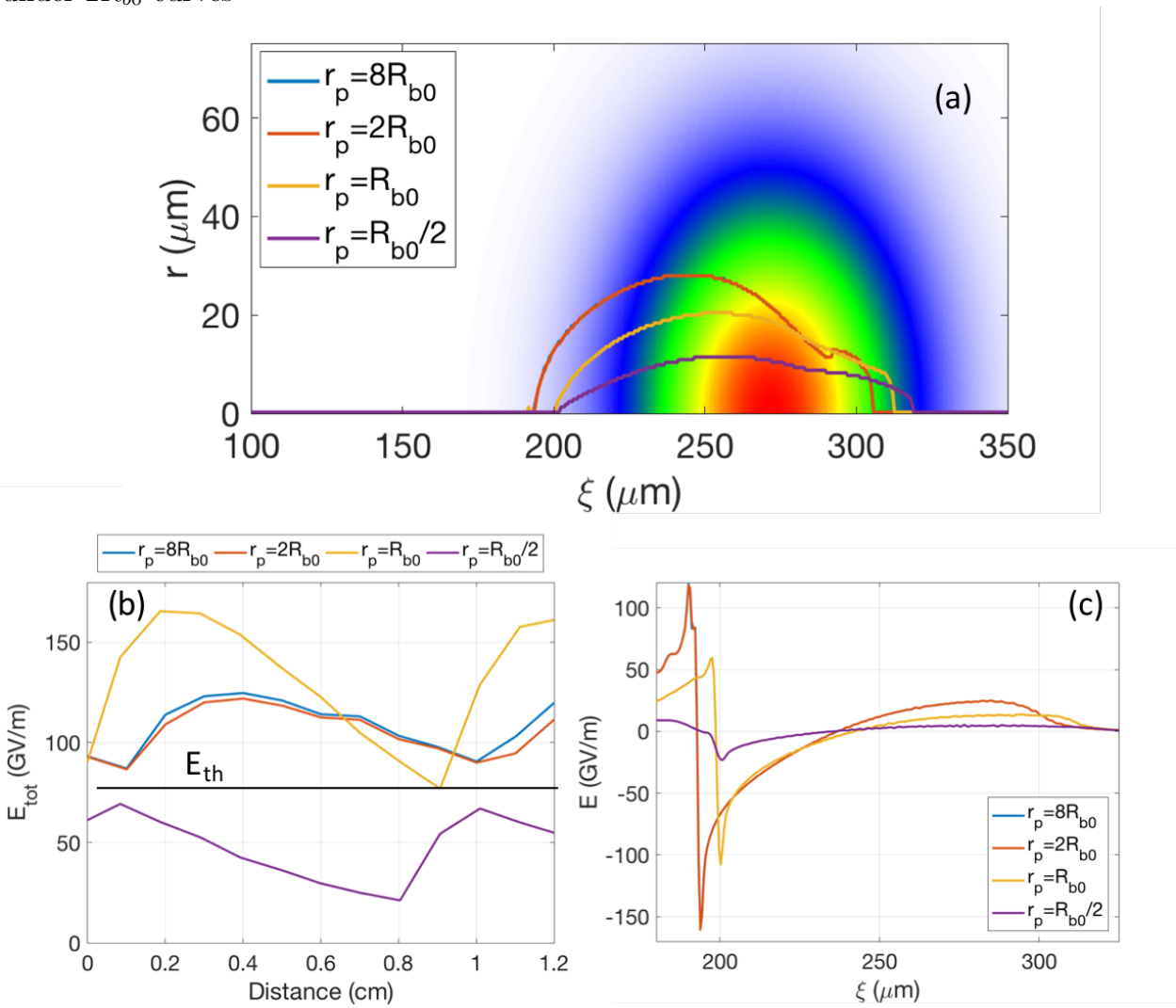

In summary, the simulations performed in this chapter show that limited injection of charge in the blowout regime can produce high current, low energy spread electron beams using a helium impurity in preionized hydrogen plasma. Furthermore, it was shown that several methods can be used to optimize the injected beam, including raising the preionized plasma's density to raise the minimum field observed in beam pinch, raising the impurity density for higher injected charge and current, and finally, reducing the plasma column's width, which if done in a controlled way, can be used to tune the length of injection by controlling the produced fields in the accelerating structure.

CHAPTER 5

Conclusions

The plasma wakefield accelerator may one day be used as the primary method for accelerating a particle beam or to augment an existing particle accelerator that uses RF cavities. The primary advantage of the plasma wakefield is its very high accelerating gradient, which can reach tens of GeVs at a modest density of 10^{17} cm^{-3}. In order for plasma wakefield technology to be seriously considered as a replacement or augmentation to current technologies, various capabilities of this technology have to be experimentally demonstrated.

The experiments reported in this thesis explored several of the issues connected to the plasma wakefield through experiments and simulations. The experiments performed at the FACET facility at the SLAC National Accelerator Laboratory used the 20.35 GeV electron beam produced by a 2 km Linac as a driver for the wakefield accelerator. The supporting simulations were performed using the Hoffman cluster and the OSIRIS Particle in Cell code.

The primary focus of this thesis has been on the process of ionization injection and how this process can play various roles in a PWFA. In Chapter 2, the results of ionization injection occurring in a distributed fashion over the length of the plasma was examined. The plasma wakefield was supported by the Rb electrons that were ionized early in the frame of the beam. Throughout the length of the plasma the electron beam's envelope oscillated in the ion column, where upon pinching, the enhanced electric field was able to ionize Rb^{1+}. Such electrons ionized inside the wake were thereafter injected into the plasma wakefield and reduced its accelerating field. The cumulative effect of such electron injection over the length of the plasma was measured by the ratio of energy gain to energy loss. The simulations showed that such distributed injection can reduce the accelerating field to about half of its unloaded value.

In Chapter 3, a lithium plasma was used, and therefore the injection of helium electrons was confined to the ramp of the lithium oven (as opposed to distributed injection over the length of the oven). This confinement is the result of Li^{1+} having an extremely high ionization threshold, which simply cannot be attained by the parameters used in the experiment. The results showed that indeed the ionization injection of helium in the plasma wake can result in formation of a separate beam that can be accelerated to over 30 GeV of energy. It was furthermore shown that the injected beam could be removed by preionization of the helium/lithium region, furthermore producing confidence in the fact that the secondary beam is made of helium electrons as opposed to background plasma electrons. The helium electron beam was furthermore found to maintain an emittance that is over an order of magnitude smaller than the initial drive beam over the process of acceleration.

Finally, it was shown through simulation in Chapter 4 that by confining the injection range to only a single oscillation cycle, it is possible to generate an electron beam with over a 100 pC in charge, over 10 kA in current and with an energy spread that can approach one percent level. Furthermore in this work, the implications of scaling the density by five folds and reducing the plasma column below the radius of the blowout were investigated. The resulting simulations showed that even in the case of a plasma column that was merely on the order of the blowout radius, the ionization injection can be used to ionize and inject helium impurity beams. It furthermore showed that the narrow plasma column does not result in injection of background plasma electrons into the wake, making it a very robust process for generated injected electron beams.

Through this body of work, it was shown that ionization injection through pinching of a high current drive beam is a promising candidate for producing an electron beam with high current, low energy spread, and low emittance in the blowout regime. Furthermore, if enough control and diagnostics exist in the experiment to measure quantities like it is possible in the simulations, one has a number of variables to optimize the qualities of the resulting electron beam. A natural next step is the experimental realization of conditions described in Chapter 4 in order to experimentally demonstrate the high energy, high brightness beam that may

be able to compete with those produced by conventional accelerators in energy as well as beam quality.

APPENDIX A

Plasma Sources for PWFA

The ionization of various elements and molecules such as lithium, xenon, and nitric oxide using the electric field of an electron beam were investigated in reference [11] at the Final Focus Test Beam (FFTB) facility, which was in operation at the SLAC National Accelerator Laboratory. It was found that the ADK model [66] was in agreement with experimental measurements, and therefore, this model, which will be described later, is extensively used in this thesis to estimate ionization of various elements.

Long and uniform-density gas columns that are comprised of an alkali metal like lithium are generated in a heat pipe oven [75, 58], and since such vapor sources are used for plasma production during the experimental portion of this thesis, it will be described here in some detail. This device, schematically shown in Fig. A.1, is used for its ability to create long vapor columns with uniform density profiles. The operation of the heat pipe oven is as follows: A heat pipe oven consists of a closed loop system. A portion of the volume of this close loop is made of high-temperature steel tube that is heated to up to 1000° C. The heated region is terminated by water jackets to rapidly cool the vapor to room temperature. Initially, the entire system is filled with a buffer gas (a noble gas, helium in the case of the lithium oven) to a predetermined pressure. A heater surrounding the steel tube melts the alkali metal (e.g. lithium), creating a vapor pressure that pushes out the buffer gas from the central region of the oven to maintain a pressure equilibrium in the entire system. The vapor condenses in the helium-lithium boundary region near the water jackets by collisions between the helium and the lithium atoms and is then transferred back to the hot center of the oven by a molybdenum mesh that acts as a wick.

Figure A.2 shows experimental measurement of the temperature profiles of the lithium

Figure A.1: (a) Schematics of a lithium vapor heat pipe oven. The important components are marked on the schematic. (b) The lithium oven seen from the side, with hot lithium inside at $\sim 1000^{\circ}$ C. (c) Image of the lithium oven as installed in the experimental area at FACET

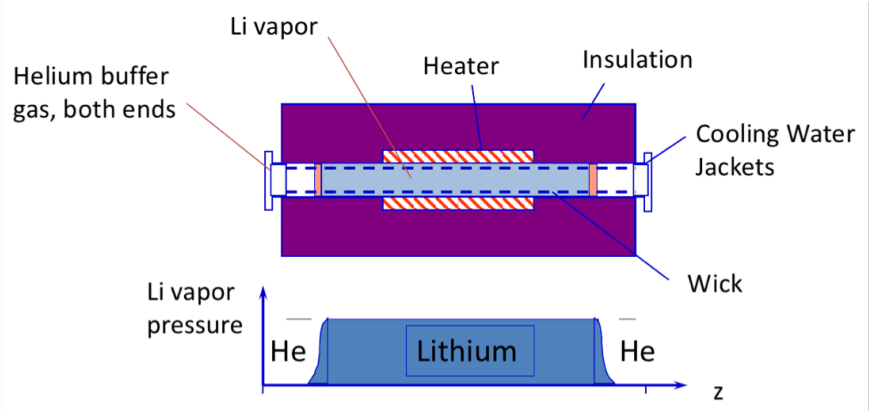

ovens that were used for the experiments reported in chapter 3 (on the left) and the corresponding density profile (on the right). The temperature is measured using a thermocouple, and it is converted to vapor pressure through [76]

$$P_v(\mathrm{Li}) = \frac{1}{133 \times 10^6} \left[\exp(-2.0532\ \ln(T) - 19.4268/T + 9.4993 + 0.753\ T)\right] \tag{A.1}$$

for lithium vapor and through

$$\begin{aligned} P_v(\mathrm{Rb}) =& \frac{1}{133 \times 10^6}[\exp(-0.9148\ \ln(T) - 9.8420/T + 8.5965 - 1.6227 \times T + \\ & 1.2416(T)^2 - 0.2943. * (T)^3 - 0.0055. * (T)^4 + 0.0042. * (T)^5)]. \end{aligned} \tag{A.2}$$

for the rubidium vapor. Here, T is the temperature in kilo Kelvin and P_v is the pressure in Torr. A similar equation for other alkali vapors can be found in [76]. The high thermal conductivity of the alkali vapor ensures that the temperature of the oven is uniform in the central region, which results in nearly a uniform density. With temperature and pressure determined, the neutral density is calculated using the ideal gas law, $n_0[\mathrm{cm}^{-3}] = 9.66 \times 10^{18} \times P_v./(T * 1000)$. The density of the helium shown in Fig. A.2 is calculated using the principle of pressure balance at equilibrium (i.e. total pressure at each point equals the backing pressure of cold helium). It is important to note that the density of helium falls as the density of lithium rises, and that in the central regions there are almost no helium atoms.

The rubidium oven was constructed in a similar way to a lithium oven, except that the gas argon was used instead of helium as a buffer gas due to a concern that the much lighter helium may not be able to contain rubidium. The density profile of rubidium vapor is shown in Fig. A.3.

The alkali metal vapor plasmas were successfully used for all the experimental campaigns at the FFTB and FACET. In the early days at the FFTB, columns of plasmas were created by single photon ionization of the Li using a nanosecond long ArF laser pulse. But the plasmas were weakly ionized and low density. Later, when the electron beam was compressed to sub 100 fs, we used field ionization by the particles in the head of the beam to produce mostly singly ionized dense plasma columns. However, the distance over which the wake could

Figure A.2: (a) Measured temperature profile of a 30 cm lithium heat pipe oven. (b) Corresponding lithium and helium density. (c) Measurement of temperature profile of a 130 cm lithium oven. The x axis indicates the distance from the center of the oven. (d) Lithium and helium density corresponding to profile in (c)

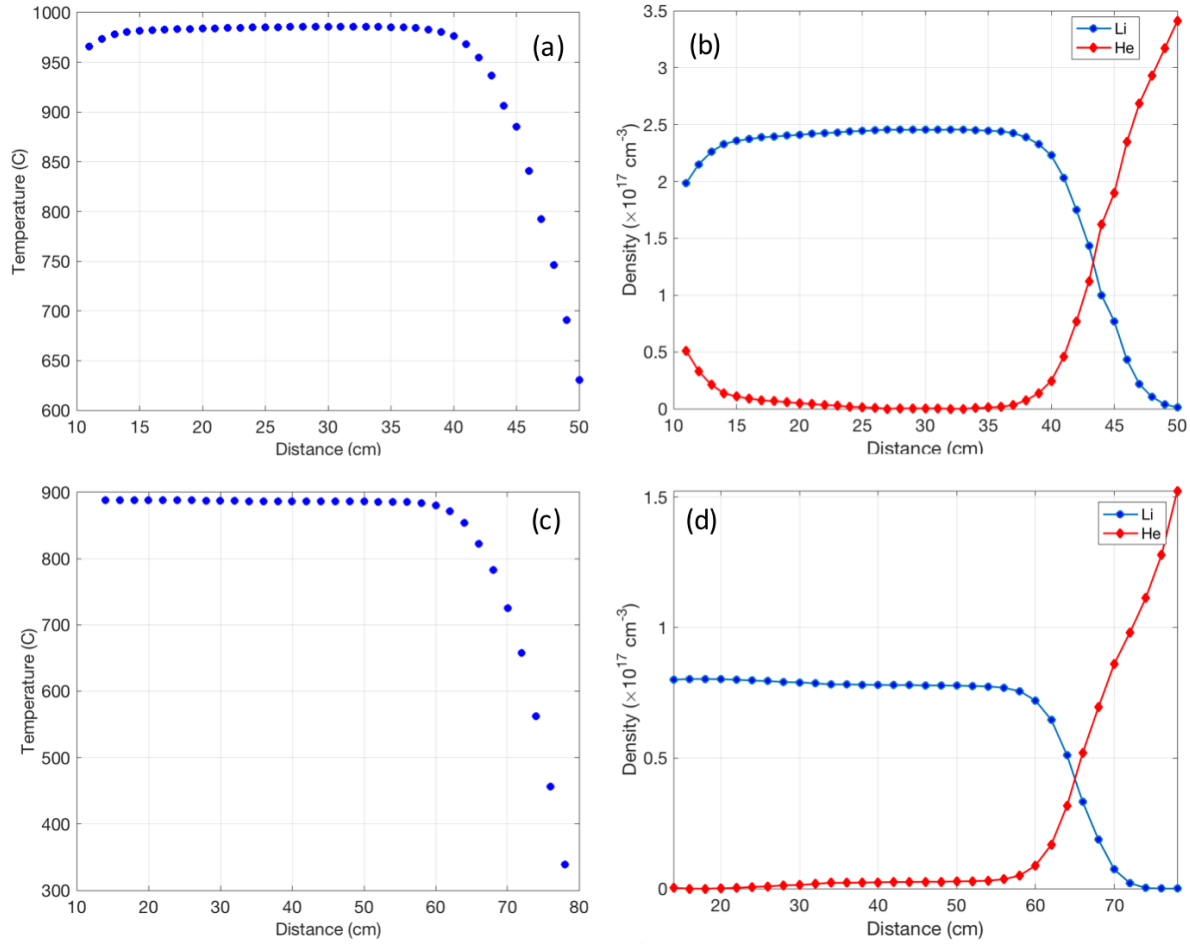

Figure A.3: (a) Temperature measurement using a thermocouple for the rubidium oven. (b) Calculated rubidium and argon densities

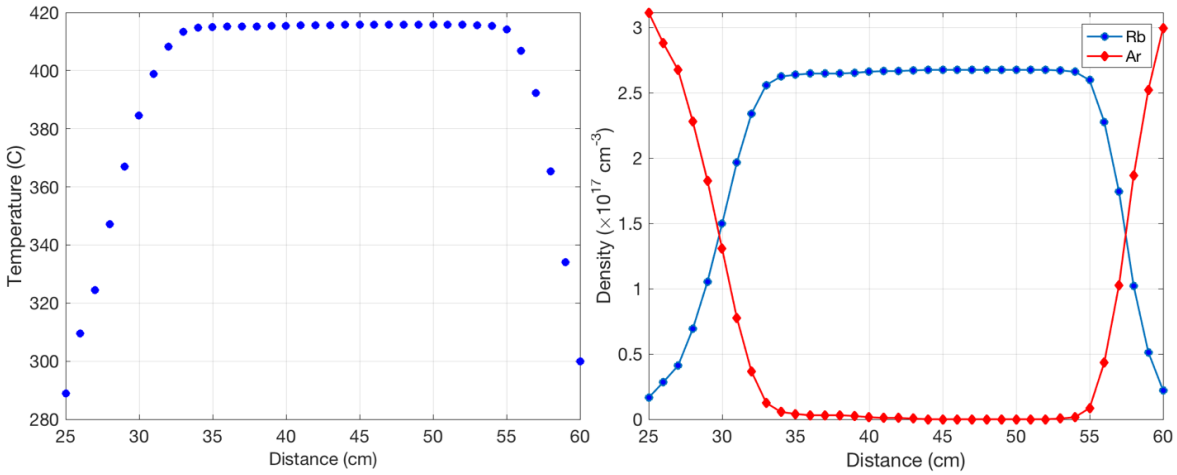

be excited was limited by beam head erosion as described earlier. We needed a method to produce meter scale fully ionized high density plasmas in not only alkali vapors but in hydrogen as well. A method to generate pre-ionized plasma using a laser will be described in this thesis in chapter 3. This technique involves the use of a specialized optic called an axicon, which creates a Bessel radial profile for the laser intensity that is stationary over a length that can span meters. This source was used to preionize the 130 cm Lithium plasma before the arrival of the electron beam. The downside of this plasma source is that the Bessel profile is typically on the order of 100 microns wide (i.e. $\sim 3\sigma_r$). However, the peak intensity of the Bessel profile was over 100x higher then the ionization threshold of lithium, and indeed it was used to even ionize helium (see chapter 3). In other words, the intensity was so high that the ionization threshold was exceeded over many rings of the Bessel profile and therefore wide plasma was generated such that the electron beam overlapped with the plasma regardless of the laser's pointing jitter.

This Bessel profile made by an axicon focused laser was also investigated for producing pre-ionized plasma in a column of hydrogen. In this instance, the peak of the intensity profile was only about 10x higher than the ionization threshold for hydrogen. Therefore, only the first ring of the Bessel profile was able to ionize hydrogen, and the first ring was

only $\sim$ $3\sigma_r$ as stated above. An additional problem was that the pointing jitter of the laser was also on the same order, making it impossible to get perfect alignment between the laser and electron beam propagation vectors. The small width of the plasma together with the pointing jitter of the laser meant that the overlap between the electron beam and the preionized plasma was smaller than the entire length of the preionized plasma. This lead to a situation where the electron beam interacted with the edge of the plasma, making the physics and the results difficult to interpret. For this reason, the results of the interaction of electron beam with this plasma require further analysis and therefore are excluded from this thesis. Although a variety of axicons, including a variant known as axilens, which has the ability to create a predefined longitudinal profile, were tried, they were not successful in making stable and reliable pre ionized plasma. Thus the generation of stable, meter scale plasmas in room temperature neutral gases such as hydrogen remains an open problem.

APPENDIX B

Distributed Beam Loading Supplement

B.1 Betatron oscillation of beam in various foil conditions

As it was stated in the text the higher emittance and spot size resulted from the insertion of the foils leads to larger amplitude betatron oscillations, but the minimum of the oscillation remains fairly constant. The effect of variation in σ_r is illustrated in Fig. B.1. Here, σ_r is increased from 35 μm in (a), to 60 μm in (b). It is clearly seen that the peak amplitude is increased from 10 μ m-20 μ m, while the minimum stays around 2 μm.

Figure B.1: The effect of betatron σ_r on the betatron oscillations. (a) Betatron oscillations for a beam with $\epsilon_n = 250$ mm-mrad, and $\sigma_r = 35$ μm, same as Fig. 2.3. (b) Betatron oscillations for a beam with $\epsilon_n = 250$ mm-mrad, and $\sigma_r = 60$ μm

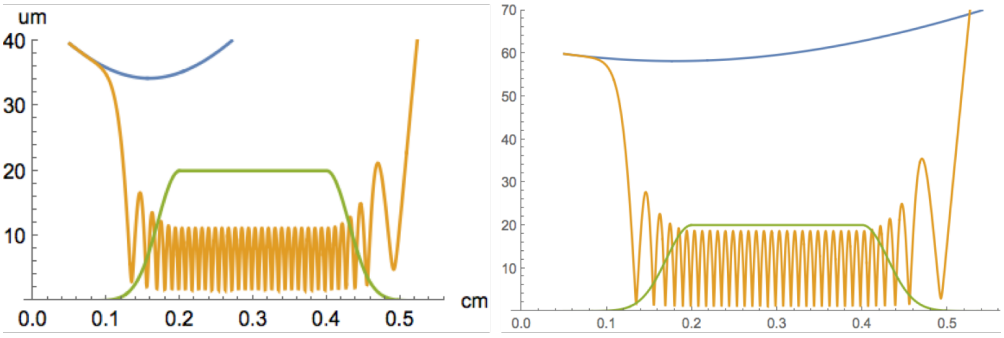

(a) (b)

APPENDIX C

Revisiting Emittance Measurement in the Experiment

C.1 Introduction

Since the measurement of emittance is central to the results of of the Chapter 3, it is important to describe the diagnostic used for emittance measurement in some detail. Additionally, the measurement shown in Chapter 3 did not take the presence of scattering foils or the downramp of plasma into account. These effects are modelled in the measurements in this chapter. The emittance for a collection of electrons is calculated using

$$\epsilon^2 =< x^2 >< x'^2 > - < xx' >^2, \tag{C.1}$$

where x is the position of an electron in the transverse coordinate of interest and $x' = p_x/p_z$ is the angle of the same electron. The brackets represent the moments of the particle distribution function in the phase space, $\psi(x, x')$, e.g.

$$< x^2 >= \int dxdx'(x- < x >)^2\psi(x, x'). \tag{C.2}$$

Therefore, to measure the emittance, it is important to measure these second order moments of the distribution function. For a Gaussian beam, that is, for a beam with Gaussian distributions in x and x', the second order moments can be described in terms of the Courant-Snyder parameters (see Fig. C.1[77]).

$$< x^2 >= \beta\epsilon \tag{C.3}$$

$$< xx' >= -\alpha\epsilon \tag{C.4}$$

$$< x'^2 >= \gamma\epsilon \tag{C.5}$$

Figure C.1: The phase space and the corresponding Courant-Snyder parameters of an electron beam with Gaussian distributions. Here, the transverse coordinate of interest is on the x axis and the corresponding divergence $x' = p_x/p_z$ is the y axis.

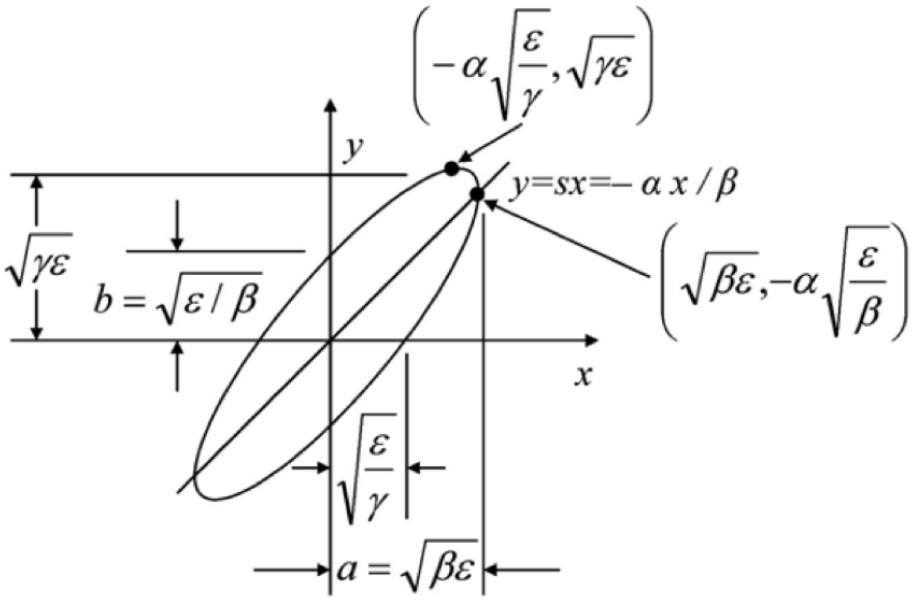

Before explaining the measurement technique for emittance, it is helpful to provide an intuitive sense of how the Courant-Snyder parameters relate to the properties of the electron beam. To start with, the parameter emittance (ϵ) is the area of the phase space ellipse in Fig. C.1. Therefore, the larger the emittance, the larger the area of this ellipse. Because this property is conserved in propagation through focusing elements, it determines the focusability of the electron beam, i.e. the smaller the emittance, the easier it is to focus the electron beam.

The parameter β together with ϵ determine the transverse size σ_x at any point through $\sigma_x = \sqrt{\beta\epsilon}$ as shown in Fig. C.1. α is related to the orientation of the ellipse in Fig. C.1, such that when $\alpha = 0$, the ellipse is vertical and the electron beam has its lowest transverse size (it is at its waist). The variable $\gamma = (1 + \alpha^2)/\beta$ is related to the divergence of the beam through $\sigma_{x'} = \gamma\epsilon$. Together, these four parameters (α, β, γ, and ϵ) determine the size, divergence, and area of the phase space for the electron beam at each position, completely describing the electron beam.

Name	z (m)
Edge of the plasma ramp	1994.78
75 μm Be window	1996.34
QS 1	1999.21
QS 2	2004.21
5 mm Al window	2015.16
Lanex	2015.22
Cherenkov	2016.04

Table C.1: Name and location of the important points using the LINAC coordinates in meters. The P_{ext} refers to the plasma exit location, taken as half way down the downramp. QS 1 and QS 2 are the two quadrupole magnets used in the spectrometer. The distances shown indicate the middle of the magnets. The effective length of the magnets is 1 m. Lanex is the Lanex screen indicated in the text, and is used for emittance measurement, and Cherenkov is the the location of the Charenkov detection plane.

The three moments of the distribution function that result in emittance would ideally be obtained from three different measurements, such as the beam size at three different dipole strengths, or at three different locations in z. Because of the shot-to-shot variability of the results in the experiment described in Chapter 3 however, a single-shot measurement based on the variation of the beam size as a function of energy on the electron spectrum is used to infer emittance.

This spectrum was obtained using a LANEX film, which was positioned upstream of the Cherenkov spectrometer and very near the exit window of the vacuum (see Table C.1 for the position of the detectors and emittance changing elements in terms of linac coordinates). Unlike the spectra produced by the Cherenkov light, which was produced through 5 cm of radiation and therefore had some blurring associated with it, the spectra observed with LANEX film was recorded as a phosphorescence of the film material as electrons traversed it at a single point along their propagation. The spectrum on LANEX therefore produces an image with better spatial quality than the Cherenkov detector.

The variation of the electron-beam-width as a function of the energy on the LANEX screen, i.e. $\sigma_{r,i}(E)$ then is used to infer emittance. An optimization routine in MATLAB is used to initialize the electron beam parameters (α, β, and ϵ) on the up-ramp of the plasma and then these variables are propagated through various elements to the detection screen. Because the precise shape of the down-ramp of the plasma is not known, the distance between the end of the down-ramp and the Be window is also used as a free parameter to provide a match. The location of down-ramp has to be limited within reasonable experimental range,

A fundamental assumption in this calculation is that the (α, β, γ, ϵ) parameters of the beam over the range of energy that is analyzed is constant, and the variation of σ_r is almost entirely due to the variation in electron energy. Because the energy gain in this experiment is 24 GeV, and the range of energies analyzed is less than 2 GeV, the beam parameters are likely the same with a very good approximation.

C.2 Modeling Electron Beam Propagation To Detection Plane

The evolution of Courant-Snyder parameters through focusing elements can be derived using the relevant transport matrices R. Given a transport matrix $R = \begin{bmatrix} C & S \\ C' & S' \end{bmatrix}$, where $\begin{bmatrix} x_f \\ x'_f \end{bmatrix} = R \begin{bmatrix} x_i \\ x'_i \end{bmatrix}$, we have

$$\begin{bmatrix} \beta_f \\ \alpha_f \\ \gamma_f \end{bmatrix} = \begin{bmatrix} C^2 & -2CS & S^2 \\ -CC' & CS' + SC' & -SS' \\ C'^2 & -2C'S' & S'^2 \end{bmatrix} \begin{bmatrix} \beta_i \\ \alpha_i \\ \gamma_i \end{bmatrix}. \tag{C.6}$$

The subscripts i indicates the parameters before the focusing element, and the subscript f indicates the parameters after the focusing element. As an example, in the case of free

propagation in space for a distance L, $R = \begin{bmatrix} 1 & L \\ 0 & 1 \end{bmatrix}$, and therefore,

$$\begin{bmatrix} \beta_f \\ \alpha_f \\ \gamma_f \end{bmatrix} = \begin{bmatrix} 1 & -2L & L^2 \\ 0 & 1 & -L \\ 0 & 0 & 1 \end{bmatrix} \begin{bmatrix} \beta_i \\ \alpha_i \\ \gamma_i \end{bmatrix}, \tag{C.7}$$

The plasma's ion column produces a linear focusing force as described in Chapter 1. The propagation of the electron beam through this continuous focusing element is modeled with the transport matrix

$$R_{\text{ramp}} = \begin{bmatrix} \cos(kdz) & \frac{1}{k}\sin(kdz) \\ -k\sin(kdz) & cos(kdz) \end{bmatrix}, \tag{C.8}$$

where $k = k_\beta = \frac{\omega_p}{c\sqrt{2\gamma_b}}$, and γ_b is the relativistic Lorentz factor. As the plasma density in the ramp decreases, so does the plasma frequency and the focusing force.

The transport matrix for the two quadrupoles QS1 (focusing element) and QS2 (defocusing element) can be expressed as

$$R_{Q1} = \begin{bmatrix} \cos\left(L\sqrt{k}\right) & \frac{1}{\sqrt{k}}\sin\left(L\sqrt{k}\right) \\ -\sqrt{k}\sin\left(L\sqrt{k}\right) & \cos\left(L\sqrt{k}\right) \end{bmatrix}, \tag{C.9}$$

$$R_{Q2} = \begin{bmatrix} \cosh\left(L\sqrt{k}\right) & \frac{1}{\sqrt{k}}\sinh\left(L\sqrt{k}\right) \\ -\sqrt{k}\sinh\left(L\sqrt{k}\right) & \cosh\left(L\sqrt{k}\right) \end{bmatrix}. \tag{C.10}$$

Because the QS2 is a defocusing element, the elements are expressed as hyperbolic trigonometric function as opposed to ordinary trigonometric functions for QS1. In both cases, k is the design normalized quadrupole strength in m^{-2}, and L is the effective length of the magnets, which is one meter for both magnets. The quadrupole strength is calculated using a thin lens approximation, $k = 1/\sqrt{Lf}$, where f is the focal length of the magnets. The focal length of the magnets can be calculated from the magnet strength, which is recorded for each dataset. For the dataset analyzed here, $f_1 = 2.7$ m and $f_1 = 4.0$ m at 24 GeV for QS1 and QS2, respectively. Using the transport matrices presented and Eq. C.6, the evolution of the Courant-Snyder parameters is modeled through the elements of the experiment.

Finally, the effect of the scattering foils on emittance is explained in section 2.4 and is calculated using Eq. 2.13, i.e.

$$\epsilon_f = \sqrt{\epsilon_i(\epsilon_i + \beta_i \Delta\theta^2)}, \tag{C.11}$$

$$\beta_f = \beta_i \epsilon_i / \sqrt{\epsilon_i(\epsilon_i + \beta_i \Delta\theta^2)}, \tag{C.12}$$

$$\alpha_f = \alpha_i \epsilon_i / \sqrt{\epsilon_i(\epsilon_i + \beta_i \Delta\theta^2)}. \tag{C.13}$$

γ is calculated using $\gamma = (1 + \alpha^2)/\beta$. At 24 GeV, the multiple scattering angle for the 75 μm Be window is 8.3 μrad and for the 5 mm Al window, it is 134 μrad. These values are calculated by Moliere scattering theory [59],

$$\Delta\theta = \frac{13.6 \text{ MeV}}{\beta_b c p} z \sqrt{x/X_0} \left[1 + 0.038 \ln(x/X0)\right], \tag{C.14}$$

where $\beta_b c$ is the velocity of the particle, p is the momentum, z is the charge number, x is the material thickness and X_0 is the radiation length. Thus given the initial conditions of the beam inside the plasma, the values of $\sigma_r(E)$ can be calculated for any electrons with energy E.

C.3 Measuring Beam Width and Estimating Emittance

The first step in estimating the beam emittance is to construct the $\sigma_r(E)$ curve. This is done by choosing the interval on the LANEX screen that is used to measure the data (spanning about 2 GeV), and choosing periodic lines of 6 pixels wide, integrating the counts verically, and then fitting a double Gaussian to the resulting lineout. The double Gaussian is necessary because the injected electrons gaining 24 GeV are overlaid on the drive beam electrons that gained only 4 GeV. However, the divergence of the drive beam electrons is very high and around the focus of the spectrometer, they represent only a wide background. Therefore, a double Gaussian fitting returns two parameters, the larger gaussian width belongs to the wide background (drive beam electrons) and the narrower Gaussian width to the injected charge. An example of such a fit is shown in Fig.C.2(a), where the $\sigma_r^{\text{fit}} = 97.3$ μm for the injected charge. This is from a case, which in Fig. 3.7(b) belongs to center of distribution ($\sim$ 30 mm-mrad).

Figure C.2: (a) An example of a double Gaussian fit to the horizontal lineout of a 6-pixel wide slice of the spectrum on LANEX. the image fitted is shown as an inset. The black lines indicate the outer extents of where the fit was performed. (b) $\sigma_r(E)$ for the same data. The value of the third point is obtained from the σ_r fitted to the lineout in (a). The dashed orange line is obtained by an optimization of the electron beam variables inside a plasma, which are then propagated to Lanex screen. Effects of foils and plasma down-ramp are included here

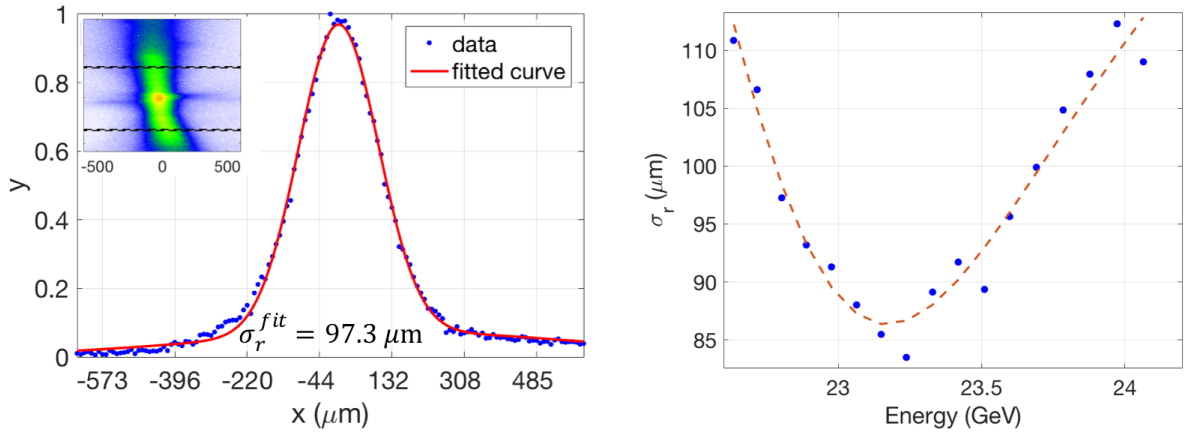

The resulting curve for all slices is shown in Fig. C.2(b). The orange dashed line in the figure shows the result of the optimization routine, which indicates the values inside the plasma. The parameters of the electron beam at the edge of the plasma ramp that are inferred from the optimization routine (orange curve in Fig. C.2(b)) are as follows: $\epsilon_n = 5.4$ mm-mrad, $\sigma_r = 1.1$ μm, $\alpha = -0.29$, D1=134.6 cm. D1 is the distance between the end of the plasma region and the Be window. The plasma region and σ_r evolution are shown in Fig. C.3. The edge of the plasma is at 1 cm in this figure. We can check this number with the linac coordinates in Table C.1 to see if the location of Be window is calculated correctly by the fit. Here, the location of Be window is found by adding the length of plasma region (0.20 m) and D1 (1.34 m) to the linac location of edge of the plasma ramp (1994.78 m), $1994.78 + 0.20 + 1.34 + = 1996.33$, which coincides within a centimeter of the measured location of Be window. Given the fit optimizes propagation of beam parameters over 10 m, this accuracy is very good.

Using the equivalent calculation of Chapter 3, where the effect of the ramp and the foils are not taken into account, the optimization routine returns these initial condition parameters (ϵ_n [mm-mrad],σ_r [μm], α) = (30.5, 17, 0.9). The value of 30.5 mm-mrad places this shot in the middle of the distribution in Fig. 3.7(b). If the effect of the foil, but not the ramp is considered, the optimized initial conditions are (ϵ_n [mm-mrad],σ_r [μm], α) = (7.5, 11, 3.47). In other words, where the initial emittance is very low, the measured beam emittance is dominated by the contribution of the foils in the beam path, and the contributions of the down-ramp are much less prominent.

C.3.1 Emittance of the Drive Beam

The emittance of the drive beam can also be measured with the same techniques. For instance, the Cherenkov diagnostic is used here to measure the emittance of the drive beam in Fig. 3.6(b). The Cherenkov spectrometer has a resolution of $\sigma_x \sim 350$ μm [72], which is subtracted in quadrature from σ_x at every energy. The same optimization routine using the plasma down-ramp and Be and Al form indicates that the emittance of drive beam before

Figure C.3: The downramp modeled after the real plasma downramp shown in blue. In orange, there is the evolution of σ_r as a function of distance.

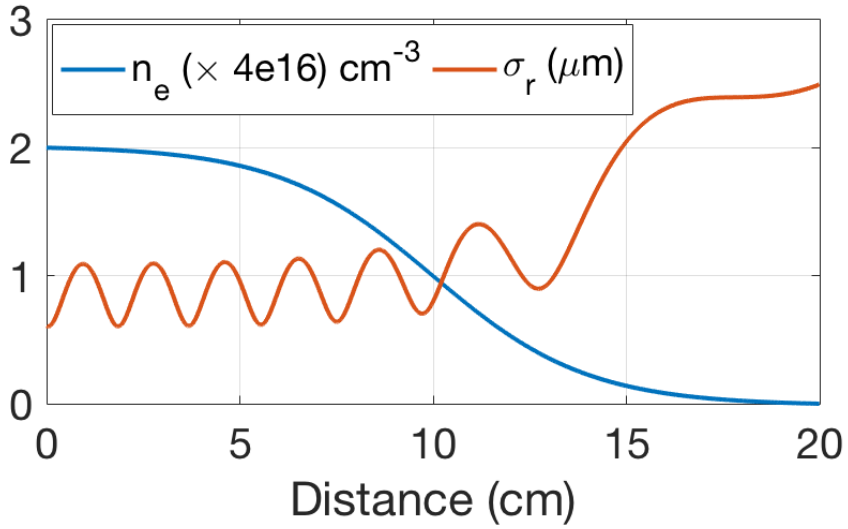

the down-ramp of the plasma is 731 mm-mrad (see Fig. C.4). Additionally, the optimization routine indicates that $\sigma_r \sim 11$ μm and $\alpha = 0.4303$ at the same point inside the plasma.

If the optimization is done instead without the use of the foils, but with the effect of the ramp taken into account, (ϵ_n [mm-mrad],σ_r [μm], α) = (749, 11, 0.4181). In this case, because of the initially large emittance of the drive beam, the additional effect of the foils are fairly minor. On the other hand, if the plasma ramp is removed from the optimization routine, the optimized parameters become (ϵ_n [mm-mrad],σ_r [μm], α) = (1629, 119, 1.88). In other words, the presence of the ramp makes about a 2x contribution to the measurement of the emittance of the drive beam electrons. This is because the down-ramp acts as a third-lens, and in effect modifies the "object" size and divergence as seen from the QS1-QS2 optical system.

If the effects of the foils and ramps are both removed, as was the case in calculations shown in Chapter 3, (ϵ_n [mm-mrad],σ_r [μm], α) = (1732, 121, 1.77). Once again, the removal of the foils has some effect on the measurement, but only accounts for about 6% of calculated value.

The emittance value of the portion of the drive beam that loses energy can also be

Figure C.4: Measuring the emittance of the electron beam. (a) Same as Fig. 3.6(b), zoomed in the region of interest. (b) σ_r plotted for various energies (blue filled circles) along with the spectra resulting from the optimization of electron beam parameters (ϵ_n,σ_r, and α) inside the plasma. The effects of the plasma down ramps, and the Be and Al foils are modeled as described above along with the effect of the quadrupoles

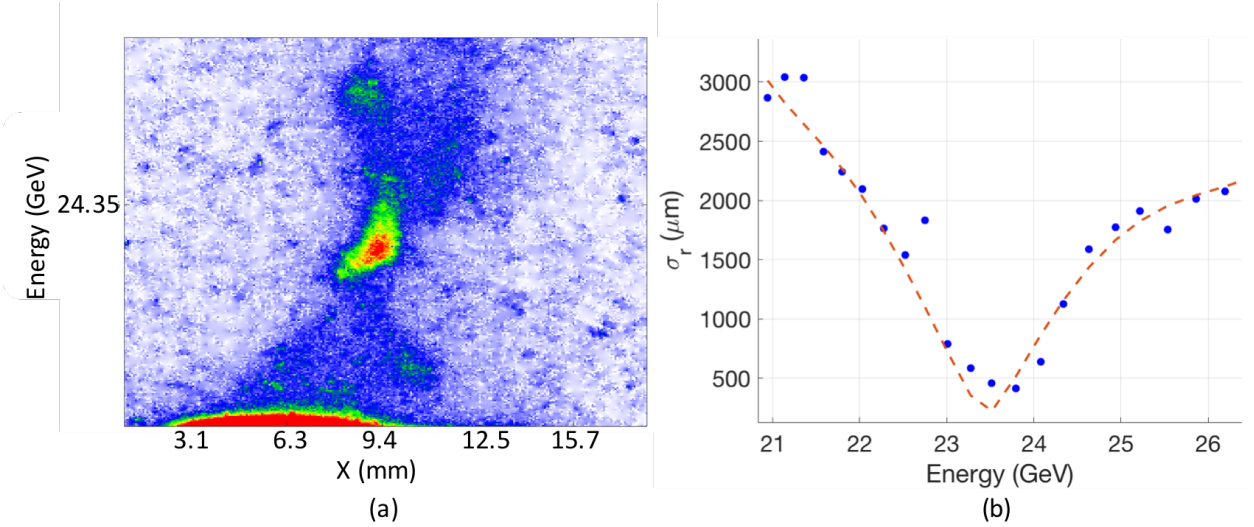

estimated using this analysis. For this measurement however, it is important to choose a set of data where the injected beam does not overlap with the drive beam electrons. Therefore, the measurement of the emittance of the drive beam were performed for a two-bunch dataset (E200_13054) with the plasma density at 3×10^{16} (see Fig. C.5(a)). Once again, double Gaussian fits are used to determine the smaller σ_r of two possible values for a fit at each energy on the Cherenkov detector. In this instance, the double Gaussian fit is necessary because the energy loss of a PWFA is double-valued. Therefore, the narrower, lower emittance part of the energy loss – attributed to the back portion of the beam in the blowout regime – is overlapped with the front portion of the beam, which loses the same amount of energy, but is not necessary in the blowout region, and as a result has a larger emittance. The optimized initial values without taking the effect of the ramp or the foils into account are (ϵ_n [mm-mrad],σ_r [μm], α) = (683, 66, 0.06). Once the effect of the foils are included, the initial conditions become (ϵ_n [mm-mrad],σ_r [μm], α) = (584, 56, 0.06). The resulting curve for the latter calculation is shown in Fig. C.5.

Figure C.5: Measuring the emittance of the drive beam electrons that lost energy. (a) Raw image. Color table enhanced to improve the visibility of pinch region at $\sim$ 14.35 GeV. the black dotted lines indicate the outer extents of where the fits to the lineouts were performed (b) σ_r plotted for various energies (blue filled circles) along with the spectra resulting from the optimization of electron beam parameters (ϵ_n,σ_r, and α)=(584, 56, 0.06) inside the plasma. The effects of the Be and Al foils are modeled as described above along with the effect of the quadrupoles, but not the plasma ramp

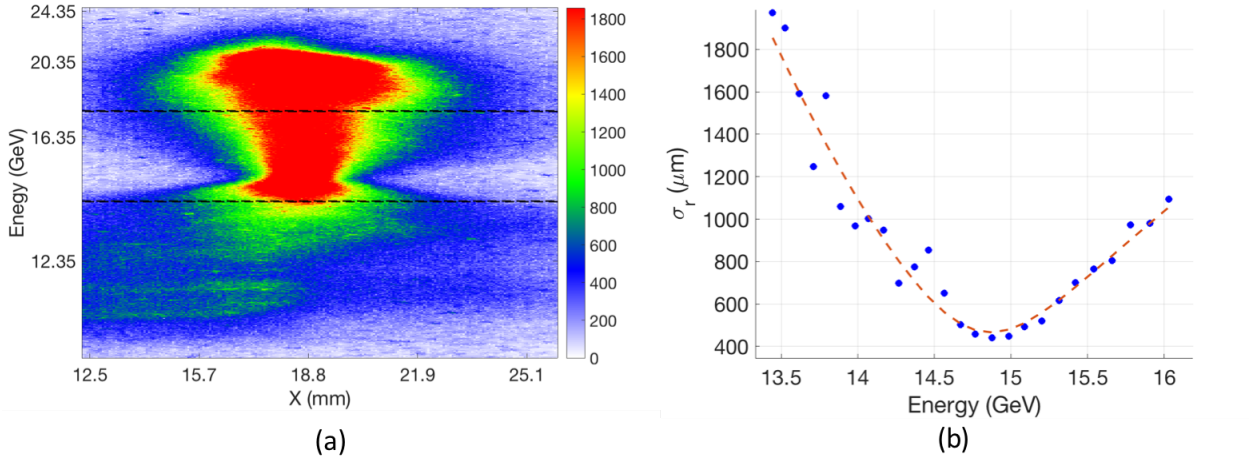

The conditions of ramp in this case are not well known for two reasons: In the case where the laser and axicon are used to preionize the plasma, as is the case in Fig. C.5, the laser intensity is high enough to ionize the down-ramp helium. This results in a modification of the plasma density that is not measured, and depending on the alignment of the laser can have complicated characteristics. On the other hand, in the self-ionized case, the current of the drive beam is much lower than the current of the single bunch electron beam, resulting in head erosion, and therefore the beam likely does not make it to the end of the 130 cm. As previously mentioned, the plasma down-ramp can reduce the measured emittance by about a factor of 2, meaning that the emittance of the drive beam inside the plasma is likely between 200 and 300 mm-mrad.

In summary, the optimization of beam parameters using the features of the spectrometer allow for calculation of the emittance for an electron beam, assuming that the various energies

have equivalent beam parameters except for energy. This method will provide an upper-bound estimate on the emittance, and a more accurate model will be needed to be developed to estimate the emittance of the beam with accuracy.

References

[1] G. Aad et al. Observation of a new particle in the search for the Standard Model Higgs boson with the ATLAS detector at the LHC. *Physics Letters, Section B: Nuclear, Elementary Particle and High-Energy Physics*, 716(1):1–29, 2012.

[2] S. Chatrchyan et al. Observation of a new boson at a mass of 125 GeV with the CMS experiment at the LHC. *Physics Letters, Section B: Nuclear, Elementary Particle and High-Energy Physics*, 716(1):30–61, 2012.

[3] T. Tajima and J. Dawson. Laser Electron Accelerator. *Physical Review Letters*, 43(4):267–270, 1979.

[4] P. Chen, J. Dawson, R. Huff, and T. Katsouleas. Acceleration of Electrons by the Interaction of a Bunched Electron Beam with a Plasma. *Physical Review Letters*, 54(7):693–696, 1985.

[5] A. M. Pukhov and J. Meyer-ter Vehn. Laser wake field acceleration : the highly nonlinear broken-wave regime. *Applied Physics B*, 74:355–361, 2002.

[6] W. Lu, C. Huang, M. Zhou, M. Tzoufras, F. S. Tsung, W. B. Mori, and T. Katsouleas. A nonlinear theory for multidimensional relativistic plasma wave wakefields. *Physics of Plasmas*, 13(5):056709, 2006.

[7] W. Lu, C. Huang, M. Zhou, W. B. Mori, and T. Katsouleas. Nonlinear Theory for Relativistic Plasma Wakefields in the Blowout Regime. *Physical Review Letters*, 96(16):165002, 2006.

[8] W. P. Leemans, A. J. Gonsalves, H.-S. Mao, K. Nakamura, C. Benedetti, C. B. Schroeder, Cs. Tóth, J. Daniels, D. E. Mittelberger, S. S. Bulanov, J.-L. Vay, C. G. R. Geddes, and E. Esarey. Multi-GeV Electron Beams from Capillary-Discharge-Guided Subpetawatt Laser Pulses in the Self-Trapping Regime. *Physical Review Letters*, 113(24):245002, 2014.

[9] X. Wang, R. Zgadzaj, N. Fazel, Z. Li, S. a. Yi, X. Zhang, W. Henderson, Y.-Y. Chang, R. Korzekwa, H.-E. Tsai, C.-H. Pai, H. Quevedo, G. Dyer, E. Gaul, M. Martinez, A. C. Bernstein, T. Borger, M. Spinks, M. Donovan, V. Khudik, G. Shvets, T. Ditmire, and M. C. Downer. Quasi-monoenergetic laser-plasma acceleration of electrons to 2GeV. *Nature Communications*, 4, 2013.

[10] W. Lu, M. Tzoufras, C. Joshi, F. S. Tsung, W. B. Mori, J. M. Vieira, R. A. Fonseca, and L. O. Silva. Generating multi-GeV electron bunches using single stage laser wakefield acceleration in a 3D nonlinear regime. *Physical Review Special Topics- Accelerators and Beams*, 10:061301, 2007.

[11] C. O'Connell, C. Barnes, F.-J. Decker, M. Hogan, R. Iverson, P. Krejcik, R. Siemann, D. Walz, C. Clayton, C. Huang, D. Johnson, C. Joshi, W. Lu, K. Marsh, W. Mori,

M. Zhou, S. Deng, T. Katsouleas, P. Muggli, and E. Oz. Plasma production via field ionization. *Physical Review Special Topics - Accelerators and Beams*, 9(10):101301, 2006.

[12] B. Hidding, G. Pretzler, J. B. Rosenzweig, T. Königstein, D. Schiller, and D. L. Bruhwiler. Ultracold Electron Bunch Generation via Plasma Photocathode Emission and Acceleration in a Beam-Driven Plasma Blowout. *Physical Review Letters*, 108(3):035001, 2012.

[13] F. Li, J. F. Hua, X. L. Xu, C. J. Zhang, L. X. Yan, Y. C. Du, W. H. Huang, H. B. Chen, C. X. Tang, W. Lu, C. Joshi, W. B. Mori, and Y. Q. Gu. Generating High-Brightness Electron Beams via Ionization Injection by Transverse Colliding Lasers in a Plasma-Wakefield Accelerator. *Physical Review Letters*, 111(1):015003, 2013.

[14] X. L. Xu, J. F. Hua, F. Li, C. J. Zhang, L. X. Yan, Y. C. Du, W. H. Huang, H. B. Chen, C. X. Tang, W. Lu, P. Yu, W. An, C. Joshi, and W. B. Mori. Phase-Space Dynamics of Ionization Injection in Plasma-Based Accelerators. *Phys. Rev. Lett.*, 112(3):35003, 2014.

[15] L. L. Yu, E. Esarey, C. B. Schroeder, J. L. Vay, C. Benedetti, C. G R Geddes, M. Chen, and W. P. Leemans. Two-color laser-ionization injection. *Physical Review Letters*, 112(12):1–5, 2013.

[16] T. Katsouleas. Physical mechanisms in the plasma wake-field accelerator. *Physical Review A*, 33(3):2056–2064, 1986.

[17] S. Wilks, T. Katsouleas, J. M. Dawson, P. Chen, and J. J. Su. Beam Loading in Plasma-Waves. *IEEE Transactions on Plasma Science*, 15(2):210–217, 1987.

[18] J. B. Rosenzweig. Nonlinear plasma dynamics in the plasma wake-field accelerator. *Physical Review Letters*, 58(6):555–558, feb 1987.

[19] J. Rosenzweig, B. Breizman, T. Katsouleas, and J. Su. Acceleration and focusing of electrons in two-dimensional nonlinear plasma wake fields. *Physical Review A*, 44(10):R6189–R6192, 1991.

[20] M. Tzoufras, W. Lu, F. Tsung, C. Huang, W. Mori, T. Katsouleas, J. Vieira, R. Fonseca, and L. Silva. Beam Loading in the Nonlinear Regime of Plasma-Based Acceleration. *Physical Review Letters*, 101(14):145002, 2008.

[21] R. A. Fonseca, L. O. Silva, F. S. Tsung, V. K. Decyk, W. Lu, C. Ren, W. B. Mori, S. Deng, S. Lee, T. Katsouleas, and J. C. Adam. OSIRIS: A Three-Dimensional, Fully Relativistic Particle in Cell Code for Modeling Plasma Based Accelerators. In *Lecture Notes in Computer Science*, volume 2331, pages 342–351. 2002.

[22] W. An, V. K. Decyk, W. B. Mori, and T. M. Antonsen. An improved iteration loop for the three dimensional quasi-static particle-in-cell algorithm: QuickPIC. *Journal of Computational Physics*, 250:165–177, 2013.

[23] C. Huang, V. K. Decyk, C. Ren, M. Zhou, W. Lu, W. B. Mori, J. H. Cooley, T. M. Antonsen, and T. Katsouleas. QUICKPIC: A highly efficient particle-in-cell code for modeling wakefield acceleration in plasmas. *Journal of Computational Physics*, 217(2):658–679, 2006.

[24] J. B. Rosenzweig, D. B. Cline, B. Cole, H. Figueroa, W. Gai, R. Konecny, J. Norem, P. Schoessow, and J. Simpson. Experimental Observation of Plasma Wake-Field Acceleration. *Physical Review Letters*, 61(1):98–101, 1988.

[25] J. B. Rosenzweig, P. Schoessow, B. Cole, W. Gai, R. Konecny, J. Norem, and J. Simpson. Experimental measurement of nonlinear plasma wake fields. *Physical Review A*, 39(3):1586–1589, 1989.

[26] J.B. Rosenzweig, P. Schoessow, B. Cole, C. Ho, W. Gai, R. Konecny, S. Mtingwa, J. Norem, M. Rosing, and J. Simpson. Demonstration of Electron Beam Self-Focusing in Plasma Wake Fields. *Physics of Fluids B*, 2(6):1376–1383, 1989.

[27] J. J. Su, T. Katsouleas, J. M. Dawson, and R. Fedele. Plasma lenses for focusing particle beams. *Physical Review A*, 41(6):3321–3331, 1990.

[28] H. Nakanishi, Y. Yoshida, T. Ueda, T. Kozawa, H. Shibata, K. Nakajima, T. Kurihara, N. Yugami, Y. Nishida, T. Kobayashi, A. Enomoto, T. Oogoe, H. Kobayashi, B. S. Newberger, S. Tagawa, K. Miya, and A. Ogata. Direct observation of plasma-lens effect. *Physical Review Letters*, 66(14):1870–1873, 1991.

[29] G. Hairapetian, P. Davis, C. E. Clayton, C. Joshi, S. C. Hartman, C. Pellegrini, and T. Katsouleas. Experimental demonstration of dynamic focusing of a relativistic electron bunch by an overdense plasma lens. *Physical Review Letters*, 72(15):2403–2406, 1994.

[30] P. Chen, D. Cline, W. Craddock, F. J. Decker, R. Iverson, T. Katsouleas, P. Kwok, W. Leemans, S. Masuda, D. D. Meyerhofer, K. Nakajima, A. Ogata, P. Raimondi, A. Sessler, D. Walz, and A. Weidemann. Plasma lens experiment at the final focus test beam. *Nuclear Instruments and Methods in Physics Research, Section A: Accelerators, Spectrometers, Detectors and Associated Equipment*, 410(3):407–417, 1998.

[31] J. S. Ng, P. Chen, H. Baldis, P. Bolton, D. Cline, W. Craddock, C. Crawford, F. J. Decker, C. Field, Y. Fukui, V. Kumar, R. Iverson, F. King, R. E. Kirby, K. Nakajima, R. Noble, A. Ogata, P. Raimondi, D. Walz, and A. W. Weidemann. Observation of plasma focusing of a 28.5 GeV positron beam. *Physical review letters*, 87(24):244801, 2001.

[32] R. Assmann, P. Chen, F. J. Decker, R. Iverson, P. Raimondi, T. Raubenheimer, S. Rokni, R. Siemann, D. Walz, D. Whittum, S. Chattopadhyay, W. Leemans, T. Katsouleas, S. Lee, C. Clayton, C. Joshi, K. Marsh, W. Mori, and G. Wang. Proposal for a one GeV plasma wakefield acceleration experiment at SLAC. *Nuclear Instruments and Methods in Physics Research, Section A: Accelerators, Spectrometers, Detectors and Associated Equipment*, 410(3):396–406, 1998.

[33] M. J. Hogan, R. Assmann, F. J. Decker, R. Iverson, P. Raimondi, S. Rokni, R. H. Siemann, D. Walz, D. Whittum, B. Blue, C. E. Clayton, E. Dodd, R. Hemker, C. Joshi, K. A. Marsh, W. B. Mori, S. Wang, T. Katsouleas, S. Lee, P. Muggli, P. Catravas, S. Chattopadhyay, E. Esarey, and W. P. Leemans. E-157: A 1.4-m-long plasma wake field acceleration experiment using a 30 GeV electron beam from the Stanford Linear Accelerator Center Linac. *Physics of Plasmas*, 7(5):2241, 2000.

[34] C. Joshi, B. Blue, C. E. Clayton, E. Dodd, C. Huang, K. A. Marsh, W. B. Mori, S. Wang, M. J. Hogan, C. O'Connell, R. Siemann, D. Watz, P. Muggli, T. Katsouleas, and S. Lee. High energy density plasma science with an ultrarelativistic electron beam. *Physics of Plasmas*, 9(5):1845, 2002.

[35] M. J Hogan, C. D Barnes, C. E Clayton, F. J Decker, S. Deng, P. Emma, C. Huang, R. H Iverson, D. K Johnson, C. Joshi, T. Katsouleas, P. Krejcik, W. Lu, K. A Marsh, W. B Mori, P. Muggli, C. O'Connell, E. Oz, R. H Siemann, D. Walz, and C L O Connell. Multi-GeV Energy Gain in a Plasma-Wakefield Accelerator. *Physical Review Letters*, 95(5):054802, 2005.

[36] I. Blumenfeld, C. E. Clayton, F.-J. Decker, M. J. Hogan, C. Huang, R. Ischebeck, R. Iverson, C. Joshi, T. Katsouleas, N. Kirby, W. Lu, K. A. Marsh, W. B. Mori, P. Muggli, E. Oz, R. H. Siemann, D. Walz, and M. Zhou. Energy doubling of 42 GeV electrons in a metre-scale plasma wakefield accelerator. *Nature*, 445(7129):741–4, 2007.

[37] C. Clayton, B. Blue, E. Dodd, C. Joshi, K. Marsh, W. Mori, S. Wang, P. Catravas, S. Chattopadhyay, E. Esarey, W. Leemans, R. Assmann, F. Decker, M. Hogan, R. Iverson, P. Raimondi, R. Siemann, D. Walz, T. Katsouleas, S. Lee, and P. Muggli. Transverse Envelope Dynamics of a 28.5-GeV Electron Beam in a Long Plasma. *Physical Review Letters*, 88(15), 2002.

[38] S. Wang, C. E. Clayton, B. E. Blue, E. S. Dodd, K. A. Marsh, W. B. Mori, C. Joshi, S. Lee, P. Muggli, T. Katsouleas, F. J. Decker, M. J. Hogan, R. H. Iverson, P. Raimondi, D. Walz, R. Siemann, and R. Assmann. X-Ray Emission from Betatron Motion in a Plasma Wiggler. *Physical Review Letters*, 88(13):135004, 2002.

[39] D. Johnson, D. Auerbach, I. Blumenfeld, C. Barnes, C. Clayton, F. Decker, S. Deng, P. Emma, M. Hogan, C. Huang, R. Ischebeck, R. Iverson, C. Joshi, T. Katsouleas, N. Kirby, P. Krejcik, W. Lu, K. Marsh, W. Mori, P. Muggli, C. O'Connell, E. Oz, R. Siemann, D. Walz, and M. Zhou. Positron Production by X Rays Emitted by Betatron Motion in a Plasma Wiggler. *Physical Review Letters*, 97(17):1–4, 2006.

[40] S. Deng, C. Barnes, C. Clayton, C. O'Connell, F. Decker, R. Fonseca, C. Huang, M. Hogan, R. Iverson, D. Johnson, C. Joshi, T. Katsouleas, P. Krejcik, W. Lu, W. Mori, P. Muggli, E. Oz, F. Tsung, D. Walz, and M. Zhou. Hose Instability and Wake Generation by an Intense Electron Beam in a Self-Ionized Gas. *Physical Review Letters*, 96(4), 2006.

[41] E. Oz, S. Deng, T. Katsouleas, P. Muggli, C. D. Barnes, I. Blumenfeld, F. J. Decker, P. Emma, M. J. Hogan, R. Ischebeck, R. H. Iverson, N. Kirby, P. Krejcik, C. O. Connell, R. H. Siemann, D. Walz, D. Auerbach, C. E. Clayton, C. Huang, D. K. Johnson, C. Joshi, W. Lu, K. A. Marsh, W. B. Mori, and M. Zhou. Ionization-Induced Electron Trapping in Ultrarelativistic Plasma Wakes. *Physical Review Letters*, 98:084801, 2007.

[42] N. Kirby, I. Blumenfeld, C. E. Clayton, F. J. Decker, M. J. Hogan, C. Huang, R. Ischebeck, R. H. Iverson, C. Joshi, T. Katsouleas, W. Lu, K. A. Marsh, S. F. Martins, W. B. Mori, P. Muggli, E. Oz, R. H. Siemann, D. Walz, and M. Zhou. Transverse emittance and current of multi-GeV trapped electrons in a plasma wakefield accelerator. *Physical Review Special Topics- Accelerators and Beams*, 12:051302, 2009.

[43] M. Litos, E. Adli, W. An, C. I. Clarke, C. E. Clayton, S. Corde, J. P. Delahaye, R. J. England, a. S. Fisher, J. Frederico, S. Gessner, S. Z. Green, M. J. Hogan, C. Joshi, W. Lu, K. a. Marsh, W. B. Mori, P. Muggli, N. Vafaei-Najafabadi, D. Walz, G. White, Z. Wu, V. Yakimenko, and G. Yocky. High-efficiency acceleration of an electron beam in a plasma wakefield accelerator. *Nature*, 515(7525):92–95, 2014.

[44] C. E. Clayton, E. Adli, J. Allen, W. An, C. I. Clarke, S. Corde, J. Frederico, S. Gessner, S. Z. Green, M. J. Hogan, C. Joshi, M. Litos, W. Lu, K. A. Marsh, W. B. Mori, N. Vafaei-Najafabadi, X. Xu, and V. Yakimenko. Self-mapping the longitudinal field structure of a nonlinear plasma accelerator cavity. *Nature Communications*, 7:12483, 2016.

[45] S. Corde, E. Adli, J. M. Allen, W. An, C. I. Clarke, B. Clausse, C. E. Clayton, J. P. Delahaye, J. Frederico, S. Gessner, S. Z. Green, M. J. Hogan, C. Joshi, M. Litos, W. Lu, K. A. Marsh, W. B. Mori, N. Vafaei-Najafabadi, D. Walz, and V. Yakimenko. High-field plasma acceleration in a high-ionization-potential gas. *Nature Communications*, 7:11898, 2016.

[46] I. Blumenfeld. *Scaling of the longitudinal electric fields and transformer ratio in a non-linear Plasma Wakefield Accelerator*. PhD thesis, Stanford University, 2009.

[47] M. M. Zhou. *Accelerating Ultra-Short Electron/ Positron Bunches in Field Ionization Produced Plasmas*. PhD thesis, University of California, Los Angeles, 2008.

[48] A. Pak, K. A. Marsh, S. F. Martins, W. Lu, W. B. Mori, and C. Joshi. Injection and Trapping of Tunnel-Ionized Electrons into Laser-Produced Wakes. *Physical Review Letters*, 104:025003, 2010.

[49] I. Blumenfeld, C. Clayton, F. Decker, M. Hogan, C. Huang, R. Ischebeck, R. Iverson, C. Joshi, T. Katsouleas, N. Kirby, W. Lu, K. Marsh, W. Mori, P. Muggli, E. Oz, R. Siemann, D. Walz, and M. Zhou. Scaling of the longitudinal electric field and transformer ratio in a nonlinear plasma wakefield accelerator. *Physical Review Special Topics - Accelerators and Beams*, 13(11):111301, 2010.

[50] R. Gholizadeh, T. Katsouleas, P. Muggli, C. Huang, and W. Mori. Preservation of Beam Emittance in the Presence of Ion Motion in Future High-Energy Plasma-Wakefield-Based Colliders. *Physical Review Letters*, 104(15):155001, 2010.

[51] J. Rosenzweig, A. Cook, A. Scott, M. Thompson, and R. Yoder. Effects of Ion Motion in Intense Beam-Driven Plasma Wakefield Accelerators. *Physical Review Letters*, 95(19):195002, 2005.

[52] B. W. Montague and W. Schnell. Multiple scattering and synchrotron radiation in the plasma beat-wave accelerator. In *AIP Conference Proceedings*, volume 130, pages 146–155. AIP, 1985.

[53] K. L. F. Bane, P. Chen, and P. B. Wilson. On Collinear Wake Field Acceleration. *IEEE Transactions on Nuclear Science*, 32(5):3524–3526, 1985.

[54] R. D. Ruth, A. W. Chao, P. L. Morton, and P. B. Wilson. A Plasma Wake Field Accelerator. *Particle Accelerators*, 17:171–189, 1985.

[55] B. Jiang, C. Jing, P. Schoessow, J. Power, and W. Gai. Formation of a novel shaped bunch to enhance transformer ratio in collinear wakefield accelerators. *Physical Review Special Topics - Accelerators and Beams*, 15(1):1–8, 2012.

[56] W. An, W. Lu, C. Joshi, W. B. Mori, C. Huang, M. J. Hogan, S. F. Martins, L. O. Silva, S. H. Gold, and G. S. Nusinovich. Simulations of Two-Bunch Plasma Wakefield Accelerator Experiments at FACET. In *Proceedings of the Advanced Accelerator Concepts: 14th Advanced Accelerator Concepts Workshop*, pages 472–477, 2010.

[57] M. J. Hogan, T. O. Raubenheimer, A. Seryi, P. Muggli, T. Katsouleas, C. Huang, W. Lu, W. An, K. A. Marsh, W. B. Mori, C. E. Clayton, and C. Joshi. Plasma wakefield acceleration experiments at FACET. *New Journal of Physics*, 12(5):055030, 2010.

[58] P. Muggli, K.A. Marsh, S. Wang, C.E. Clayton, S. Lee, T.C. Katsouleas, and C. Joshi. Photo-ionized lithium source for plasma accelerator applications. *IEEE Transactions on Plasma Science*, 27(3):791–799, 1999.

[59] K. A. Olive et al. Review of particle physics. *Chinese Physics*, C38:090001, 2014.

[60] K. A. Marsh, W. An, C. E. Clayton, C. Joshi, W. B. Mori, N Vafaei-Najafabadi, P. Muggli, C. I. Clarke, S. Corde, J.-P. Delahaye, R. J. England, A. S. Fisher, J. Frederico, S. J. Gessner, M. J. Hogan, S. Z. Li, M. D. Litos, D. Walz, Z. Wu, E. Adli, and W. Lu. X-ray radiation and electron injection from beam envelope oscillations in plasma wakefield accelerator experiments at FACET. In *Proceedings of the PAC2013*, pages 1105–1107, 2013.

[61] J. B. Rosenzweig and P. Chen. Beam optics of a self-focusing plasma lens. *Physical Review D*, 39(7):2039–2045, 1989.

[62] A. S. Muller. Description of Beam-Matter Interaction in the Covariance Matrix Formalism: Application to Modification of Emittance and Twiss Parameters; rev. version. Technical Report CERN-PS-2001-013-AE, CERN, Geneva, May 2001.

[63] S. Z. Li, E. Adli, R. J. England, J. Frederico, S. J. Gessner, M. J. Hogan, M. D. Litos, D. R. Walz, P. Muggli, W. An, C. E. Clayton, C. Joshi, W. Lu, K. a. Marsh, W. Mori, and N. Vafaei. Head erosion with emittance growth in PWFA. In *Proceedings of the Advanced Accelerator Concepts: 15th Advanced Accelerator Concepts Workshop*, pages 582–587, 2013.

[64] Z. Wu, A. S. Fisher, J. Goodfellow, M. Fuchs, D. Daranciang, M. Hogan, H. Loos, and A. Lindenberg. Intense terahertz pulses from SLAC electron beams using coherent transition radiation. *The Review of scientific instruments*, 84(2):022701, 2013.

[65] R. Fulton, J. Haggerty, R. Jared, R. Jones, J. Kadyk, C. Field, W. Kozanecki, and W. Koska. A high resolution wire scanner for micron-size profile measurements at the SLC. *Nuclear Instruments and Methods in Physics Research Section A: Accelerators, Spectrometers, Detectors and Associated Equipment*, 274(1-2):37–44, 1989.

[66] D. L. Bruhwiler, D. A. Dimitrov, J. R. Cary, E. Esarey, W. Leemans, and R. E. Giacone. Particle-in-cell simulations of tunneling ionization effects in plasma-based accelerators. *Physics of Plasmas*, 10(5):2022, 2003.

[67] K.A. Marsh, C.E. Clayton, D.K. Johnson, C Huang, C Joshi, W Lu, W.B. Mori, M Zhou, C.D. Barnes, F.-J. Decker, M.J. Hogan, R Iverson, P Krejcik, C.L. O'Connell, R Siemann, D Walz, S. Deng, T.C. Katsouleas, P Muggli, and E. Oz. Beam Matching to a Plasma Wake Field Accelerator using a Ramped Density Profile at the Plasma Boundary. In *Proceedings of the 2005 Particle Accelerator Conference*, pages 2702–2704. IEEE, 2005.

[68] I. Kostyukov, S. Kiselev, and A. Pukhov. X-ray generation in an ion channel. *Physics of Plasmas*, 10(12):4818–4828, 2003.

[69] N. Vafaei-Najafabadi, K. A. Marsh, C. E. Clayton, W An, W. B. Mori, C Joshi, W Lu, E Adli, S Corde, M Litos, S Li, S Gessner, J Frederico, A. S. Fisher, Z Wu, D Walz, R. J. England, J. P. Delahaye, C. I. Clarke, M. J. Hogan, and P Muggli. Beam loading by distributed injection of electrons in a plasma wakefield accelerator. *Physical Review Letters*, 112(2):025001, 2014.

[70] A. Martinez de la Ossa, J. Grebenyuk, T. Mehrling, L. Schaper, and J. Osterhoff. High-Quality Electron Beams from Beam-Driven Plasma Accelerators by Wakefield-Induced Ionization Injection. *Physical Review Letters*, 111(24):245003, 2013.

[71] C. Mcguffey, A. G. R. Thomas, W. Schumaker, T. Matsuoka, V. Chvykov, F. J. Dollar, G. Kalintchenko, V. Yanovsky, A. Maksimchuk, K. Krushelnick, V. Y. Bychenkov, I. V. Glazyrin, and A. V. Karapeev. Ionization Induced Trapping in a Laser Wakefield Accelerator. *Physical Review Letters*, 104:025004, 2010.

[72] E. Adli, S.J. Gessner, S. Corde, M.J. Hogan, and H.H. Bjerke. Cherenkov light-based beam profiling for ultrarelativistic electron beams. *Nuclear Instruments and Methods in Physics Research Section A: Accelerators, Spectrometers, Detectors and Associated Equipment*, 783:35–42, 2015.

[73] R. M. Herman and T. A. Wiggins. Production and uses of diffractionless beams. *Journal of the Optical Society of America A*, 8(6):932, 1991.

[74] R. Weingartner, S. Raith, a. Popp, S. Chou, J. Wenz, K. Khrennikov, M. Heigoldt, a. R. Maier, N. Kajumba, M. Fuchs, B. Zeitler, F. Krausz, S. Karsch, and F. Grüner. Ultralow emittance electron beams from a laser-wakefield accelerator. *Physical Review Special Topics - Accelerators and Beams*, 15(11):111302, 2012.

[75] C. C. Silverstein. *Design and technology of heat pipes for cooling and heat exchange*. Taylor and Francis, 1992.

[76] A. G. Mozgovoi, I. I. Novikov, M. A. Pokrasin, and V. V. Roschupkin. The saturated vapour pressure of lithium, sodium, potassium, rubidium, and cesium. *High Temperatures. High Pressures*, 19(4):425–430, 1987.

[77] W. A. Barletta. Lecture 4, beam properties, fundamentals of accelerator physics and technology with simulations and measurements lab. U.S. Particle Accelerator School, 2009.